Thesis for the Degree of
Licentiate of Philosophy

Computational studies of Chemical Looping combustion materials and CO_2 activating surfaces

Teemu Parviainen

University of Jyväskylä
Department of Physics, Nanoscience Center
Supervisors: Karoliina Honkala & Hannu Häkkinen
June 2016

Preface

This work was done at the Nanoscience Center (NSC) of the Univesity of Jyväskylä between May 2013 and January 2016.

First of all, I would like to thank my supervisors, Dr. Karoliina Honkala and professor Hannu Häkkinen, for providing me interesting topics for my graduate studies and great guidance to carry out them. Furthermore, thanks goes to the whole NSC personnel for creating very inspiring atmosphere for working and especially to Dr. Vesa Apaja who has always when needed provided very valuable support in computer related problems. I am also thankful for professor H. J. Freund alongside with his research group from the Department of Chemical Physics in Fritz-Haber-Institut der Max-Planck-Gesellschaft in Berlin, Germany, for collaboration and carrying out interesting thin film experiments.

Financial support from Jenny and Antti Wihuri foundation as well as the University of Jyväskylä Graduate School for Doctoral Students is gratefully acknowledged. I am also grateful for The National Doctoral Programme in Nanoscience (NGS-NANO) for funding my trips to summer school Copenhagen in 2014 as well as to the International Conference on Chemical Looping in Gothenburg 2014. These trips greatly enhanced my expertise and provided me valuable connections. I also acknowledge the Finnish IT Center for Science (CSC) and the NSC for the essential computer resources.

Finally, I want to thank my wonderful girlfriend Katariina, my all family and friends for supporting me during the ups and downs in carrying out this work.

Jyväskylä, June 2016
Teemu Parviainen

Abstract

Unarguably the world energy production is still dependent on the usage of fossil fuels which are the main source of greenhouse gases (GHG) such as CO_2. One of the most viable techniques to reduce CO_2 emissions is Carbon Capture and Storage (CCS). Among this category of techniques Chemical Looping Combustion (CLC) which is based on alternating oxidizing and reduction steps of Oxygen Carrier (OC) providing pure oxygen for the fuel burning. Another strategy to be used either in combination with CLC or as a standalone solution would be to transform CO_2 into higher value products *via* e.g. heterogeneous catalysis, which was the topic of the second part in this thesis.

In the first part of this work two OCs, Cu and Mn oxides CuO and Mn_2O_3, were selected for evaluation using DFT calculations in respect of oxygen uncoupling. Oxygen vacancy formation energies and diffusion barriers both in bulk and at the vicinity of the surface were calculated and tendency of reduction under different conditions was studied using atomistic thermodynamics. It is found that the lowest vacancy formation energy at the surface is always lower than in the corresponding bulk which favors particles having high surface to bulk ratio in terms of reduction. On the other hand, diffusion is not expected to be the rate determining step. Atomistic thermodynamics approach reveals that Mn_2O_3 is readily reduced into Mn_3O_4 at relatively low temperatures whereas the reduction of CuO is not straightforward and is likely dependent on additional adsorbed reducing agents, such as fuel molecules. Additionally the effect of applying lateral structural straining to the oxygen diffusion barriers were studied. It was found that in general straining the lattice decreases the diffusion barrier inside bulk materials. It can be concluded that these calculations provide a framework to study the redox reactivity of OC materials under CLC conditions using *ab initio* DFT calculations.

In the latter part of this thesis catalytic activity of Au/MgO/Ag thin film in CO_2 activation process was studied computationally. It was found that the adsorption of CO_2 is enhanced at the edges of Au clusters when compared to the clean MgO/Ag system. However, the adsorption energy varies among different

Au cluster models which can be explained both by the relative Lewis acidity and different D-band center locations of the Au islands. When CO_2 is adsorbed either on clean MgO or at the edge of Au island, the linear conformation of the molecule is broken and it adapts an activated bent shape. However, on clean MgO the formation of oxalate species, i.e. forming a C-C bond between two CO_2 molecules, is sterically much more restricted compared to the adsorption configuration at the edge of Au cluster. This is potentially the most significant factor, alongside with the electron shuttling properties, in the observed catalytic effect of Au/MgO/Ag thin film systems for CO_2 reactions.

The results for the CLC-materials are intended to be published and the author has written the original draft with the title "Mn and Cu oxides from first principles calculations: Reduction of CLC materials". Part of the results related to the latter part, thin film CO_2 activation, have been published in [1] for which the author has performed all the DFT calculations.

Contents

Preface **i**

Abstract **ii**

1 Introduction **1**

1.1 Chemical Looping Combustion (CLC) and Chemical Looping with Oxygen Uncoupling (CLOU) 1

1.1.1 Motivation and Principles 1

1.1.2 Mn and Cu Oxides as CLC materials 4

1.1.3 Strain in metal oxides 5

1.2 CO_2 usage in industrial scale and value-adding processes 6

1.2.1 Motivation and challenges 6

1.2.2 Gold in nano-scale 8

1.3 About this thesis 9

2 Theoretical Background and Computational Methods **11**

2.1 The Schrödinger Equation 11

2.2 Density Functional Theory 12

2.2.1 The Hohenberg-Kohn theorems 12

2.2.2 Kohn-Sham approach 14

2.2.3 Exchange-Correlation Functionals 15

2.3 Numerical implementation of the DFT theory 18

2.3.1 Periodic systems 19

2.3.2 Plane-Waves 19

2.3.3 Real Space Grids 20

2.3.4 Separation of core and valence states 20

2.4 Atomistic Thermodynamics 23

2.5 Bader charge analysis 24

2.6 Local Density of States 25

2.7 Apparent activation energy 25

2.8 Computational details 28

2.8.1 CLC materials 28
2.8.2 Au/MgO/Ag surfaces 32

3 Results and Discussion **36**
3.1 Mn and Cu Oxides for CLC 36
3.1.1 Lattice Parameters, Electronic Structures and Formation Enthalpies 36
3.1.2 Formation of oxygen vacancies and their migration in bulk 39
3.1.3 Thermodynamics and kinetics at the surface 48
3.1.4 The effect of straining to the kinetics in bulk 63
3.2 CO_2 on Au/MgO(100)/Ag and C_2O_4 formation 68
3.2.1 CO_2 Adsorption Energies 69
3.2.2 DOS comparison between Au_x and Au_x-CO_2 systems. . . 74
3.2.3 Adsorption at the vicinity of Au 77
3.2.4 Formation of C_2O_4 78
3.2.5 Vibration Analysis 82

4 Summary and Outlook **85**

1 Introduction

1.1 Chemical Looping Combustion (CLC) and Chemical Looping with Oxygen Uncoupling (CLOU)

1.1.1 Motivation and Principles

Despite increasing investments made to renewable energy source power plants, the global energy production is still heavily dependent on non-renewable fossil fuels, such as coal and oil. As is widely accepted, the usage of fossil fuels has major damaging environmental effects due to the emission of greenhouse gases (GHG), e.g. CO_2, SO_x, NO_x and CH_4 of which CO_2 has the main contribution [2]. These greenhouse gases are able to absorb thermal energy coming from the Sun therefore having a great potential to disturb the energy budget of the Earth. Indeed, the increasing greenhouse gas content of the atmosphere due to human activity over the past decades seems to have had the most significant contribution to the global warming which is imposing an alarming threat to the biodiversity of the Earth [3]. The usage of fossil fuels and greenhouse gas emissions are expected only to increase during the following years without additional significant efforts to reduce the dependency of the energy production on fossil fuels due to global economic and population growth [4].

Globally power generation and transport are the dominating GHG emission sources both accounting for 30-35 % of total emissions [5]. In these sectors some crucial efforts have been made to decrease the net CO_2 emissions to the atmosphere. These actions include among other things reducing energy consumption, increasing the efficiency of energy conversion and utilization, switching to less carbon intensive fuels, increasing the use of renewable sources of energy and enhancing the biological CO_2 sinks by increasing the capacity of forest and plants. However, even adding efforts of all of these methods will probably turn out to be insufficient to reach the sustainable low CO_2 levels if new techniques and policies are not adapted in large scale [6].

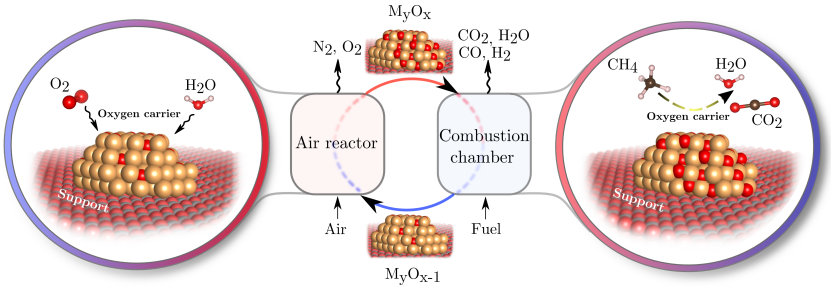

Figure 1.1. *The principle of chemical looping combustion. Oxygen carrier particles are oxidized in the air reactor and are transported into fuel chamber. Here, the excess oxygen in OC particles is released for the burning reaction of the fuel. As a result only CO_2 and O_2 are produced which can be separated easily.*

According to IPCC, over 80 % of world energy consumption will be satisfied by fossil fuels during the first part of the 21$^{\mathbf{st}}$ century [7]. Therefore, strategy to develop existing fossil fuel power plants seems to be a necessary strategy to tackle the problem of global warming. One of the most important technologies in this area would be methods for CO_2 capture and storage (CCS) which enables combustion of fossil fuels without net GHG emissions, or even negative net emissions if biomass is used as fuel. Different CCS approaches have been developed many of them having a high energy penalty, unfortunately. However, among all CCS technologies Chemical Looping Combustion (CLC) has been identified one of the most promising alternatives to reduce the cost of CO_2 capture [8].

In general, CLC reaction consists of two phases, presented in Figure 1.1 where a special oxygen carrier (OC), which is usually a metal oxide MeO on a support material, circulates between two chambers (air reactor AR and fuel reactor FR) oxidizing and reducing in an alternating manner. Pure oxygen is provided for the burning reaction of the fuel. Fuel is isolated into its own chamber and the re-oxidation of the OC happens in an air reactor. Thus, fuel and air are separated and the products of the combustion consists only of streams of pure CO_2 and H_2O steam which can be easily separated without any additional energy cost by condensing steam. The gaseous CO_2 produced in the combustion chamber can be captured and stored without requiring energy intensive equipment for the separation process.

In conventional CLC fuel molecules react directly with OC particles in the oxidation process. An alternative technique has been introduced quite recently by Mattisson *et. al.* [9] appointed as chemical-looping combustion with oxy-

gen uncoupling (CLOU). In contrary to CLC, in CLOU oxygen carrier which releases gaseous O_2 is used. Otherwise the reactor design is much similar to conventional CLC.

The performance of CCS in CLC power plant is strongly dependent on the properties of the OC particles. Hundreds of different materials have been tested but the choice of appropriate oxygen carrier remains a challenge due to requirements for stability and redox reactivity under harsh CLC conditions. The active oxide is typically supported by inert oxide, such as Al_2O_3, ZrO_2 or SiO_2 to increase the mechanical strength of the particles and the surface area of active material. In CLOU OCs have the additional requirement to release gaseous oxygen at suitable temperatures and O_2 partial pressures. One of the measures used to characterize and evaluate OC materials is oxygen transport capacity R_O, which is defined as the ratio of released oxygen $m_{\mathrm{ox}} - m_{\mathrm{red}}$ compared to the mass of OC material at the oxidized form m_{ox}:

$$R_O = \frac{m_{\mathrm{ox}} - m_{\mathrm{red}}}{m_{\mathrm{ox}}}. \tag{1.1}$$

In addition, reactivity is discussed in the literature usually referring to the conversion rate of OC particles during oxidation or reduction or the oxidation rate of the fuel flow $d[c(t)]/dt$, where $c(t)$ is the time-dependent concentration of gas. The oxygen carrying capacity alongside the exhibited reactivity determines the circulation speed of OC material and fuel stream inside CLC reactor. Higher OC circulation rate tends to lead more rapid attrition of the particles lowering the overall performance.

One of the most studied OC materials is iron due to its low cost, low toxicity and abundant availability [10, 11]. The low reactivity, however, with typical fuels and poor oxygen transfer capacity are major drawbacks of iron-based OCs especially for CLOU process [12]. In general transition metal oxides such as Mn_3O_4[13], CuO[14, 15] and NiO[16, 17] offer both better reactivity and oxygen transfer capacity profiles compared to iron oxides. Until now, at least Mn_2O_3/Mn_3O_4, CuO/Cu_2O and Co_3O_4/CoO oxide pairs have been identified to have suitable thermodynamic properties for CLOU[9]. These systems are able to release gaseous oxygen through the following reversible reactions:

$$\begin{aligned} 4\mathrm{CuO} &\leftrightarrow 2\mathrm{Cu_2O} + \mathrm{O_2(g)}, \quad \Delta H_{850} = 263.2\mathrm{kJ/molO_2} \\ 6\mathrm{Mn_2O_3} &\leftrightarrow 4\mathrm{Mn_3O_4} + \mathrm{O_2(g)}, \quad \Delta H_{850} = 193.9\mathrm{kJ/molO_2} \\ 2\mathrm{Co_3O_4} &\leftrightarrow 6\mathrm{CoO} + \mathrm{O_2(g)}, \quad \Delta H_{850} = 408.2\mathrm{kJ/molO_2} \end{aligned} \tag{1.2}$$

The study presented here aims to characterize the first two of these reactions

using quantum mechanic calculations approach and thus to collect atomistic information related to the reduction process.

1.1.2 Mn and Cu Oxides as CLC materials

All things considered, manganese and copper oxides are attractive materials for the basis of OC particles according to literature review [18]. In general, oxides of transition metals, like manganese and copper, are very complex materials with many different phases in morphology and magnetic structures. The ranging properties have attracted well-earned attention for transition metal oxides and many studies highlighting interesting applications, e.g. high T_c superconductors [19], photocatalysis [20] and solid oxide fuel cells [21] have emerged. The presence of many possible different oxidation states is an important characteristic for oxygen transport applications, such as OC in CLC [22].

For both manganese and copper based oxides two different bulk structures were selected, i.e. the reduced and oxidized form. According to the literature review, most relevant two phases of manganese oxides for CLC are Mn_3O_4 and Mn_2O_3. Correspondingly for copper oxides Cu_2O and CuO were selected. Above, the reduced form is mentioned first.

Like iron oxides, manganese oxide has many oxidation states and is an environmentally friendly and low cost material which is also readily available. However, despite these favorable characteristics, only few studies have been investigating Mn-based oxygen carriers so far. Those studies have revealed intermediate reactivity characteristics, although more favorable than those of iron, but also tendency to form stable secondary spinel structures with some support materials which limits the oxygen carrying capacity of the OCs [23, 24, 25]. However, by combining active manganese oxide with suitable metals, like Fe or Ni, the fuel conversion rates, oxygen release capacity and long-term stability may be enhanced greatly [26].

Copper oxide CuO, unlike manganese oxide, has attracted a lot of interest due to the high reactivity yet being a relatively low cost and environmentally friendly material among the possible CLC materials [27]. Pure CuO is known to exhibit high reactivity even at low temperatures with various fuels [14, 28] although according to de Diego *et. al.* [29] the mechanical properties are poor leading to unacceptable rate of particle degradation and reduced reactivity with increasing number of oxidation-reduction cycles. On the other hand, oxygen carriers prepared by mechanical mixing with several support materials and CuO as an active phase show significantly higher reactivity both in reduction

and oxidation phase with superior mechanical strength compared to pure CuO particles.

1.1.3 Strain in metal oxides

In most crystalline materials the arrangement of atoms rarely represents the ideal crystal structure. In addition to point defects, like already discussed oxygen vacancies, straining is often introduced to the structure by e.g. the interfaces between nanoparticles and the support material or between dissimilar oxides. Several experimental studies have reported that this kind of straining plays an important role in surprisingly high ionic conductivity of materials compared to the clean structures. Also, oxygen defect formation enthalpy, adsorption enthalpies, dissociation energies and charge transfer barriers undergo stress induced changes [30].

Especially yttria-stabilized zirconia (YSZ, 85 % ZrO_2, 15 % Y_2O_3) has been studied excessively when considering the influence of straining to the migration barrier energy due to its usability in solid oxide fuel cells in which the ionic conduction plays a crucial role. In general, it has been found that the migration barrier lowers with the increasing tensile straining of the YSZ structure [31, 32, 33] and increases when compression is applied [34]. This has been explained by increased free space along the migration path and weakened bonds between the migrating oxygen and the cations upon applying tensile strain. On the other hand, counter-intuitively also strong compressive strain applied to the structure can decrease oxygen migration barrier. Hirschfeld *et al.* [34] studied ZrO_2 employing DFT and found out that the maximum migration barrier occurs under 0.91 strain beyond which it descends until vanishing completely. Here the explanation is that while the initial position becomes more and more unfavorable, the energy at the barrier position does not increase at the same rate at large enough compression when straining is beyond elastic region. Therefore the mechanisms for ionic migration are still rather poorly understood and no generally valid models for the reaction energies in metal oxides can be formulated. Therefore it is crucial to study each material and diffusion path individually.

Since straining in bulk metal oxides is expected to have significant effect for the diffusion processes, in this work the oxygen migration energies were calculated also for strained oxides. The straining was applied in x, y and z directions equally up to 6 %.

1.2 CO_2 usage in industrial scale and value-adding processes

1.2.1 Motivation and challenges

CO_2 captured by any CCS method, like CLC, has to be either stored or used. The storage is considered the riskiest, and therefore most controversial, solution to tackle down the CO_2 concentration in the atmosphere because the gas has to be injected into underground natural sites for economical reasons. Also storage in oceans has been suggested but this is not generally considered feasible due to ocean acidification leading to possibly hazardous environmental impacts. The CO_2 is therefore usually stored in form of stable carbonates into the soil. Many unpredictable factors are related to this kind of solution, like geological activity in long time scales and risk of leakage during the transport and long term storage. It has to be noted, that this approach can only be effective if the captured gas is stored for long time scales, i.e. several hundreds of thousands years. However, by carefully selecting and later monitoring the site of injection these risks are low [4]. Also, such leakage would rarely pose any life threatening danger since humans are able to tolerate CO_2 up to 30,000 ppm concentrations without any adverse consequences [35]. Though, impacts of elevated CO_2 levels on the ecosystem are less well understood since the concept of CO_2 storage is relatively new introduced commercially first in 2000 [36].

The existing industrial uses of CO_2 are mostly consisting of CO_2-enhanced oil recovery (EOR), beverage carbonation, food processing, preservation and packaging. EOR is by far the most abundant use of CO_2 with $\sim$70 % share of the global demand of $\sim$ 80 million tonnes a year [37]. In EOR CO_2 gas is injected into nearly depleted oil fields releasing the trapped oil from the soil formations increasing the recoverable oil resources and therefore boosting the efficiency of oil plants by up to 15% [5]. The injected CO_2 is stored in the ground or recycled back into the injection well. Therefore, the procedure resembles closely to the CO_2 storage having essentially the same environmental impacts with the benefit of carbon dioxide concentration reduction from the atmosphere. This is necessarily not common to the other utilization methods since often CO_2 gas is only used as an inert and is released back into the atmosphere at the end of the process or product lifetime [37]. On the other hand, EOR increases the usage of fossil fuels by increasing the supply into the markets so the overall environmental effect is less flattering.

Comparing the present global usage of pure CO_2 of $<$ 100 million tonnes

per year to corresponding emissions from fossil fuel combustion and industrial processes summing up to $\sim$ 35 billion tonnes [38], it is evident that there is a huge demand for new methods to utilize CO_2. Especially *carbon recycling* techniques, i.e. utilization of carbon dioxide in the synthesis of organic chemicals are getting much interest. The idea is to use CO_2 as a C_1 building block for making e.g. organic chemicals, materials and other carbohydrates, thus cutting the GHG emissions by reducing nonrenewable petroleum usage and producing useful compounds [39]. However, the usage of CO_2 as a chemical feedstock is still very limited primarily due to thermodynamic stability of the molecule structure so new designs and improvements for existing catalytic systems have to be studied [40].

CO_2 hydrogenation *via* reverse gas shift (RWGS) reaction and following hydrogenation of CO

$$CO_2 + H_2 \longleftrightarrow CO + H_2O, \Delta H_{573\ K} = 38\ \text{kJmol}^{-1} \tag{1.3}$$

$$CO + 2\,H_2 \longrightarrow (CH_2) + H_2O, \Delta H_{573\ K} = -166\ \text{kJmol}^{-1} \tag{1.4}$$

has been studied and identified as one promising mechanism for CO_2 conversion [41]. Since the RWGS reaction is endothermic, high temperatures are needed which sets limits to the catalysts. E.g. some copper-based catalysts have performed well in terms of activity and selectivity but the thermal stability is typically rather poor due to sintering of copper. Methanation of CO_2, i.e. catalytic hydrogenation to methane (also called Sabatier reaction) is also an important carbon dioxide value-adding process. The reaction is thermodynamically favorable with $\Delta H_{298\ K} = -252.9\ \text{kJmol}^{-1}$, though catalyst is required due to the kinetic restrictions of linear structure of CO_2, but according to the equation

$$CO_2 + 4\,H_2 \longrightarrow CH_4 + 2\,H_2O \tag{1.5}$$

process uses hydrogen much more than hydrogenation *via* RWGS reaction. H_2 generation remains challenging process and currently fossil fuels are the dominant source of industrial hydrogen [42]. This is problematic, since the used steam reforming technique yields also CO_2 as a by-product negating the atmospheric CO_2 concentration reduction of hydrogenation process. Water splitting by e.g. electrolysis, photocatalysis or radiolysis would be an interesting alternative source of hydrogen but much research is still needed to achieve reasonable economic efficiency [43].

Another potential route to activate CO_2 molecules to achieve higher value products is *via* initial electron transfer yielding a corresponding $CO_2{}^{-\bullet}$ anion

radical as an intermediate. In the gas phase for a single carbon dioxide molecule the electron affinity is negative, thus the electron transfer reaction

$$CO_2{}^{-\bullet} \longrightarrow CO_2 + e^- \tag{1.6}$$

is exothermic by about 40-60 kJ/mol [44]. However, these radical anions as well as $(CO_2)_n^{-\bullet}$ clusters have been produced *via* heterogenic reactions in the gas phase and well characterized in several experiments [45, 44, 46, 47]. When carbon dioxide accepts an electron, the structure deforms from linear to bend activating the molecule and allowing e.g. C-C bond forming. In fact, dimerization of oxalate

$$CO_2{}^{-\bullet} + CO_2{}^{-\bullet} \longrightarrow C_2O_4{}^{2-} \tag{1.7}$$

seems to be the main reaction of $CO_2{}^{-\bullet}$ when other substrates are not available [46].

In the nature the CO_2 activation occurs in ribulose 1,5-biphosphate carboxylase/oxygenase (Rubisco) enzymes through photosynthesis reaction. Carbon dioxide, Ribulose 1,5 bisphosphate (RuBP) and water molecules are aligned in specific locations around Rubisco's active center which is essentially a Mg(II) ion. The protein induces a conformational change in CO_2 molecule allowing it to react with RuBP [48]. It is therefore clear that the kinetic barriers related to the carbon dioxide activation can be overcome also by the means of rationally designed heterogeneous catalysis. It is known, that some solid-state catalysts, such as alkaline earth metals and alkaline earth metal oxides, are able to adsorb CO_2 and facilitate electron transfer to them [49, 50, 51]. However, formation of these $CO_2{}^-$ anions is not enough to activate the value adding reactions such as decomposition to CO and O or oxalate forming. Rather recent experimental study corroborated with DFT calculations has shown that inorganic electride $[Ca_{24}Al_{28}O_{64}]^{4+}(e-)_4]$ surface expresses CO_2 binding and dissociation to CO and atomic oxygen at room temperature with a reaction barrier of 1-1.5 eV [52]. Upon heating the products were also desorpted demonstrating in principle the applicability of heterogeneous catalysis in carbon dioxide activation. However, oxalate $C_2O_4{}^{2-}$ forming has not been previously demonstrated on such systems which was the main emphasis in this work.

1.2.2 Gold in nano-scale

Although gold has been known throughout the human history for its durability and beauty resulting from its inert nature, it also exhibits uniquely high

chemical activity in number of reactions. The basis for systematic research of gold catalysis was set in 1970s when Bond *et al.* studied supported gold particles as catalysts for olefins hydrogenation [53]. In the 1980s it was found that nanosized gold particles could act as a catalysis in low temperatures for CO oxidations [54] and since then a huge number of both experimental and computational studies in catalysis, photonics and biology has been made [55]. The studies have revealed that there are numerous factors affecting on the catalytic activity, like cluster size and shape, method of preparation and support material and its dimensions [56]. Especially gold clusters supported on thin film (1-5 ML) oxides on bulk metal substrate have gained much interest since it has been shown that in this kind of metal-insulator-metal systems the metallic substrate acts as an source of electrons which can be shuttled to the adsorbed reacting species giving rise to the catalytic properties [57]. Therefore, oxide/metal supported gold clusters are very attractive systems to study CO_2 activation processes.

Due to its simple structure, MgO can be considered as the most ideal ionic metal oxide. Most often MgO is grown on Mo(001) or Ag(001) metallic substrate since both share a similar cubic crystal structure, lattice constants match well and recipes for preparation are well-established [58, 59, 60]. In this thesis the model system was consisted of Au islands with different sizes and geometries supported on 2 monolayer (ML) MgO(001) thin film on Ag(001) substrate.

1.3 About this thesis

In this thesis I will focus on density functional characterization of different metal oxide materials. In Chapter 2 basic theory of DFT alongside numerical implementation and model systems used in the calculations are introduced. The discussion about the calculations is divided into two parts throughout the thesis: usage of four different metal oxides, namely Mn_3O_4, Mn_2O_3 Cu_2O and CuO, as chemical-looping combustion materials and catalytic CO_2 activation on MgO/Ag supported Au islands.

The emphasis of the first part is on the reduction capacity of the selected metal oxides. To address the problem the oxygen vacancy energies and corresponding oxygen migration barriers both in bulk and at the vicinity of the most stable surfaces are reported since these properties are closely related to the reduction process. Also, the effect of straining on diffusion barriers has been studied since the crystal structures of supported nanoparticles are rarely

ideal due to tension caused by the support material interface. The stability of oxygen defected surfaces in realistic reaction conditions is examined by the means of atomistic thermodynamics to include also pressure and temperature dependency.

In the second part of this thesis the emphasis is on CO_2 adsorption on possible sites provided by supported Au islands with different sizes and forms and oxalate C_2O_4 formation as a result of $CO_2 + CO_2$ reaction. The model systems in this part are typical slab models and the size of Au islands range from 1 to 14 atoms. In addition, semi-infinite Au stripes along (100) and (110) directions were modeled representing edges of larger Au islands which are outside the range of feasible DFT calculations. In Chapter 3 the obtained results are presented and discussed and finally in Chapter 4 conclusions and outlook will be given.

2 Theoretical Background and Computational Methods

All calculations in this work were performed by utilizing the implementations of the density functional theory (DFT) which is an *ab initio* tool to investigate the electronic structure of many-body systems. DFT has become an important tool in physics, chemistry and material sciences during the recent years due to its versatility and constantly increasing availability and more efficient utilization of computational resources, which have made the studies for increasingly complex systems possible. The purpose of this chapter is to give the reader a short introduction to the most essential steps and assumptions needed to derive equations for implementation of DFT in practice. The chapter follows for the most part the book by Parr and Yang [61].

2.1 The Schrödinger Equation

As the most material properties are directly related to the differences in total energy, we begin by introducing the Schrödinger equation (SE) which in its time independent form is given by:

$$\hat{\mathcal{H}}\Psi = E\Psi, \tag{2.1}$$

where $\hat{\mathcal{H}}$ is the Hamiltonian operator, $\Psi = \Psi(\mathbf{r}_1, \mathbf{r}_2, \dots \mathbf{r}_N; \mathbf{R}_1, \mathbf{R}_2, \mathbf{R}_M)$ is the wave function of the many-body system consisting of N electrons in positions $\vec{r}_i$ and M nuclei in positions R_I and E is the total energy of the system. The Hamiltonian consists of the sum of kinetic energies of electrons and nuclei and the interactions (Coulomb potentials) between electron-electron, nucleus-nucleus and electron-nucleus pairs, i.e. (in Hartree atomic mass units)

$$\begin{aligned}\hat{\mathcal{H}} = &-\frac{1}{2}\sum_{i=1}^{N}\nabla_i^2 - \sum_{I=1}^{M}\frac{1}{2M_I}\nabla_I^2 + \sum_{i=1}^{N}\sum_{j>i}^{N}\frac{1}{|r_i - r_j|} \\ &+ \sum_{I=1}^{M}\sum_{J>I}^{M}\frac{Z_I Z_J}{|R_I - R_J|} - \sum_{i=1}^{N}\sum_{I=1}^{M}\frac{Z_I}{|r_i - R_I|},\end{aligned} \tag{2.2}$$

where M_I is the mass of a nucleus I with proton number Z_I.

Unfortunately, analytical solutions of SE for wave-function and the associated ground state energy exists only for a narrow set of physical systems due to which approximations and additional theorems relating to the simplification of the problem have to be introduced. The first approximation made is usually the *Born-Oppenheimer approximation*. As nuclei are significantly heavier than electrons, and therefore moving at much lower speeds, it becomes conventional to separate the wave-function into the electronic (*elec*) and nucleic (*nucl*) parts:

$$\Psi_{\text{total}} = \Psi_{\text{elec}}\Psi_{\text{nucl}}. \tag{2.3}$$

The relaxation of the electrons into the ground state is considerably faster than the relaxation of the nuclei, thus the electronic system can be solved separately in the potential field of fixed nuclei. The electronic Schrödinger equation is then

$$\hat{\mathcal{H}}_{\text{elec}}\Psi = E_{\text{elec}}\Psi, \tag{2.4}$$

where electronic Hamiltonian consists of the kinetic energy of the electrons, electron-electron potential and electron-nuclei potential:

$$\begin{aligned}\hat{\mathcal{H}}_{\text{elec}} &= -\frac{1}{2}\sum_{i=1}^{N}\nabla_i^2 + \sum_{i=1}^{N}\sum_{j>i}^{N}\frac{1}{|r_i - r_j|} + \sum_{i=1}^{N}\sum_{I=1}^{M}\frac{Z_I}{|r_i - R_I|} \\ &\equiv \hat{T}_{\text{e}} + \hat{V}_{ee} + \hat{V}_{ext}\end{aligned} \tag{2.5}$$

The total energy of the system is then

$$E_{\text{tot}} = E_{\text{elec}} + \sum_{I=1}^{M}\sum_{J>I}^{M}\frac{Z_I Z_J}{|R_I - R_J|} \tag{2.6}$$

taking into account also the nuclei-nuclei interactions.

2.2 Density Functional Theory

2.2.1 The Hohenberg-Kohn theorems

Two simple theorems by Hohenberg and Kohn [62] are forming the ground of density functional theorem in which the description of the SE 2.4 with the positions of every single electron, having $3N$ degrees of freedom, is replaced by the density distribution of the electron cloud in the system. Note that to keep notations simple, the equations have been written in this chapter only for closed-shell, i.e. spin unpolarized, systems. For spin polarized case the equations are essentially the same but some modifications may be required.

Theorem 1. For any system of interacting particles in an external potential field $V_{ext}(\vec{r})$, the density $n(\vec{r})$is uniquelly determined

In other words, this theorem states that the external potential is a unique functional (a mapping from functions to real numbers) of the density and

$$\begin{aligned} E[n] = T[n] + V_{ne}[n] + V_{ee}[n] &= \int d\vec{r} n(\vec{r}) V_{ext}(\vec{r}) + F_{\mathrm{HK}}[n] \\ &\equiv E_{ext}[n] + F_{\mathrm{HK}}[n] \end{aligned} \tag{2.7}$$

where T, V_{ne} and V_{ee} represent the expectation values of the corresponding operators, e.g. $T \equiv \langle \Psi | \hat{T} | \Psi \rangle$, and $F_{\mathrm{HK}}[n] = T[n] + V_{ee}[n]$ denotes the Hohenberg-Kohn functional that does not depend on the external potential and is universal for all Coulomb systems. The deeper knowledge of this term is unknown at this point. Also, two different external potentials yield inevitably into two different ground state densities.

Theorem 2. A universal functional for the energy $E[n]$ can be defined in terms of the density. The exact ground state is the global minimum value of this functional.

This introduces the variational principle in terms of electron density into DFT. The ground state energy, for a given V_{ext} is the global minimum of the functional $E[n]$ and it is given by the ground state density $n_0(\vec{r})$. Therefore for every given trial density stands equation $E[n] \geq E[n_0] = E_0(\vec{r})$. The proofs of these two theorems are bypassed here and can be found from [61].

To summarize, applying both theorems by Hohenberg and Kohn the many-body SE of N electrons and $3N$ degrees of freedom in an external potential V_{ext} is reduced into a problem of finding the minimum for the functional $E[n]$, which consists of the easily calculated term describing the potential of electrons in the given external potential, and the unknown universal term describing the kinetic energy of the system and electron-electron interactions. As we know that the ground state density is the density giving the minimum value of functional 2.7, the corresponding functional derivative must be zero for the density n_0, i.e.

$$\frac{\delta E[n]}{\delta n(\vec{r})} = \frac{\delta E_{\mathrm{ext}}[n]}{\delta n(\vec{r})} + \frac{\delta F_{\mathrm{HK}}[n]}{\delta n(\vec{r})} = 0, \tag{2.8}$$

which leads to

$$\frac{\delta F_{\mathrm{HK}}[n]}{\delta n(\vec{r})} = -E_{\mathrm{ext}}[\vec{r}]. \tag{2.9}$$

Therefore for given $E_{\mathrm{ext}}(\vec{r})$ we know the functional derivative of $F_{\mathrm{HK}}[n(\vec{r})]$ and the ground state density is the density fulfilling Equation 2.9. However, the construction of F_{HK} is still left unknown.

2.2.2 Kohn-Sham approach

In 1965 Kohn and Sham suggested a way to approximate functional F_{HK} using the idea that the exact ground state density can be written as the ground state density of a system of non-interacting single particles acting as a fictitious reference system [63]. These states ϕ_i are connected to the density as

$$n(\vec{r}) = \sum_{i=1}^{N} |\phi(\vec{r})|^2 , \tag{2.10}$$

where ϕ_i are so called Kohn-Sham orbitals. For every single orbital can be written

$$\left(-\frac{1}{2}\nabla^2 + v_{\mathrm{eff}}\right)\phi_i(\vec{r}) = \epsilon_i \phi_i(\vec{r}), \tag{2.11}$$

which define a set of Schrödinger equations for single electrons with energies ϵ_i. Here v_{eff} denotes the effective potential felt by the electrons and is the sum of the external, Hartree and exchange-correlation potentials,

$$v_{\mathrm{eff}} = v_{\mathrm{ext}} + v_{\mathrm{H}} + v_{\mathrm{XC}}. \tag{2.12}$$

In this system the kinetic energy is known exactly:

$$T_s[n] = -\frac{1}{2}\sum_{i=1}^{N} \langle \phi_i | \nabla^2 | \phi_i \rangle \tag{2.13}$$

and the total energy is just a sum of single particle energies:

$$E_s = \sum_{i=1}^{N} \epsilon_i. \tag{2.14}$$

Here the suffix s means that the energies are not the true kinetic and total energy of the interactive system. However, this way the dominant part of the kinetic energy is sufficiently described. Furthermore, the most significant component of electron-electron interactions can be approximated to be the classical Coulomb interaction, sometimes called Hartree energy, which can be written in terms of electron density as

$$V_H[n] = \frac{1}{2}\int \frac{n(\vec{r}_1)n(\vec{r}_2)}{|\vec{r}_1 - \vec{r}_2|} d\vec{r}_1 d\vec{r}_2. \tag{2.15}$$

The total energy functional is therefore

$$E[n] = E_{\mathrm{ext}}[n] + F_{\mathrm{HK}}[n] = V_{\mathrm{ext}}[n] + T_s[n] + V_H[n] + E_{\mathrm{XC}}[n], \tag{2.16}$$

where *exchange-correlation functional* E_{XC} can be written as

$$E_{\mathrm{XC}}[n] = (T[n] - T_s[n]) + (V_{ee}[n] - V_H[n]), \tag{2.17}$$

from which we can see that E_{XC} is simply the sum of the error made in using a non-interacting kinetic energy and treating the electron-electron interaction classically. The exchange-correlation term contains all the parts that have to be approximated and, in practice, defines therefore the accuracy of the theory. Several different approaches for this term have been generated and the finding of universally well performing functional with reasonable computational cost has become a research field of its own. The choice of which functional to use is not straightforward and is heavily dependent on the system in question. In the next sections a few functionals, including those used in this work, and the theory behind them are introduced briefly.

2.2.3 Exchange-Correlation Functionals

Local Density Approximation

Homogeneous electron gas (HEG) is an example of a system for which exact solutions can be solved and therefore it is an important basis for the construction of XC functionals. In this system the electrons are interacting with constant external positive potential and thus the electron density is constant everywhere in the volume V, $n = \frac{N}{V}$. Local density approximation (LDA), presented by Kohn and Sham in 1965 [63] expands the results obtained for the HEG system to the inhomogeneous case by assuming that the exchange-correlation energy functional depends solely on the value of the electron density at each point $\vec{r}$. The exchange-correlation energy functional in LDA is written as

$$E_{\mathrm{XC}}^{\mathrm{LDA}} = \int d\vec{r} n(\vec{r}) \epsilon_{\mathrm{XC}}[n(\vec{r})], \tag{2.18}$$

where ϵ_{XC} is the exchange-correlation energy density of the homogeneous electron gas and is divided into both exchange and correlation terms, $\epsilon_{\mathrm{XC}} = \epsilon_{\mathrm{X}} + \epsilon_{\mathrm{C}}$. The exchange electron term ϵ_{X} is known directly from the analytic results for HEG. However, there is no explicit expression known for the correlation energy expect at the high- and low density limits. The intermediate values can be fortunately solved utilizing quantum Monte-Carlo simulations [64] yielding accurate parametrizations for the correlation term.

Since the derivatives of the electron density are ignored in Equation 2.18, one could make an assumption that this kind of approach would perform well only for systems with slowly varying electron densities. In reality LDA describes generally surprisingly well covalent, metallic as well as ionic bonds, i.e. systems with strong density variations, yielding reasonable molecular geometries and

vibration frequencies. One explanation for this behaviour is that the significant errors related to the exchange and correlation energies tend to cancel each other [65]. On the other hand LDA satisfies the summing rules associated with exact exchange correlation electron holes [66, 67]

$$\begin{aligned} \int n_{\mathrm{X}}(\vec{r}, \vec{r}+\vec{u}) d\vec{u} &= -1 \\ \int n_{\mathrm{C}}(\vec{r}, \vec{r}+\vec{u}) d\vec{u} &= 0. \end{aligned} \tag{2.19}$$

However, e.g. the atomization energies tend to be strongly overestimated [68].

Generalized Gradient Approximation

The natural expansion of LDA is to append the information about the charge density with the gradient, i.e. the magnitudes and directions of local variations in the charge cloud. Thus the term generalized gradient approximation (GGA). The GGA energy functionals, the idea introduced by Hohenberg and Kohn in 1964 [62], can be expressed in general form

$$E_{\mathrm{XC}}^{\mathrm{GGA}}[n] = \int d\vec{r} f(n, \nabla n), \tag{2.20}$$

where f is some function depending on the density and its gradient. Again, this energy functional can be separated into the exchange and correlation terms. In all GGAs the exchange functional is written as

$$\epsilon_{\mathrm{X}}[n, s] = \epsilon_{\mathrm{X}}^{\mathrm{LDA}}[n] F_{\mathrm{X}}[s], \tag{2.21}$$

where the LDA exchange energy density $\epsilon_{\mathrm{X}}^{\mathrm{LDA}}$ is multipled by so called enhancement factor F_{X} due to density gradients. The variable s is a reduced density gradient

$$s = \frac{|\nabla n|}{2(3\pi^2)^{1/3} n^{4/3}}. \tag{2.22}$$

Different flavours of GGA functionals differ by the enchancement factor. For example, PW91 functional [69], is constructed to fulfill as many as possible known constraints of the exact functional like the sum rules of the XC hole. PBE functional, which is novadays one of the most popular functionals, mimics PW91 but is constructed with simpler derivation and lighter parametrization while all energetically significant physical cosntraints are included. The enhancement factor in Equation 2.21 for PBE is given by

$$F_{\mathrm{X}}^{\mathrm{PBE}}(x) = 1 + \kappa \left(1 - \frac{1}{1 + x/\kappa}\right), \tag{2.23}$$

where $x = \mu s^2$. The non-empirical parameters $\kappa = 0.804$ and $\mu = 0.2195$ can be determined when demanding that the exchange gradient correction cancels off when $s \to 0$ and Lieb-Oxford bound to be obeyed [70].

GGA type of functionals have been very popular due to high accuracy-to-cost ratio for a wide range of applications. For example, the PBE improvement from LSDA is significant when comparing equilibrium lattice constants, bulk moduli and cohesive energies for a range of different solids and even outperforms more complex functionals in many cases [71]. However, GGA functionals in general seem to have problems at describing the physics and chemistry of surfaces fundamentally [72] without the proper accounting of van der Waals (vdW) dispersion interactions [73] because, by construct, the long-range, non-local correlations are neglected.

Bayesian Error Estimation Functional with van der Waals

To put it simple, XC functionals can be developed by two ways: construction of constraint satisfaction by reduction of exact density functional and fitting to empirical data. GGA is an example of the former one, while BEEF-vdW (Bayesian Error Estimation Functional with van der Waals) goes beyond GGA by incorporating 31 empirical parameters fitted using Bayesian error estimation [74] taking into account vdW dispersion interactions. The exchange-correlation energy functional is

$$E_{\mathrm{XC}} = \sum_{m=0}^{M_x-1} a_m E_m^{\text{GGA-x}} + \alpha_c E^{\text{LDA-c}} + (1-\alpha_c) E^{\text{PBE-c}} + E^{\text{nl-c}}, \tag{2.24}$$

where $M_x = 30$ and α_c is a mixing parameter. GGA exchange energy has been expanded on orthogonal Legendre polynomials parameters a_m being the corresponding expansion coefficients. The last term is vdW-DF2 type nonlocal correlation term [75] having a form

$$E^{\text{nl-c}}[n] = \frac{1}{2} \int n(\vec{r}) \gamma(\vec{r}, \vec{r}+\vec{u}) n(\vec{u}) d\vec{r} d\vec{u}, \tag{2.25}$$

where $\gamma(\vec{r}, \vec{r}+\vec{u})$ is nonlocal interaction kernel function. The training datasets used for fitting include quantities representing chemistry, solid state physics, surface chemistry, and vdW dominated interactions making BEEF-vdW an attractive choice for surface chemistry calculations.

Hubbard U Parameter For Correlated Systems

The construction of Kohn-Sham functionals in an approximative way leads inevitably into some known problems. Semi-local approximations, i.e. functionals

in which $\epsilon_{\mathrm{XC}}(\vec{r})$ is found from the electron spin-density in an infinitesimal vicinity of $\vec{r}$ (such as LDA and GGA), often fail to describe the electronic structure of strongly correlated systems, typically having incompletely filled d- or f-electron shells with narrow energy bands, due to so called self-interaction error. This error arises from the Hartree energy functional in Equation 2.16 which includes the density of all electrons in the system. Applying this equation to an one-electron system with wave-function $\phi(\vec{r})$ leads to non-zero Hartree term which is not canceled out by a similar term in exchange-correlation term.

Many transition-metal compounds are Mott-Hubbard or charge-transfer insulators, but DFT predicts metallic state The total energy using DFT+U theory summarizing the essence of the method is

$$E_{\mathrm{DFT+U}} = E_{\mathrm{DFT}} + E_{\mathrm{U}}[\rho^a] = E_{\mathrm{DFT}} + \sum_a \frac{U_{\mathrm{eff}}}{2}\mathrm{Tr}(\rho^a - \rho^a\rho^a), \tag{2.26}$$

where U_{eff} is the effective interaction parameter and ρ^a is the atomic orbital occupation matrix. This introduces an additional repulsive term for a subset of the system - the electrons that should be localized - while all other electrons are treated within the standard approach. It is noteworthy that utilizing this simple and inexpensive addition to LDA or GGA theory leads often to correct reproduction of magnetic ground states, electronic structure and relative energetics for systems in which the standard method fails [76, 77, 78, 79]. However, the transferability of interaction parameter U_{eff} has been found to be limited across compounds differing only by the oxidation state [80] which introduces a limitation to the method.

2.3 Numerical implementation of the DFT theory

In practice, the seeking of minimum energy (or corresponding minimum energy electron density) starts with an educated guess for the initial density $n_{\mathrm{init}}(\vec{r})$ which gives an initial value of total energy in Equation 2.16 and effectively also to the effective potential 2.12. Then Kohn-Sham orbitals can be solved from Equation 2.11 which gives the new electron density $n(\vec{r}) = \sum_{i=1}^{N} |\psi_i|^2$. If the corresponding wave function is the same within some predetermined convergence criteria, the calculation can be stopped, otherwise new guess for the density is constructed and the cycle starts over until the convergence has been reached. This is called self-consistent field (SCF) procedure.

To represent each object in Kohn-Sham method in a computer program, some further approximations and numerical tricks for the description of Kohn-

Sham orbitals and evaluation of the total energy have to be made. Generally speaking, the orbitals are written as a sum of some basis functions and only the coefficients are stored into the computer memory. Then, the Kohn-Sham Schrödinger equations are written in a matrix form

$$H_j c_{ij} = \epsilon_i c_{ij}. \tag{2.27}$$

Alternatively, the orbitals can be described within a real space grid. The KS-orbitals in this thesis work were expanded by plane waves and real space grids which are discussed in this chapter.

2.3.1 Periodic systems

Often large but finite systems possess periodicity, when examined closely, thus it becomes reasonable to model them as periodic systems which are infinite in one to three dimensions. For example, bulk materials can often be constructed using unit cells consisting only of a few atoms and applying periodic boundary conditions in three dimensions. Similarly corresponding models for surfaces can be constructed from a thick enough slab of given material having periodic boundary conditions in the surface plane. The effects in relation to e.g. the coverage or concentration (molecule adsorption on surfaces, oxygen vacancy concentration etc.) can be studied by simply defining larger supercells consisting of different number of the simplest possible cell.

2.3.2 Plane-Waves

In plane-wave approach [81] each orbital is expanded as a Fourier series and corresponding G-space coefficients are stored on a regular grid. The advantage of this method is that because each basis function is a spatially delocalized plane-wave, the basis is independent on the coordinates of the atoms in the system. Thus, no basis set related error corrections are needed. The orbitals ψ_i can be expressed in a very compact form

$$\psi_i(\vec{r}) = \sum_{\vec{k}} c_{\vec{k}i} e^{i\vec{k}\vec{r}}, \tag{2.28}$$

where $\vec{k}$ is a vector in G-space. However, this general description of the basis functions requires very large basis sets in order to acquire accurate results. In practice, the plane-wave basis set is defined by choosing a cut-off energy E_{cut} which designates the upper limit for the kinetic energy of plane-waves.

To perform mathematical operations involving the wave-functions, densities and potentials, Fourier transforms between the real and reciprocal must be made. Since these operations are highly non-local in nature, the parallelization becomes difficult.

2.3.3 Real Space Grids

An alternative for basis functions based expansion of KS-orbitals is to use real space grids. In this method the orbitals are represented as a matrix of numerical values within a discrete 3D grid. The KS Hamiltonian is then applied on the grid, thus the potentials and density are discretized. The significant advantage of this method is the possibility for massive parallelization of computations with excellent scalability by dividing the grid points between different processors. Also, periodic and non-periodic systems can be treated equally in contrast to plane-wave approach which requires periodical boundary conditions.

In the grid formalism continuous potential $V(\vec{r})$ and electron density $n(\vec{r})$ are discretized as

$$\int V(\vec{r})n(\vec{r}) \sim \Omega_G \sum_{\vec{G}} V(\vec{G})n(\vec{G}), \tag{2.29}$$

where discrete functions are defined in grid points $\vec{G} = (G_x, G_y, G_z)$ and Ω_G is the correponding volume defined by the spacing of the grid points h. For the partial derivatives of functions approximations have to be made. E.g. in fixed point G_0 with respect to x component of vector $\vec{r}$ of a wave-function can be written [82] as

$$\left[\frac{\partial^2 \psi_i(\vec{r})}{\partial x^2}\right]_{x,y,z} \sim \sum_{-m}^{m} c_m \psi_i(G_x + mh, G_y, G_z), \tag{2.30}$$

where c_m are grid dependent coefficients, m is an integer, which determines how many grid points is used for the approximation, $\vec{G}$ is a point in real space grid corresponding to $\vec{r}$. With the help of discrete Laplacians, constructed using Equation 2.30, the total energy of the system can be calculated [82].

2.3.4 Separation of core and valence states

The single particle states have typically rapidly oscillating features near the atomic nuclei due to high momentum while the states further away (the valence electrons) behave more smoothly. As a result, for accurate calculations, one would have to use very fine real space grid or a high number of plane-waves to describe the states near nuclei properly without leading to chaotic behavior. On

the other hand, the requirements for equally accurate calculations of valence states are lower. Since the contribution of the inner states to the chemical properties is typically minor, raises a question if these two distinct types of electronic states could be separated somehow. Fortunately, there are methods available to address this problem and two formalisms are discussed briefly next.

Pseudopotentials

The system can be simplified with the help of so called pseudopotentials (or effective potentials) which are used as an approximation for the core states, including the nucleus and strongly bound core electrons, of the system [81]. The element dependent effective potential basically eliminates the highly oscillating inner states of the system from the calculations by replacing them with much smoother wavefunctions while only the valence states are solved from the KS equations.

All pseudopotentials are described by their cut-off radius which is a distance from the nucleus beyond of which the wave-function is equal to a single particle wave-function from an all-elecron calculation. Also, the charges calculated both by pseudo and all-electron densities must be equal, which introduces a norm conservation rule. The psedopotentials need to be calculated only once for each type of atom effectively reducing the number of required calculations of KS equations. There are many types of pseudopotentials available which all have their advantages and drawbacks [83] but there is evidence that this formalism can be applied in both effective and transferable way at least in certain cases [84, 66]. However, one has to remember that all information of the full wave function close to the nuclei is lost, which may prevent the calculation of certain parameters accurately [85]. Also, one has to have beforehand knowledge if the chosen type of pseudopotential is suitable for the description of atoms in the particular chemical environment which raises concerns about the reliability of calculations when completely new materials are studied.

Projector-augmented wave method

An alternative method for avoiding the need of a large set of plane waves or very fine grid for correct description of electronic states is projector-augmented wave (PAW) method which is a more general approach of pseudopotentials. However, the true wavefunction is conserved instead of using auxiliar states and the potential is not directly modified. For mathematically more comprehensive

description of the method the original paper by Blöch [86] as well as the material provided by GPAW developers [85] are recommended.

The PAW formalism relies on the existence of a linear transformation $\hat{T}$ which transforms an auxiliary smooth wavefunction $|\tilde{\psi}_n\rangle$ to the true all electron KS single particle wave function $|\psi_n\rangle$ inside an atom-specific augmentation region $\left|\vec{r} - \vec{R}^a\right| < r_c^a$ with cut-off radii r_c^a.

$$|\psi_n\rangle = \hat{T}|\tilde{\psi}_n\rangle. \tag{2.31}$$

Instead of usual KS equations, the transformed equations

$$\hat{T}^\dagger \hat{\mathcal{H}} \hat{T}|\tilde{\psi}_n\rangle = \epsilon_n \hat{T}^\dagger \hat{T}|\tilde{\psi}_n\rangle \tag{2.32}$$

are solved. Inside the augmentation sphere the true wavefunction is expanded with the help of partial waves ϕ_i^a. In turn, for each of these partial waves a corresponding smooth partial wave $\tilde{\phi}_i^a$ can be defined requiring that

$$|\phi_i^a\rangle = (1 + \hat{T}^a)|\tilde{\phi}_i^a\rangle \Leftrightarrow \hat{T}^a|\tilde{\phi}_i^a\rangle = |\phi_i^a\rangle - |\tilde{\phi}_i^a\rangle \quad \forall i, a. \tag{2.33}$$

All in all, the expression for transformation $\hat{T}$ is

$$\hat{T} = \hat{1} + \sum_a \sum_i (|\phi_i^a\rangle - |\tilde{\phi}_i^a\rangle)\langle \tilde{p_i^a}|, \tag{2.34}$$

where $|\tilde{p_i^a}\rangle$ are some fixed functions called smooth projector functions. The all electron KS wave function is then acquired from the function

$$\psi_n(\vec{r}) = \tilde{\psi}_n(\vec{r}) + \sum_a \sum_i (\phi_i^a(\vec{r}) - \tilde{\phi}_i^a(\vec{r}))\langle \tilde{p_i^a}|\tilde{\psi}_n\rangle, \tag{2.35}$$

where the smooth wave function $\tilde{\psi}_n(\vec{r})$ is solved from Equation 2.32. As can be seen, the transformation consists of three parts: the partial waves $\phi_i^a(\vec{r})$, the corresponding smooth partial waves $\tilde{\phi}_i^a(\vec{r})$ and the smooth projector functions $\tilde{p_i^a}(\vec{r})$. The partial waves and projector functions are system independent, hence they can be calculated only once and stored into database from where they are read when needed. Note also that in Equation 2.35 the only component that is needed to be solved outside the augmentation sphere is numerically convenient smooth wave function $\tilde{\psi}_n(\vec{r})$. This way access to full all-electron wavefunctions (and density) is available while there is no need to deal with the computationally challenging inert core electrons.

2.4 Atomistic Thermodynamics

Strictly speaking, all evaluated physical quantities obtained by DFT calculations are only valid at $T = 0$ K and $p = 0$ atm. There are fortunately superimposed methods to link the concepts of statistical mechanics and thermodynamics with atomistic electronic structure calculations. The dependence on temperature and pressure can be considered by applying so-called *ab initio* atomistic thermodynamics theory [87] which was used to predict the relative stability of surfaces with varying oxygen content in different surrounding conditions. Using this theory we calculate the surface free energies as

$$\gamma(T,p) = \frac{1}{2A}\left[G^{\text{slab}} - \frac{N_{\text{m}}}{x} g^{\text{bulk}}_{\text{m}_x\text{o}_y} + \left(\frac{y}{x}N_{\text{m}} - N_{\text{o}}\right)\mu_{\text{O}}(T,p)\right], \tag{2.36}$$

where A is the surface area of the slab unit cell, G^{slab} the slab free energy, N_{m} and N_{o} the number of metal and oxygen atoms respectively, $g^{\text{bulk}}_{\text{m}_x\text{o}_y}$ the free energy of bulk oxide per formula unit and $\mu_{\text{O}}(T,p)$ the chemical potential of oxygen atom in gas phase at temperature T and pressure p. Following assumptions are made:

$$\begin{aligned} G^{\text{slab}} &\approx E^{\text{slab}}_{\text{DFT}} \\ g^{\text{bulk}}_{\text{m}_x\text{o}_y} &\approx \frac{x+y}{N^{\text{bulk}}} E^{\text{bulk}}_{\text{DFT}}. \end{aligned} \tag{2.37}$$

The chemical potential of oxygen is calculated as follows

$$\begin{aligned} \mu_{\text{O}}(T,p) &= \frac{1}{2}E^{\text{total}}_{\text{O}_2} + \frac{1}{2}E^{\text{ZPE}}_{\text{O}_2} + \Delta\mu_{\text{O}}(T,p) \\ &= \frac{1}{2}E^{\text{total}}_{\text{O}_2} + \frac{1}{2}E^{\text{ZPE}}_{\text{O}_2} + \Delta\mu_{\text{O}}(T,p^0) + \frac{1}{2}k_B T \ln\frac{p}{p^0}, \end{aligned} \tag{2.38}$$

where p^0 is standard pressure, $E^{\text{total}}_{\text{O}_2}$ is the calculated total energy of an oxygen molecule, $E^{\text{ZPE}}_{\text{O}_2}$ the zero-point energy of oxygen molecule, $\Delta\mu_{\text{O}}(T,p^0)$ relative oxygen chemical potential at standard pressure (tabulated values) and k_B is the Boltzmann constant.

The minimum value of the oxide surface free energy can be determined from the limit at which the bulk oxide becomes thermodynamically more favorable than an equivalent amount of bulk metal and oxygen in gas phase, namely

$$g^{\text{bulk}}_{\text{m}_x\text{o}_y} \leq x g^{\text{bulk}}_{\text{m}} + y\mu_{\text{o}}. \tag{2.39}$$

Using equation 2.38 yields

$$\begin{aligned} \Delta\mu_{\text{O}}(T,p) &> \frac{1}{y}(g^{\text{bulk}}_{\text{m}_x\text{o}_y} - x g^{\text{bulk}}_{\text{m}} - \frac{y}{2}E^{\text{tot}}_{\text{O}_2}) \\ &= \frac{1}{y}H^0_f(0,0), \end{aligned} \tag{2.40}$$

where $H_f^0(0,0)$ is the enthalpy of formation of the bulk oxide at $T = 0K$. The maximum value of $\Delta\mu_O(T,p)$ is set to total energy of oxygen in gas phase, i.e., $\Delta\mu_O(0,p^0) = \frac{1}{2}E_{O_2} = 0$, which corresponds to the oxygen-rich condition.

2.5 Bader charge analysis

Quantum mechanical theory does not provide any direct information about the charges of molecules or individual atoms since the output is only the continuous charge density. Understanding the mechanics of many chemical reactions often require, however, information about the oxidation state of individual atoms and fragments of the molecules. Therefore a standalone method to partition the electron density, which by definition does not belong to any individual atom, between different atoms is needed.

Many different schemes have been proposed to address this problem and they can be divided roughly into two categories: based on partitioning either the space or the charge density. For example in Voronoi polyhedra -approach each point in real space is assigned to the nearest atom and the charge of the atom is evaluated by integrating the charge density over the assigned spatial points. This kind of primitive scheme does not take into account different atomic types leading to possibly unreasonable results. However, the method can be modified e.g. moving the dividing planes according to the relative atomic sizes of the bonding atoms, which makes the results more reasonable [88].

In contrast to Voronoi approach, Bader charge analysis is based solely on the real-space electron density i.e. the atomic positions are not used as an input [89, 90]. The algorithm finds the critical points (maximum values) of the electron density which are usually, but not necessarily, at the nuclei of the atoms. The real-space is then divided into sub-volumes, referred as Bader-volumes, centered by the critical points and separated by so called zero-flux surfaces determined by

$$\nabla n(\vec{r_s}) \bullet u(\vec{r_s}) = 0, \tag{2.41}$$

where $u(\vec{r_s})$ is the unit vector normal to the surface at r_s. The electron density is then integrated over the Bader-volume to determine the charge of an atom. This method provides a highly intuitive and well defined way to determine partial charges of individual atoms and molecules.

In this work Bader charge analysis was used to determine the atomic charges and the changes in oxidation states upon removal of an oxygen atom from metal oxide structure or adsorption of molecules on Ag/MgO surfaces. When changes

of the charge state of individual atoms were considered, the difference between the final and initial state $\Delta q(A)$ was calculated as

$$\Delta q(A) = q_{\text{final}}(A) - q_{\text{initial}}(A) \tag{2.42}$$

negative value implicating an increase of the electron density around the corresponding atom.

2.6 Local Density of States

The density of states (DOS) $\rho(\epsilon)$ describes the amount of states having an energy between interval $[\epsilon, \epsilon + \mathrm{d}\epsilon]$ and available to be occupied. Using system eigenstates it can be defined as

$$\rho(\epsilon) = \sum_n \langle \psi_n | \psi_n \rangle \delta(\epsilon - \epsilon_n), \tag{2.43}$$

where ϵ_n is the eigenvalue of state ψ_n. In general DOS defined as in Equation 2.43 describes the average over the space occupied by the system. This can be expressed as

$$\rho(\epsilon) = \int \mathrm{d}\vec{r} \sum_n \langle \psi_n | \vec{r} \rangle \langle \vec{r} | \psi_n \rangle \delta(\epsilon - \epsilon_n), \tag{2.44}$$

where unity operator $\hat{1} = \int \mathrm{d}\vec{r} |\vec{r}\rangle\langle\vec{r}|$ was used. Now

$$\rho(\vec{r}, \epsilon) \equiv \sum_n \langle \psi_n | \vec{r} \rangle \langle \vec{r} | \psi_n \rangle \delta(\epsilon - \epsilon_n) \tag{2.45}$$

is the local density of states (LDOS) which represents DOS of state ψ_n at each point $\vec{r}$ separately. To quantify differences between different LDOS, it is often useful to define band center

$$\epsilon_x = \frac{\int_{E_f - E_c}^{E_f} E \rho_x(E) \mathrm{d}E}{\int_{E_f - E_c}^{E_f} \rho_x(E) \mathrm{d}E} \tag{2.46}$$

for band x, where E_f is the Fermi-energy and E_c is the cut-off energy which is in principle $-\infty$ but for numerical reasons it was set to -10 eV.

2.7 Apparent activation energy

One of the challenges in DFT calculations is the interpretation of the results and comparing to the real experiments in a relevant manner. For example when considering different reactions, where two or more molecules react with each

other, it is important to choose the correct baseline for the energy to make relevant comparison to the possible experimental data.

Let us consider a catalytic reaction where two molecules A and B coming from the gas phase adsorb and form a product on a surface and then desorb into gas phase. The overall reaction can be described by equations

$$(1) \qquad \mathrm{A} + \square \underset{\mathrm{k_1}^-}{\overset{\mathrm{k_1^+}}{\rightleftharpoons}} \mathrm{A}_\square \tag{2.47}$$

$$(2) \qquad \mathrm{B} + \square \underset{\mathrm{k_2}^-}{\overset{\mathrm{k_2^+}}{\rightleftharpoons}} \mathrm{B}_\square \tag{2.48}$$

$$(3) \qquad \mathrm{A}_\square{}^+ \, \mathrm{B}_\square \underset{\mathrm{k_3}^-}{\overset{\mathrm{k_3^+}}{\rightleftharpoons}} \mathrm{AB}_\square{}^+ \, \square \tag{2.49}$$

$$(4) \qquad \mathrm{AB}_\square \underset{\mathrm{k_4^-}}{\overset{\mathrm{k_4^{++}}}{\rightleftharpoons}} \mathrm{AB}^+ \, \square \tag{2.50}$$

where A/B is an adsorbate, $\square$ is an empty surface site and $\mathrm{A/B}_\square$ is an adsorbed species. The equilibrium constants are defined as $\mathrm{K_x} = \frac{\mathrm{k_x^+}}{\mathrm{k_x^-}}$. For each step the corresponding rates can be calculated as

$$r_1 = k_1^+ p_A \theta_\square - k_1^- \theta_A \tag{2.51}$$

$$r_2 = k_2^+ p_B \theta_\square - k_2^- \theta_B \tag{2.52}$$

$$r_1 = k_3^+ \theta_A \theta_B - k_3^- \theta_{AB} \theta_\square \tag{2.53}$$

$$r_1 = k_4^+ \theta_{AB} - k_4^- p_{AB} \theta_\square \tag{2.54}$$

with constraint

$$\theta_\square + \theta_A + \theta_B + \theta_{AB} = 1 \tag{2.55}$$

since the number of cites on a catalytic surface is constant. If we assume that the surface reaction (3) is the rate-determining step (RDS) and other steps are relatively fast, i.e. the reactions are in quasi-equilibrium, we may approximate that $r_1, r_2, r_3 \approxeq 0$ and solve the coverages

$$\theta_A = K_1 p_A \theta_\square \tag{2.56}$$

$$\theta_B = K_2 p_B \theta_\square \tag{2.57}$$

$$\theta_{AB} = K_4^{-1} p_{AB} \theta_\square. \tag{2.58}$$

Using these equations the coverage of empty sites can be expressed as

$$\theta_\square = \frac{1}{1 + K_1 p_A + K_2 p_B + K_4^{-1} p_{AB}}. \tag{2.59}$$

The overall rate of the reaction is then

$$\begin{aligned} r = r_3 &= k_3^+ \theta_A \theta_B - k_3^- \theta_{AB} \theta_\square \\ &= k_3^+ K_1 K_2 p_A p_B \left(1 - \frac{p_{AB}}{p_A p_B K_G}\right) \left(\frac{1}{1 + K_1 p_A + K_2 p_B + K_4^{-1} p_{AB}}\right)^2 \end{aligned} \tag{2.60}$$

One more approximation can be made related to the partial pressures of A, B and AB. The product AB concentration is usually kept low to enhance the overall reaction. In this case the reverse reaction of Equation 2.54 can be neglected and we can make an approximation $p_{AB} \approx 0$ which greatly simplifies equation 2.60 to

$$r = \frac{k_3^+ K_1 K_2 p_A p_B}{(1 + K_1 p_A + K_2 p_B)^2} \tag{2.61}$$

Clearly the assumption of rate-determining step present in the reaction limits the usability of this approach but this is usually very justified approximation in catalytic reactions since the reaction energies for adsorption and desorption are typically low. However, change in reaction conditions might shift the RDS to a different elementary step. For example, in ultrahigh vacuum conditions the partial pressures of A and B may become so small that the rates of adsorption limit the overall reaction.

Now, the apparent activation energy E^a_{app}, which is expressed in the experiments, is

$$E^a_{\text{app}} = RT^2 \frac{\partial \ln r}{\partial T} = \ldots = E^a + (1 - 2\theta_A)\Delta H_A + (1 - 2\theta_B)\Delta H_B + 2\theta_{AB}\Delta H_{AB}, \tag{2.62}$$

where E^a is the activation energy of elementary step (3), i.e. the reaction barrier of A+B→AB, and ΔH_X is adsorption enthalpy of species X. The more comprehensive derivation of previous equation is presented in reference [91].

The important thing to note is that the apparent activation energy given by Equation 2.62 does not equal only the activation energy of RDS but depends also on the adsorption enthalpies and coverages of all molecules participating to overall reaction. Hence, the apparent activation energy given by experiments depends considerably on the conditions under which the experiments have been performed. When for both species A and B the coverage $\theta < \frac{1}{2}$, which is a reasonable approximation in many realistic conditions, the apparent activation energy is inevitably lower than the RDS reaction barrier E^a (assuming the adsorptions are thermodynamically favorable, i.e. $\Delta H < 0$).

2.8 Computational details

In all calculations presented in this thesis real-space implementation of projector-augmented wave method has been used within *GPAW* program [92]. *GPAW* is an open-source program package utilizing *Atomic Simulation Environment* (ASE) [93] for the description of atomic positions, molecular dynamics, analysis, optimization and visualization. GPAW implements the projector augmented method in a real space grid and more information can be obtained from the literature [92].

2.8.1 CLC materials

Model systems

The reduced form of Mn_2O_3, Mn_3O_4, has both di- and tri-valent manganese atoms and hausmannite crystal structure (space group 141/amd) with Mn^{3+} occupying tetrahedral sites and Mn^{2+} occupying octahedral sites [94] (purple and blue atoms in Figure 2.1(a)). Mn_3O_4 expresses ferri-magnetic behaviour with Mn^{3+} ions forming a spiral-magnetic spin structure[95]. However, purely ferromagnetic ordering was used in the calculations due to numerical practicality. This is justifiable since it is known to yield very comparable results compared to the experimental findings [76].

Less reduced Mn_2O_3 can appear in two different phases, α and γ forms, α phase being the dominant phase in nano scale under CLC conditions [96, 97]. In α-Mn_2O_3 bulk the Mn atoms are in +3 oxidation state and coordinate octahedrally while the coordination of oxygen ions is tetrahedral. The structure belongs to bixbyite $Ia\overline{3}$ space group with cubic unit cell having 32 Mn atoms and 48 O atoms (presented in Figure 2.1(b)). The cubic structure undergoes several orthorhombic distortions in relatively low temperatures below $\sim$ 300 K [96] but in this study the high temperature cubic bixbyite structure was used throughout the work since it is the dominant phase in CLC conditions.

The magnetic structure of α-Mn_2O_3 is rather complex and it has not been solved completely[98] but experimental studies have found evidence for various antiferromagnetic magnetic orderings[97]. However, in the study the manganese atoms were assumed to be at the high spin configuration with ferromagnetic coupling between the ions in order to reduce the problems arising from the multiple possible antiferromagnetic states of the system. The comprehensive justification for this approach is presented by Busch *et. al.* [99]. Also, the difference between the antiferromagnetic and ferromagnetic coupling was tested

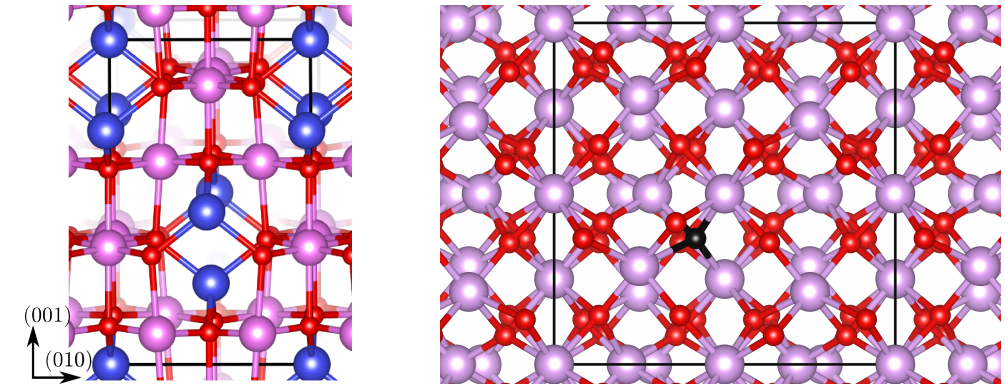

(a) Mn_3O_4 **(b)** Mn_2O_3

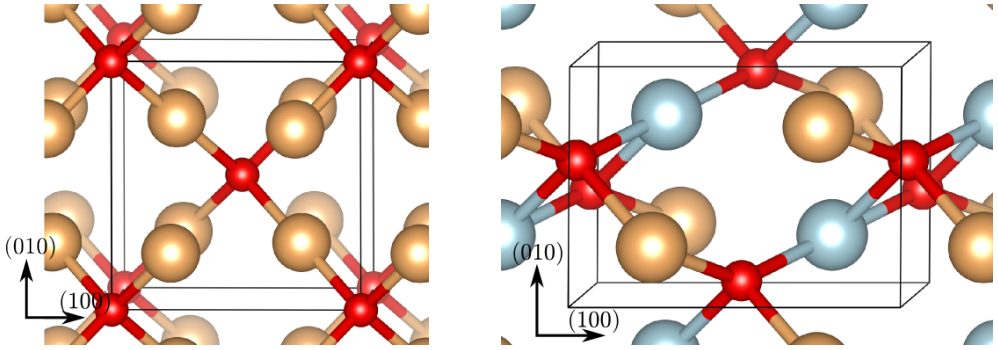

(c) Cu_2O **(d)** CuO

Figure 2.1. *The smallest unit cells of a) Mn_2O_3, b) Mn_3O_4, c) CuO and d) Cu_2O. The bigger (smaller) balls represent cation (oxygen) atoms. In figure (a) the blue (purple) balls represent Mn(II) (Mn(III)) atoms. The antiferromagnetic spin structure of CuO is shown in figure (d): cations with spin up (down) are colored brown (blue).*

in the bulk and the differences between the oxygen vacancy formation energy and diffusion barrier were negligible (∼0.1 eV)

The crystal structure of cuprous oxide Cu_2O is relatively simple and highly symmetric since it has a cubic lattice with two sub-lattices: oxygen atoms in a body-centred cubic (bcc) sub-lattice and copper atoms in a face-centered cubic (fcc) lattice occupying the tetrahedral sites relative to the oxygen atoms (Figure 2.1(c)). Despite of the simplicity, the low coordination crystal structure is rather unusual and for metal oxides only two other similar structures are known, i.e. Ag_2O and Pb_2O [100]. The lattice is characterized by space group $Pn\bar{3}m$ and it expresses diamagnetic properties [101, 102].

Compared to Cu_2O, cupric oxide CuO has considerably more complex low

symmetry tenorite crystal structure[103] with monoclinic unit cell and space group *C2/c* containing four copper and oxygen atoms. The copper atoms are coordinated in square planar configuration by 4 oxygen atoms. The magnetic structure of ground state CuO is antiferromagnetic [104]. The smallest possible unit cell and AFM spin ordering are shown in Figure 2.1(d).

Parameters of the calculations

To describe exchange and correlation effects, generalized gradient approximation (GGA) using PBE exchange correlation functional [68] was employed in the DFT calculations. To take into account strong correlation effect among the partially filled 3d states in Cu and Mn metal oxides, the Hubbard parameter U was introduced. The values of 4.0 and 3.9 eV, which are designed to match the experimental enthalpies of oxidation for Cu_2O and MnO, were adopted from reference [76]. Calculations were treated as spin-polarized except in the case of Cu_2O.

First, the lattices were built based on the information about the crystal structure. The lattice parameters of all bulk structures were solved using implemented `StrainFilter` method which relaxes the unit cell volume while keeping the scaled positions fixed. The unit cell under review was relaxed until the forces were below 0.035 eV/Å on each atom. After the unit cell relaxation the atomic positions were allowed to relax using the same relaxed force criteria. If the energy decrease upon relaxation was $>\sim$ 0.1 eV new iteration of `StrainFilter` -relaxation cycle was performed.

For each bulk structure the lattice parameters were optimized separately. In calculations a force convergence criterion of 0.035 eV/Å was set. The suitable Monkhorst-Pack k-point grids were tested for each material separately. Since this work is focused on the comparison of the oxygen vacancy stability and oxygen diffusion energetic properties of different materials, the convergence of the oxygen vacancy formation energy was tested with respect to the number of k-points separately. The grid spacing of 0.16 Å was used throughout the work. As the unit cells of each oxide are very different in size, larger cells for Mn_3O_4, Cu_2O and CuO were generated to match the separation distances between the mirror images of vacancies resulting from the periodic boundary conditions. The cells (1x1x1)Mn_2O_3, (2x2x1)Mn_3O_4, (2x2x2)Cu_2O and (2x3x2)CuO all have lattice size of $\sim$ 10 Å along each direction thus making the single vacancy separation distances comparable. For these larger cells sufficient k-point grids, yielding to accurate description of vacancy formation energies and diffusion

barriers, were Γ only, 1x1x2, 2x2x2 and Γ only, respectively. Using these parameters allows comparison of the results obtained from each materials with each other.

The formation enthalpies of studied oxides were calculated using equation

$$\Delta H = E^{\text{bulk}}_{M_xO_y} - xE^{\text{bulk}}_{\text{M}} - y\frac{1}{2}E_{\text{O}_2}, \tag{2.63}$$

where $E^{\text{bulk}}_{M_xO_y}$, $E^{\text{bulk}}_{\text{M}}$ and E_{O_2} are the calculated total energies of oxide bulk, corresponding metal bulk and an oxygen molecule, respectively. For pure Cu bulk, the ordinary fcc crystal structure was employed in calculations. Manganese metal bulk is a little problematic, however, since several stable phases have been identified [105]. In this work pure high temperature γ phase manganese with a fcc crystal structure [106] was chosen as the metal bulk reference since the structure of room temperature α manganese is particularly complex due to its geometrical and magnetic properties [107]. Moreover, the high temperature γ phase is more relevant choice for the CLC applications. Furthermore, Hafner and Hobbs [108] reported that the DFT computed energy difference between α and γ phases is only in the order of < 1 meV.

Oxygen vacancy stability was examined by removing one oxygen atom from the structure. This oxygen-lacking structure was fully relaxed and the vacancy formation energy per oxygen atom can be calculated as

$$E_{V_{\text{O}}} = E_{\text{vac}} + \frac{1}{2}E_{\text{O}_2} - E_{\text{bulk}}, \tag{2.64}$$

where E_{vac} is the calculated energy of the structure with a created oxygen vacancy, E_{O_2} is the energy of single oxygen molecule in vacuum calculated using similar methods as the oxide and E_{bulk} is the energy of the corresponding bulk oxide structure. It has to be noted that the GGA method overestimates the binding energy of a O_2 molecule by $\sim$0.7 eV [76]. Due to this the vacancy formation energy is expected to be underestimated. However, the trends in oxygen vacancy stability among different metal oxides can be reasoned to be unaffected and this constant error will be neglected throughout the rest of the report. In relation to vacancy formation energies, structure relaxation energies $E_{R_{\text{O}}}$ are also discussed describing the energy difference between the non-relaxed and the fully relaxed structure once a vacancy is created. The magnitude of this energy tells about the driving forces trying to minimize the structural energies.

The diffusion of oxygen atoms into a created vacancy was studied using nudged elastic band (NEB) method [109] which can be used to find the minimum energy migration path between two images presenting the initial and final

state of the system. A constraint method, in which migrating oxygen atom is moved manually restricting the movement of the atom upon relaxation into the plane perpendicular to the migrating path, was used for validating the NEB calculations in selected cases to verify the saddle point energy. The images were relaxed until the forces acting to each atom were smaller than 0.08 eV/Å using either of the methods.

The surfaces were constructed for each of the bulk structures. The most stable surfaces of each material were chosen from the literature to determine oxygen vacancy stability and vacancy diffusion properties at the vicinity of the surfaces and compare them to the corresponding bulk structures. Similarly to bulk structures, generating the smallest possible unit cell may lead to different vacancy concentrations on the surfaces. Therefore (2x2) Mn_3O_4(001), (1x1) Mn_2O_3(110), (2x2) Cu_2O(111) and (3x2) CuO(111) surface unit cells were generated for the calculations. This yielded the separation distance between the mirror images of the surface vacancies $\sim$ 10 Å in both x and y directions. Oxygen vacancy formation energies for the surface structures were determined both at the surface (first layer) and subsurface (second layer) sites. The diffusion between the first and second layer was studied by choosing the lowest energy surface site vacancy as the initial state. Then, different routes of diffusion were considered and the lowest migration barriers are presented and discussed.

The slab models consisted of 4-7 formula unit (f.u.) layers (corresponding to 8-18 atomic layers) and at least 10 Å vacuum on both sides of the slab to ensure the complete vanishing of the wave function before the cell edge. In all different calculations the atomic positions of the one to three undermost f.u. layers were fixed allowing 3-4 topmost layers to relax using the same convergence criteria as used for the bulk structures. Similarly to bulk calculations, the k-point convergence was tested with respect to surface vacancy energy. For (2x2) Cu_2O 2x2x1 grid was used while for the others Γ only grid was employed.

2.8.2 Au/MgO/Ag surfaces

Calculations were performed utilizing GPAW with BEEF-vdW exchange-correlation functional. Using this functional yields to much longer computations in physical time compared to e.g. PBE. However, this way Van der Waals interactions, which may have crucial affect on the physisorption of molecules onto the studied surface, can be incorporated. An MgO/Ag surface was constructed consisting of three atomic layers of Ag(100) with two MgO(001) layers atop. An side-view example of the MgO/Ag slab model with Au adsorbates is pre-

Table 2.1. Size of unit cells and used parameters. In all calculations grid spacing was 0.20 Å except $Au_{stripe}(110)$ for which 0.16 Å was used.

Au island	Unit cell [MgO units]	k-points
Au_1	(2x2)	4x4x1
Au_2	(3x3)	3x3x1
Au_8	(4x4)	1x1x1
Au_{11}	(4x4)	1x1x1
Au_{12}	(4x4)	1x1x1
Au_{13}	(4x4)	1x1x1
Au_{14}	(4x4)	1x1x1
$Au_{stripe}(100)$	(4x2)	2x3x1
$Au_{stripe}(110)$	(5x3[45 °])	1x2x1

sented in Figure 2.2(j). Depending on the Au island size different unit cells, shown in Figures 2.2(a)-(g), were constructed. Table 2.1 reviews the unit cells and computational parameters used to model each of the studied Au islands. For instance, (2x2) unit cell is constructed of 2x2 MgO units in x -y plane with a lattice parameter of 4.166 Å. In these cases the cells are rectangular. Similar unit cell was also used to construct (100) stripe. However, to create (110) stripe a parallelogram cell was used with an angle 45°.

The two Ag layers at the bottom of the slab models were fixed at the initial positions of corresponding Ag bulk with a lattice constant of 4.18 Å, which was found by optimizing bulk fcc Ag. All other layers and adsorbates were allowed to relax until the residual force criterion of 0.05 eV/Å was fulfilled. Periodic boundary conditions were applied in the surface plane and not in the surface normal direction. Instead, in all slab models there was at least 5 Å vacuum under the bottom Ag layer and over any adsorbates. For (2x2) and (3x3) unit cells 4x4x1 and 2x2x1 Monkhorst-Pack k-point mesh were used while for the largest (4x4) only Γ-point was used. The calculations were done in a real-space grid with 0.2 Å spacing. Using these parameters the CO_2 adsorption energy was shown to be sufficiently converged between the different unit cells. In all calculations spin-polarization was included.

Adsorption of Au islands on supported MgO thin layer with varying size has been studied recently utilizing DFT calculations in [110, 111, 112, 113]. In this work adsorption of CO_2 and catalyzed formation of C_2O_4 species at these Au clusters was studied. While all Au islands and Au/adsorbate systems do not represent necessarily energetically the most favorable isomers, they can be

used to capture the general trends in adsorption properties of CO_2. Adsorption energy for any species X present on surface was calculated using equation

$$\Delta E_{\text{ads}} = E_{\text{X+surf}} - E_{\text{surf}} - E_{\text{X,vacuum}}, \tag{2.65}$$

where $E_{\text{X+surf}}$ is DFT total energy of the system containing adsorbate on surface, E_{surf} is slab energy without adsorbate and $E_{\text{X,vacuum}}$ is the X energy in vacuum. The barrier for C_2O_4 formation from two CO_2 precursors was investigated using constraint method, in which the distance of two C atoms was varied and fixed while allowing other atoms to relax.

In order to make comparison between the experimental IR absorbance spectra and DFT results, vibration analysis was performed utilizing `Vibrations` class implemented in ASE software. The method is based on the harmonic approximation and finite difference calculations to obtain the vibration eigenmodes of selected atoms in the system. In principle, energies for 6 displacements per atom ($\pm x, \pm y$ and $\pm z$) are calculated using 0.1 Å displacement. The more specific description of the method is given in [114]. Typically the absolute values of vibration energies obtained by DFT calculations differ from the experimental data and therefore scaling factors, which are characteristic to the system, may have to be used. Also, the changes in the energies with varying atomic masses are useful features to be studied, if experimental data using corresponding atom labeling is available. In this work ^{13}C and ^{18}O labeling for CO_2 was used in addition to the normal $^{12}C^{16}O_2$ molecule.

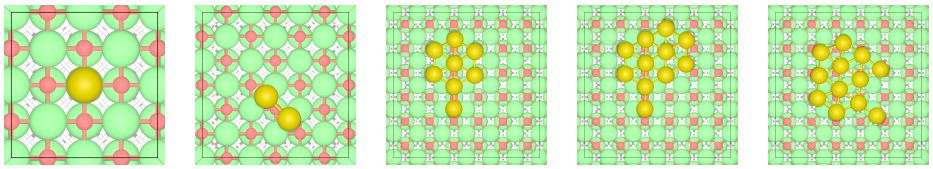

(a) Au_1 (b) Au_2 (c) Au_8 (d) Au_{11} (e) Au_{12}

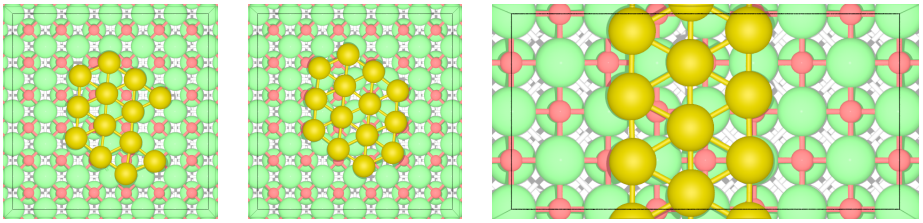

(f) Au_{13} (g) Au_{14} (h) $Au_{stripe}(100)$

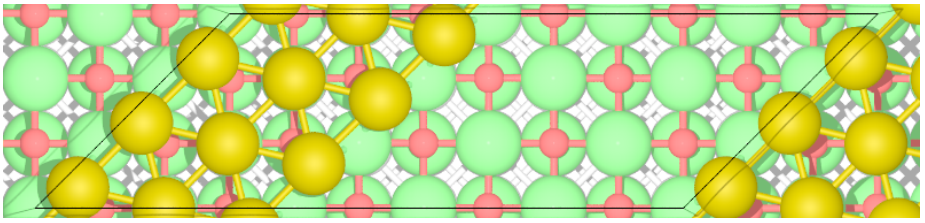

(i) $Au_{stripe}(110)$

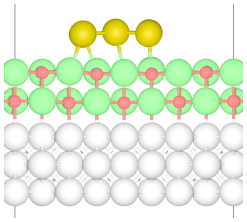

(j) Side view

Figure 2.2. *Examples of Au island models considered in this work. Images (**a**)-(**g**) represent separate Au islands consisting up to 14 atoms while (**h**) and (**i**) represent semi-infinite Au stripes along MgO lattice directions (100) and (110), respectively. Image (**j**) shows the whole slab model consisting of three Ag and two MgO molecular layers and Au adsorbates. White, yellow, red and green balls are Ag, Au, O and Mg atoms, respectively.*

3 Results and Discussion

3.1 Mn and Cu Oxides for CLC

3.1.1 Lattice Parameters, Electronic Structures and Formation Enthalpies

To validate the computational approach optimized lattice parameters, band gaps, formation enthalpies and oxidation enthalpies were first determined for all the studied oxide materials. Table 3.1 presents the computed lattice parameters and optimized magnetic structure together with experimental values and previously calculated parameters and the corresponding atomic structures displayed in Figure 2.1. In general, the results for both manganese and copper oxides are in good agreement with the experimental and previously calculated values. The largest deviation between the calculated and experimental parameters is found for Mn_2O_3 with the optimized lattice constant of 9.61 Å, while the corresponding experimental value is 9.42 Å. Even in this case the difference is just $\sim$2% and agrees with the earlier calculations. In studies PBE+U method has been found to overestimate manganese oxide cell volumes depending on the applied U parameter: larger U yields more overestimated equilibrium vol-

Table 3.1. Calculated magnetic moments, lattice constants and corresponding experimental values. The two magnetic moments for Mn_3O_4 correspond to Mn(II) and Mn(III) cations.

Metal oxide	Calc. lattice parameters [Å]	Ref. calc. parameters [Å]	Ref. exp. lattice parameters [Å]
α-Mn_2O_3	a : 9.61	a : 9.59[80]	a : 9.42[96]
Mn_3O_4	a : 5.90, c : 9.59	a : 5.78, c : 9.59[22]	a : 5.79, c : 9.56 [115]
CuO	a : 4.77, b : 3.46, c : 5.21, α : 99.6°	a : 4.68, b : 3.43, c : 5.14, α : 99.2°[116]	a : 4.65, b : 3.41, c : 5.11, α : 99.5°[117]
Cu_2O	a : 4.34	a : 4.31 [118]	a : 4.27[119]

Table 3.2. Calculated band gaps of the studied materials alongside with the reference values. The theoretical literature values refer to similar DFT calculations utilizing PBE functional. In cases where band gaps for majority and minority bands differ from each other, both gaps are shown. HM=Half metallic

Oxide	Calculated band gap [eV]	Literature value (PBE+U) [eV]	Literature value (experimental) [eV]	Calc. magn. moments [μ_b]
CuO	1.0	1.3[116] (U=7 eV)	1.2-1.9[121, 122, 123]	±0.63 (AFM)
Cu_2O	1.0	0.7 [118] (U=0 eV)	2-2.2 [124]	DM
Mn_2O_3	HM/4.6	HM/3.5 [80] (U=4 eV)	1.9-2.1 [125]	+4.11 (FM)
Mn_3O_4	0.7/4.4	0.6 [76] (U=4 eV)	2.1 [115]	+4.16/4.73 (FM)

ume [80]. This dependency has also been found for other oxides, e.g. ZrO_2 [34] and uranium oxides [120]. The U parameter was applied in order to correct the energies relating to oxidation and reduction, thus the deviation of these secondary parameters with this magnitude is acceptable.

The calculated band gaps are collected into Table 3.2. Electronic gaps for the both manganese oxides are represented well, when comparing to the experimental literature values if the gap is estimated as an average value between majority and minority spin. This can be done since it has been shown that the gap corresponding to paramagnetic phase (in which both experimental values have been obtained) can be assigned as the average of DFT+U calculated majority and minority-spin gaps for ferromagnetic state [126]. Since the magnetic structures used in the calculations do not correspond to paramagnetic room temperature magnetic phases, the band gaps are not directly comparable. The band gaps calculated here for manganese oxides are well comparable with the previous PBE+U studies, although the minority band gap for half-metal Mn_2O_3 is larger than the one presented by Franchini *et al.* [80]. The calculated magnetic moments are consistent with earlier PBE+U calculations [80] and experimental results [97].

The calculated band gaps of both copper oxides are slightly underestimated when compared to the experimental gaps. The experimental values range for CuO from 1.2 eV up to 1.9 eV while the result in this work falls into the lower limit of that range. Using significantly higher U parameter 7 eV the gap is increased 0.3 eV [116]. However, the calculated magnetic moment is perfectly in line with the experimental value of 0.68 μ_b [127] which, together with the equilibrium cell parameters, indicates that PBE+U level of approach is appropriate for describing both the crystal and the AFM magnetic structure

Table 3.3. The enthalpy of formation, corresponding literature values, the vacancy formation and oxygen diffusion energies for the studied CLC materials.

Metal oxide	ΔH_f [eV/atom]	Literature, DFT (experimental)[eV/atom]	Vacancy percentage [%]	E_{vac} [eV]	E_{diff} [eV]
Mn_2O_3	-10.06	-9.97[80](-9.939[129])	2.08	2.1	0.66
Mn_3O_4	-14.84	-14.337[80](-14.384[129])	6.25	3.82	0.52
			1.56	3.63	0.69
CuO	-1.61	-2.04[130](-1.63[129])	2.08	2.64	1.52
Cu_2O	-1.44	-1.24[116](-1.75[129])	6.25	2.44	1.56

of CuO. For Cu_2O the underestimation of band gap is more notable being $\sim$ 1 eV. This is a known feature of all GGA/LDA functionals even applying the U parameter [128]. However, the qualitative features of the DOS (not shown here) appear very similar when compared to e.g. previous DFT study [118].

The second column in Table 3.3 summarizes the calculated formation enthalpies (using Equation 2.63). In general, the calculated values agree reasonably with the corresponding experimental values presented in the third column of the table. Particularly, this holds for CuO, for which the theoretical value matches fortuitously the experimental one. For Cu_2O, the value computed in this study and the measured value differ slightly but compared to the previous computed value at the same level of theory PBE+U the value obtained here matches better with the experimental value.

Oxidation enthalpies of M_3O_4 and Cu_2O were calculated employing the following two reaction equations

$$\begin{aligned} 4Mn_3O_4 + O_2 &\rightarrow 6Mn_2O_3 \\ 2Cu_2O + O_2 &\rightarrow 4CuO \end{aligned} \tag{3.1}$$

Computed reaction enthalpies (per O_2 molecule) are -1.76 eV and -2.60 eV for Mn_3O_4 and Cu_2O eV, respectively, and they compare reasonably well with the measured values -2.01 eV and -2.73 eV [27] but are less negative than the measured enthalpies. In general, underestimation can, at least partly, be explained by the typical overestimation of the O_2 molecule binding energy in the GGA-level of theory [131]. Moreover, the experimental values were measured at 850 °C whereas DFT-computed values were obtained at 0 K. The oxidation enthalpy of Cu_2O were previously calculated with the GGA+U method by Wang *et al.*[76], who reported the enthalpy value of $\sim$-3.0 eV, which, however,

includes -1.36 eV correction to O_2 energy.

The different oxidation states of cations are evident from the Bader analysis. For Mn(III) and Mn(II) cations in Mn_3O_4 bulk the Bader analysis finds charges +1.74 e and +1.50 e, respectively. For Mn_2O_3 the charge for all cations is +1.78 e which can be therefore interpreted to correspond the formal oxidation state of +3.

3.1.2 Formation of oxygen vacancies and their migration in bulk

During a reduction, an oxygen carrier donates an oxygen atom to fuel in a CL process, therefore oxygen vacancy formation energy gives an estimate of the reducibility of a material. The more positive vacancy formation energy value corresponds lower reducibility. The second key property of an efficient oxygen carrier material is fast oxygen ion transport, which is addressed here by calculating a migration barrier in the bulk. In the following sections the reducibility and oxygen transport in all four oxides studied are addressed.

Creating a single oxygen vacancy induces structural changes in the neighboring cations. The removal of an neutral oxygen also leaves two electrons in the lattice, and the fate of these electrons is a key issue in a reduction process. Small relaxation has been found as an indication of an electron trapping in the vacancy e.g., in ZrO_2 [132] which is a similar reducible oxide as manganese and copper oxides. Again, the Bader method was applied to investigate the charge states of the nearest cations to the vacancy.

In all oxides there are essentially two possible types of oxygen migration paths into created vacancy. These types are labeled henceforth as edge paths (EP) and face paths (FP). EP goes through one edge of tetrahedron composed of four cations with one oxygen in the middle. Correspondingly, a pathway is labeled FP if it goes through one of the tetrahedron faces. In oxides EP pathways correspond typically the first nearest-neighbor (1NN) jumps, i.e. the oxygen nearest the vacancy jumps to the vacant site, and usually they have the lowest energy barrier. However, in the case of Cu_2O the 1NN pathway is FP which also has the lowest diffusion energy. Also with Mn_3O_4 it is demonstrated that also 2NN pathways may actually have the lowest migration barrier and hence all the possible routes for diffusion should be considered.

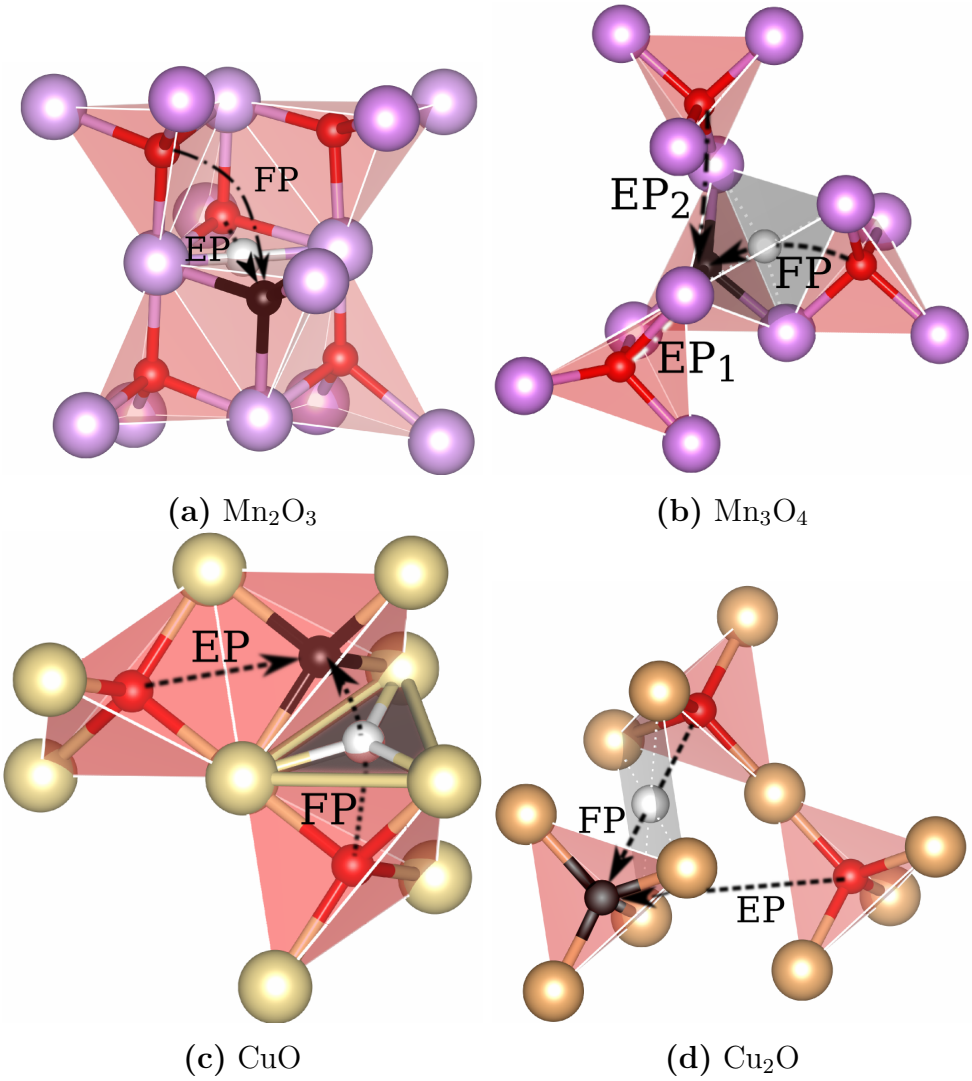

(a) Mn_2O_3 **(b)** Mn_3O_4

(c) CuO **(d)** Cu_2O

Figure 3.1. *Possible paths for oxygen migration in the bulk structures. Two types of diffusion paths are identified: edge paths (EP) and face paths (FP).*

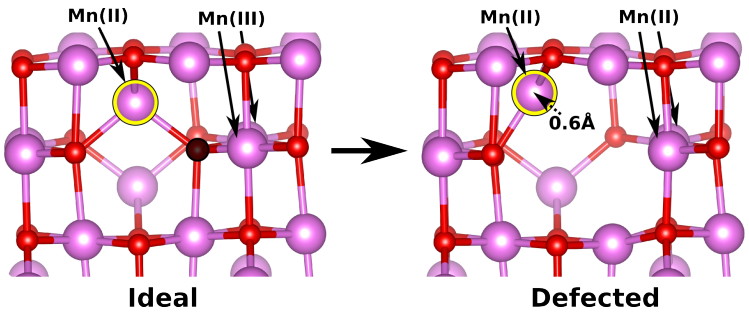

Figure 3.2. *The relaxation and change of oxidation states of cations around created oxygen vacancy. The black sphere is the oxygen atom which is removed upon creating a vacancy and purple atom encircled yellow is the 1NN Mn(II) atom in relative to the vacancy.*

Manganese oxides

To make an oxygen vacancy V_O, one neutral oxygen atom is simply removed from the bulk. Using equation 2.64, the computed vacancy formation energies E_{V_O} are 2.2 eV and 3.6 eV for Mn_2O_3 and for Mn_3O_4, respectively. For Mn_3O_4, the impact of vacancy concentration was explored further and E_{V_O} was also calculated at a higher vacancy concentration employing a smaller unit cell size. In this case, slightly higher vacancy formation energy of 3.8 eV was obtained. The higher vacancy energy for Mn_3O_4 compared to the relatively oxidized Mn_2O_3 and the fact that the vacancy formation energy increases with increasing concentration could indicate that the reducibility becomes more difficult as the material is reduced further. This in turn might be important for hindering Mn_3O_4 reduction to metallic manganese. On the other hand, it could also be linked to poor oxygen carrying capacity, which has been identified as a possible disadvantage of Mn-based oxygen carriers [13]. However, a comparison of computed vacancy formation energies with those of well-known reducible metal oxide bulks such as CeO_2 and TiO_2, which present vacancy formation energies around 4.6 eV [133] and 7 eV [134], indicates that both Mn oxides studied in this work can be classified as reducible oxides.

While tetrahedrally coordinated Mn^{+2} atom in Mn_3O_4 moves as much as 0.6 Å away from the vacancy (presented in Figure 3.2), the Mn^{+3} atoms in the both manganese oxides relax outwards at most ∼0.15 Å. All the other atoms remain approximately in their original positions. The structural relaxation stabilizes the oxygen deficient structure compared to the un-relaxed structure. Relaxation energy amounts to 0.5 eV for both Mn oxides, which is similar to the value reported in the literature for bulk ZrO_2 [135].

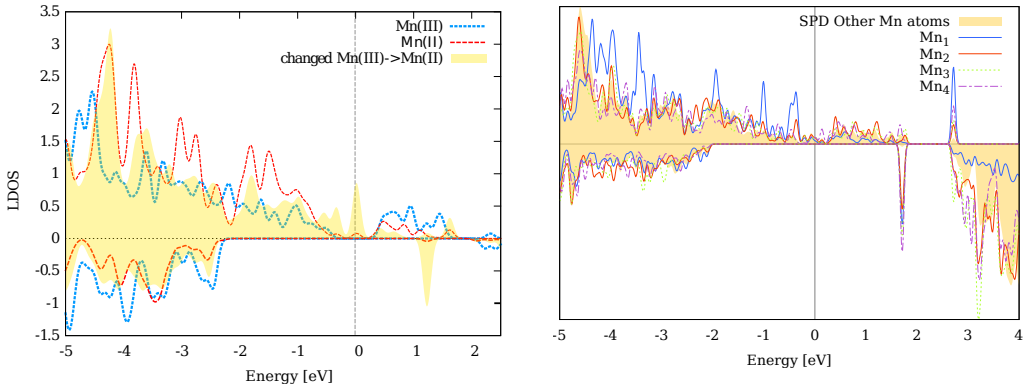

(a) Mn_3O_4 (b) Mn_2O_3

Figure 3.3. *Total LDOS plots of cations in single oxygen deficient manganese oxide bulks. (**a**) In Mn_3O_4 two Mn^{3+} reduce to Mn^{2+} which is supported by comparing the DOS of these atoms with Mn^{2+} before creating a vacancy. New states at the band gap are also appeared at 0 eV in the majority spin channel and 1.2 eV in the minority spins. (**b**) In Mn_2O_3 the +3 to +2 reduced Mn (Mn_1 in figure) shows distinct features compared to the other cations, like sharper peaks at -1 eV, -0.4 eV and more modest unoccupied states 2.6 eV and onwards in the minority spin channel (Mn_2 to Mn_4 are three other nearest-neighbor Mn atoms around vacancy and filled curve is DOS of all other cations). The nearest-neighbor Mn atoms share however the same peak at 1.7 eV in the minority states which is not seen in the other cations.*

In Mn_3O_4, two nearest Mn^{3+} cations gain 0.23 electrons upon creating a single oxygen vacancy compared to the initial state which can be interpreted as a change of a oxidation state from +3 to +2, while the oxidation state of the third Mn^{3+} and the only Mn^{2+} stay intact. The Mn^{2+} displays the largest displacement from the vacancy which can be associated to maintaining its oxidation state. The DOS plots provide further support for the Bader analysis. The +2 and +3 Mn cations display distinct features as shown in Figure 3.3(a) (red and blue lines respectively). In the oxygen deficient system, the LDOS plot of atoms, for which the Bader charge did not change, remains relatively same compared to that of the ideal bulk. The most significant changes are seen in the LDOS of the two nearest reducing Mn^{3+} cations (yellow area in the Figure) which express some features of Mn^{2+} DOS, especially peaks at -4.3 eV, -3.8 eV and -1.8 eV. The formation of single oxygen vacancy is also accompanied by new states at the band gap reducing the effective electronic energy gap for

majority and minority spin channel to 0 eV and 3.3 eV. Both the Bader and LDOS analysis therefore suggest that the two excess electrons of the removed oxygen in Mn_3O_4 bulk are mainly localized to the two nearest neighbor Mn^{3+} cations and reduce them to the +2 oxidation state, while the Mn^{2+} cation at the vicinity of the vacancy remains intact. This is not, however, surprising as Mn is not known to exits in oxidation state +1 in any stable oxide [129].

In the case of Mn_2O_3, the Bader method indicates that one of the nearest Mn atoms gains 0.26 electrons which is interpreted as reducing to the oxidation state +2, while the rest of the charge seems to spread to three other cations. This is also seen in DOS plots, presented in Figure 3.3(b). At the defected system for the reducing Mn atom a new LDOS peak at 1.7 eV is appeared in the minority spin channel, which also reduces the effective band gap to 3.7 eV. This peak is not seen in any other atoms and is consisted equally of *p*- and *d*-states. From the DOS is also evident that the most reduced Mn cation displays the most distinguishable features compared to the other cations, like sharper peaks at -1 eV and -0.4, red-shifted *p*-bands at -5 to -3 eV and more modest unoccupied states at 2.6 eV and upwards.

Next, the oxygen diffusion into a created vacancy is discussed. In Mn_3O_4, there exists three geometrically different oxygen ion migration channels as shown in Figure 3.1(a). Two of them are edge paths (EP_1 and EP_2), while the third channel is FP. The two EP channels differ in a number of edges they pass: along EP_1 the anion migrates through one edge shared by the neighboring tetrahedrals but along the EP_2 channel the ion goes through two edges. Along FP, at the transition state, the oxygen coordinates with four manganese atoms initially forming an empty tetrahedral site. In here EP_1, FP and EP_2 are 1NN, 2NN and 3NN paths, correspondingly.

The computed migration barriers for channels EP_1 and EP_2 are 1.41 eV and 1.94 eV, respectively. However, the barrier for the channel FP is energetically the most favorable being only 0.69 eV, which is significantly lower compared to the other two paths. The main reason for this is, in addition to four stabilizing NN Mn atoms at TS, that along this path the migrating oxygen minimizes the repulsive O-O interactions compared to other possible diffusion routes (see Table 3.4). At TS, the nearest oxygen atoms are $\sim$ 2.9 Å which is significantly further than in other diffusion path transition states (2.5-2.6 Å). The combination of these two factors can be seen as over 0.7 eV lower diffusion barrier compared to other two routes.

Also, the 0.5 eV difference between the two EP paths can be explained by

Table 3.4. NN bond lengths at transition states of FP, EP_1 and EP_2 oxygen migration paths in Mn_3O_4 alongside with the corresponding barriers. The numbers in the parenthesis indicate the oxidation states of Mn atoms.

Path	d(Mn-O) [Å]	d(O-O) [Å]	E_{diff} [eV]
FP	1.98 (+2), 2.07 (+2) 2.12 (+2), 2.66 (+3)	2.86, 3.04, 3.02, 2.96	0.69
EP_1	1.89 (+2 to +3), 1.90 (+2 to +3)	2.54, 2.55, 2.77, 2.77	1.41
EP_2	1.92 (+2), 2 x 2.40 (+3)	2.62, 2.62	1.94

the transition state geometries. At EP_1 TS the migrating oxygen has two NN Mn atoms with bond lengths of 1.9 Å. These two Mn atoms are at an oxidation state which is in between +2 and +3, according to the Bader analysis. At the TS of EP_2 the nearest Mn, with distance 1.9 Å, is at +2 state. There are also two NN +3 cations but the distance to these atoms is relatively large, 2.4 Å. These cations are forced away from the migrating oxygen by two NN O atoms, presented in Figure 3.4. Therefore the repulsing O-O ion Coulomb interactions outweigh the attractive Mn-O interactions in this case. Hence the stronger Mn-O bonds in the EP_1 path compared to the EP_2 transition state may explain the favorability of the former migration path.

Two feasible oxygen migration channels are considered for Mn_2O_3, one EP and FP displayed in Figure 3.1(b). EP presents a 1NN jump while FP is a 2NN pathway. In principle also a 3NN pathway (edge→empty tetrahedral site→edge) could be feasible, but in the pre-screening of this pathway demonstrates that the migration barrier is higher than 2.5 eV and therefore the channel was excluded from the further studies. The computed barriers for the EP and the FP channels are 0.66 eV and 0.95 eV, respectively. Like in the case of Mn_3O_4, the relative barriers can be explained by transition state geometries. Migration along the EP channel maximizes the distances between the moving oxygen and the nearest neighbor anions. The FP channel is similar to the FP in Mn_3O_4. However, at the transition state, the migrating oxygen lies on the same plane with the three nearest manganese cations, while in Mn_3O_4 bulk the transition state is tetragonally coordinated. The difference is a result from additional oxygen atoms surrounding the diffusion path in Mn_2O_3. Comparison of EP channels shows that in Mn_3O_4 the barrier is over twice that of Mn_2O_3. The large difference in these energies can be explained by Mn-Mn distances at the edges: in Mn_2O_3 the distance is 3.40 Å while it is 3.18 Å in Mn_3O_4 providing

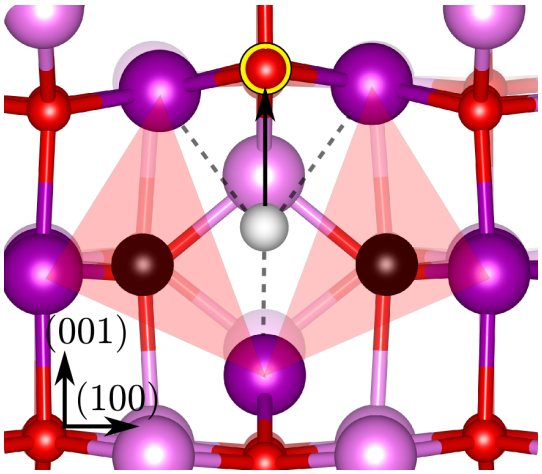

Figure 3.4. *EP_2 diffusion route TS coordination in Mn_3O_4 bulk. The black spheres indicate the vacant oxygen sites. The two oxygen atoms marked with yellow border (only one shown in Figure due to overlap) are pushed further away from the TS oxygen atom (white sphere) by 0.25 Å indicating strong repulsion between these atoms. Due to this interaction EP_2 is unfavored compared to other possible routes.*

less space to move for diffusing oxygen.

Copper oxides

In CuO and Cu_2O, the formal oxidation states of copper atoms are +2 and +1, respectively. The corresponding computed Bader charges are +1.12e and +0.51e in ideal bulks which can be used as a comparison for the reduction analysis. The value for Cu_2O agrees well with the value of 0.53e reported in a recent PBE study [118]. The computed values match also with an experimental study [136] where the charges were found to range from +0.84e to +0.57e on Cu atom and -1.68e to -1.14e on O atom.

The relaxation of an oxygen vacancy defected system is totally different compared to the manganese oxides. In Cu_2O the copper atoms around a vacancy are strongly moved by $\sim$ 0.33 Å towards the vacancy upon relaxation bringing also the neighboring oxygen atoms closer by 0.17 Å. The movements of all the next shells of atoms surrounding the vacancy are minor. This kind of behavior is typical for ionic oxides [137]. The Cu-Cu distance of 3.07 Å in stoichiometric bulk is reduced around the oxygen vacancy to 2.54 Å, which is close to the corresponding table value of 2.56 Å in Cu bulk [138]. Upon relaxation the structure, the energy is reduced by 1.2 eV which is over twofold compared

to corresponding value obtained for the manganese oxide bulks. This may be due to the unique structural characteristics, especially the unusual linear coordination of O-Cu-O chain. Breaking this chain results in total change in the local structure and pure Cu phase is formed.

In CuO bulk the relaxation of atoms around an anion vacancy is different compared to Cu_2O. The NN copper atoms stay relatively firmly at the initial positions and move towards the vacancy only ~ 0.03 Å while the most notable relaxation of 0.09 Å (towards the vacancy) is seen in NN oxygen atoms. For other atoms the relaxation is smaller than 0.05 Å. After an oxygen vacancy is introduced, the Bader charges indicate that only the NN cations around the vacancy are reduced. Each of the four Cu(II) atoms are reduced by $0.25e$-$0.30e$ while the charge of other atoms in the bulk remains relatively unchanged indicating that the two leftover electrons are fully localized to the copper atoms around the vacancy. Upon relaxation the total energy is reduced by $\sim$0.5 eV which happens to be in line with both manganese oxide bulks but significantly lower than for Cu_2O.

The computed vacancy formation energy 3.6 eV in bulk CuO is substantially higher compared to the corresponding value 2.4 eV in Cu_2O bulk which indicates that after the first step, CuO $\Rightarrow$ Cu_2O, the reduction from Cu_2O to Cu is more rapid. In fact, recent time-resolved XRD studies support this deduction suggesting that Cu^{1+} oxide is not a stable intermediate in reduction of CuO [139, 140]. Instead, the reduction is rather occurring via a one-step process CuO $\Rightarrow$ Cu. .

The changes induced to the densities of state in both copper oxides are seen in Figure 3.5. In Cu_2O the HOMO *p*- and *d*-states are pushed lower in energy by ~ 0.2 eV when oxygen is terminated from the structure (Figure 3.5(a)). Also new LUMO states are seen. Therefore the band gap stays essentially the same at 0.85 eV. The new LUMO states are consisted of mainly *p*-states of metal atoms (Fig. 3.5(b)). In CuO, however, band gap in oxygen lacking system is 0.5 eV being only half of the original gap. New states appearing to the gap area are originated from the NN metal atom *d*- and *p*-states (Figure 3.5(d)). Also the *d*-band center of NN copper atoms is red-shifted strongly.

The diffusion pathways in Cu_2O and CuO bulk oxides are presented in Figures 3.1(c) and (d), respectively. In both materials there are two noteworthy oxygen ion diffusion paths into created vacancy site: one FP and one EP. However, there are prominent differences comparing these paths between the two materials. Firstly, EP in Cu_2O has to go through two edges (see Figure

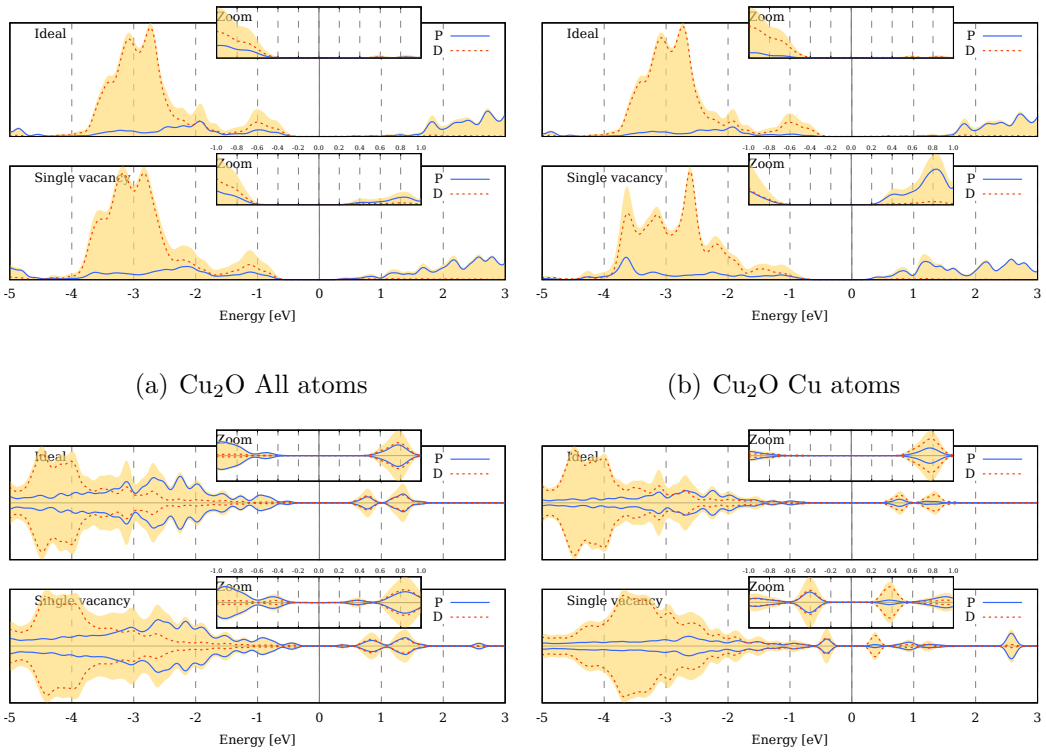

(a) Cu_2O All atoms

(b) Cu_2O Cu atoms

(c) CuO All atoms

(d) CuO Cu atoms

Figure 3.5. *The changes in PDOS induced by oxygen vacancy in copper oxides. (a) and (b): All atom and NN (in relative to the oxygen vacancy V_O) cations only DOS for Cu_2O and correspondingly (c) and (d) for CuO. Note the different scales of the overview and zoomed plots presenting the energies near Fermi level more accurately. The upper plot in each figure is for ideal bulk while the lower plot is for V_O defected system. Spin-up (down) states are plotted into the positive (negative) y-axis for CuO.*

3.1(d)) while in CuO only one edge is penetrated. Secondly, comparing the FPs most distinct difference is the geometry of the TS coordination of the migrating oxygen ion. In Cu_2O the oxygen coordinates with planar tetragonal geometry (grey plane in Figure 3.1(c)) with four adjacent copper cations while in CuO the transition state coordination geometry is rather trigonal. EP in CuO corresponds to the 1NN diffusion while FP is the 2NN pathway and in Cu_2O vice versa.

In both materials FP is preferred over EP. The calculated FP barriers for Cu_2O and CuO are 1.56 eV and 1.52 eV, respectively. The barriers are surprisingly similar for both materials given the different geometries of the paths. EP in Cu_2O yields 2.1 eV barrier which compares well to the EP barrier in CuO

(2.0 eV). Again, in the case of CuO, the 2NN oxygen hop is preferred over the 1NN pathway mainly due to clearly more open space for the migration. Also, there are no other oxygen atoms at the immediate vicinity of the TS. The same arguments can be applied also for Cu_2O.

Overall, it can be concluded taking into account also manganese oxides that for the studied oxide bulks the differences in the diffusion barriers are minor when one compares the reduced and oxidized form with each other and the most significant differences rise at the vacancy formation energies. The difference between manganese and copper oxides arises when we are comparing the relative vacancy formation energies between the reduced and the oxidized form: in manganese oxide the energy to form an oxygen vacancy increases as the oxide reduces while in copper oxides the affect is vice versa. This may indicate that copper oxide has tendency to form pure metallic phase upon the reduction while manganese oxide remains as an oxide. As explained above, reducing into pure metal is disadvantageous property of OC as it may lead to unwanted catalytic reactions and decrease of the expected OC life time in CLC conditions.

3.1.3 Thermodynamics and kinetics at the surface

In this section the focus is shifted from the bulk materials to the corresponding surfaces. Since most of the reactions in CLC process happen at the surfaces of OC particles, it is important to study also the thermodynamics at the vicinity of the surfaces to address the reactivity of the materials. The relaxation effects of the ideal surfaces, energies of single point oxygen vacancies and the kinetics at the vicinity of the surfaces keeping the vacancy separation distances between each material as equivalent as possible will be discussed. All surfaces show at least two differently coordinated oxygen atoms for all of which the corresponding vacancy formation energy has been calculated. The vacancies were made to the top layer of the surfaces as well as the second layer subsurface sites and diffusion barriers between these two states were computed. In these calculations the most stable surface oxygen vacancy was chosen as the initial state and possible diffusion paths between the two states were identified and calculated.

The relaxed surface structures are presented in Figures 3.6 and 3.7. The corresponding computed surface free energies alongside with the oxygen vacancy formation energies and corresponding diffusion barriers for each structure are presented in Table 3.5. In the figures and discussion the surface oxygen atoms

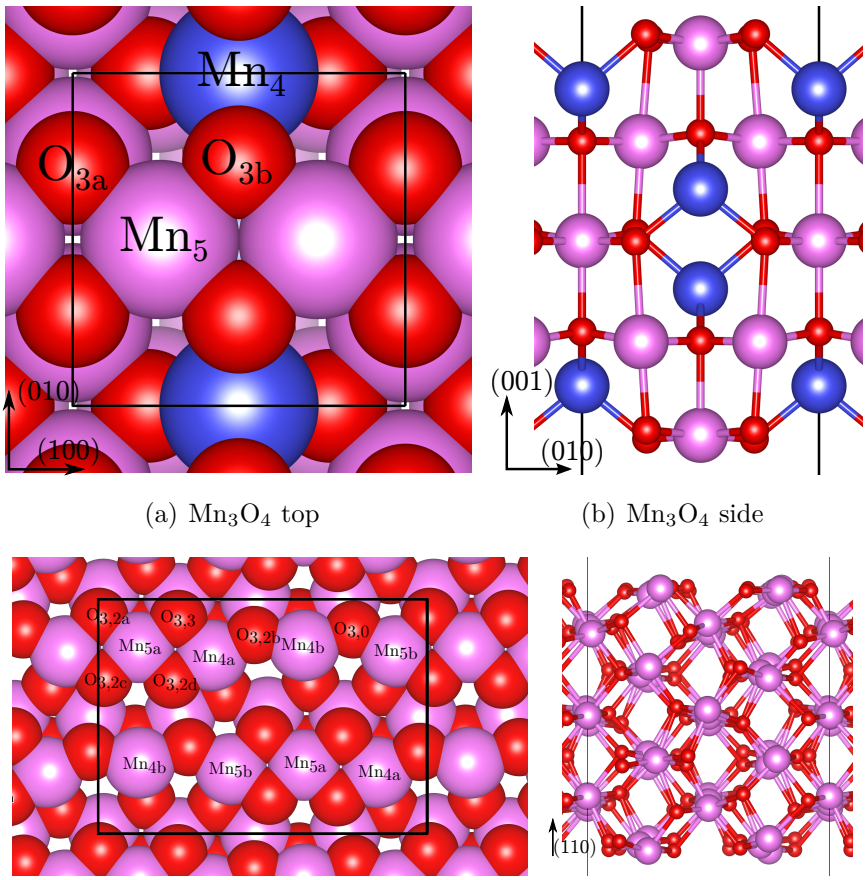

(a) Mn_3O_4 top (b) Mn_3O_4 side

(c) Mn_2O_3 top (d) Mn_2O_3 top

Figure 3.6. *Smallest possible surface slab cells of $Mn_3O_4(001)$ ((a) and (b)) and $Mn_2O_3(110)$ ((c) and (d)). Manganese atoms in tetragonal (octahedral) sites are colored blue (purple) and oxygen atoms are red. Different kind of manganese and oxygen atoms at the topmost layer are labeled.*

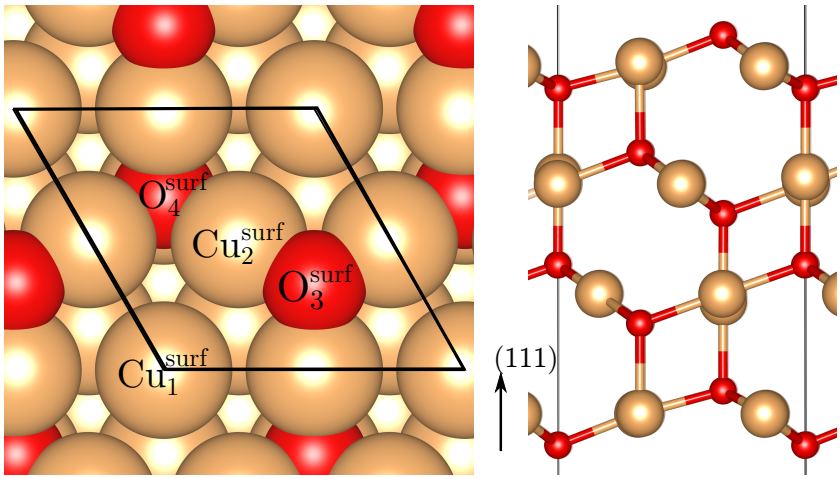

(a) CU_2O top (b) Cu_2O side

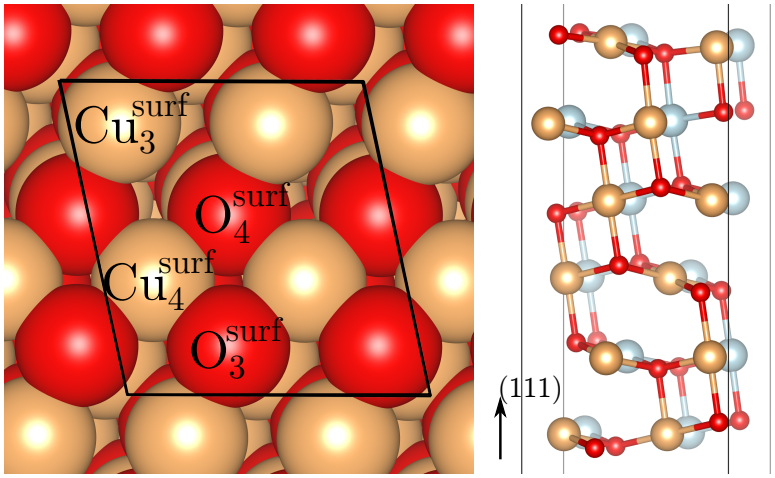

(c) CuO top (d) CuO side

Figure 3.7. *Smallest possible surface slab cells of $Cu_2O(111)$ ((a) and (b)) and CuO(111) ((c) and (d)). The spin up (down) cations in the antiferromagnetic structure of CuO are colored brown (light blue)*

Table 3.5. Summarized results for surface structures. If several differently coordinated oxygen atoms were present, the shown vacancy formation energies are the lowest energy surface vacancies.

Surface	γ [meV/Å^2]	Vacancy concentration [1/nm^2]	Vacancy separation [Å]	E_{vac} [eV]	E_{diff} [eV]
Mn_2O_3(110)	67.3	0.8	x:13.6, y:9.6	1.45	1.1
Mn_3O_4(001)	65.5	0.7	11.8	1.94	1.2
Mn(100)	162.9				
Mn(111)	150.0				
CuO(111)	39.6	2.8	x:5.9, y: 6.1	2.50	
		0.7	x:11.8, y: 12.2	2.26	1.0
Cu_2O(111)	42.2	3.1	6.1	2.57	1.6
		0.8	12.2	1.78	1.6
Cu(111)	67.7				

are labeled as O_m^{surf} in which m is the number of metal atoms to which the oxygen bounds to. Additionally if there are more than one atom with the same coordination number m, second index o is introduced indicating the number of oxygen atoms at nearest neighboring tetragonal sites. Metal cations are numbered using the same scheme Me_o^{surf}.

Manganese oxide surfaces

Mn_3O_4(001) At the Mn_3O_4(001) surface (Figure 3.6(a)) there are two different kinds of manganese and oxygen atoms. Manganese cations coordinate either with four or five surrounding anions. Atom Mn_5^{surf} is bounded to four surface and one subsurface oxygen atoms while Mn_4^{surf} atom coordinates with two surface and two subsurface oxygen atoms. There are two different surface oxygen atoms labeled as O_{3a}^{surf} and O_{3b}^{surf} which both coordinate with three manganese atoms: O_{3a}^{surf} with two Mn_5^{surf} atoms and one subsurface manganese while O_{3b}^{surf} with two Mn_5^{surf} atoms and one Mn_4^{surf} atom.

The Bader determined charges for atoms Mn_5^{surf} and Mn_4^{surf} are $+1.70e$ and $+1.54e$, respectively, which are relatively close to the corresponding bulk values ($+1.74e$ and $+1.50e$). At the second layer the charges are already very close to the bulk values. Surface oxygen atoms O_{3a}^{surf} and O_{3b}^{surf} express the charge of -1.17e and -1.11e, respectively. Summing up the positive and negative charges of Mn and O shows that first two formula unit layers express total charges of 1.5e and 0.3e while corresponding values for third and fourth layer are -0.3e and -1.5e. Therefore Mn_3O_4(001) surface is polarized according to Bader analysis.

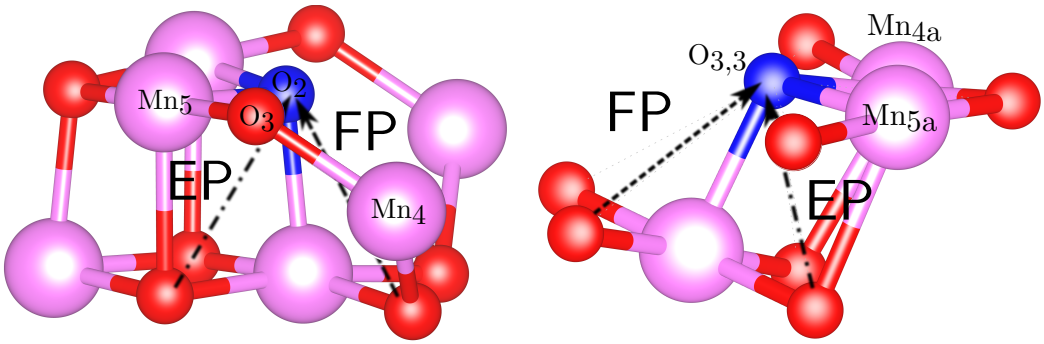

(a) Mn_3O_4 (b) Mn_2O_3

Figure 3.8. *Possible oxygen diffusion paths from the second atomic layer onto a vacancy at the surface layer of (a) $Mn_3O_4(001)$ and (b) $Mn_2O_3(110)$ surfaces.*

O_{3a}^{surf} bonds with three Mn(III) atom while O_{3b}^{surf} coordinates with two Mn(III) and one Mn(II) atoms. This is reflected in the vacancy formation energies for these two surface oxygen atoms, computed to be 1.94 eV and 2.73 eV, respectively. Comparing these values to bulk (3.6-3.8 eV), the vacancy formation energy is therefore reduced by even $\sim$ 50 % at the surface. Removing O_{3a}^{surf} reduces two surface Mn_5^{surf} atoms by $0.14e$, Mn_4^{surf} atom by $0.07e$, nearest neighbor oxygen atom is gained $0.12e$ and rest of the charge is divided rather uniformly between other surface atoms. Upon removing O_{3b}^{surf} two NN surface Mn(III) reduce by $0.19e$ while NN Mn(II) atom is reduced further by $0.11e$.

There are two possible pathways, FP and EP, (Figure 3.8(a)) for diffusion from the subsurface layer into the surface oxygen vacancy O_{3a}^{surf}. The pathways correspond to the bulk FP with similar interstitial tetragonal binding site along the diffusion path and the bulk EP_1, respectively. The diffusion barriers for these pathways are 1.2 eV and 1.8 eV, respectively, presenting $\sim$ 0.4 eV higher values compared to the bulk (0.7 eV and 1.4 eV). However, the diffusion barriers are relatively low compared to the vacancy formation energy when the typical underestimation due to the overestimation of O_2 binding energy is taken into account, which indicates that the diffusion is not the rate-determining step in the reduction process.

The 0.4 eV difference of bulk and surface diffusion for FP can be reasoned by the transition state geometry. In bulk the migrating oxygen coordinates with four cations at the TS while at the surface one of these corresponding manganese atoms is removed in the surface cleavage. For EP the higher barrier can be explained by the relaxation of the first atomic layer. Mn_5^{surf} atoms withdraw

0.2 Å towards the second atomic layer reducing the Mn-Mn distance at the tetragon edge by 0.3 Å and therefore leaving less space for the oxygen atom to penetrate the edge.

Mn_2O_3(110) In Mn_2O_3(110) surface there are four different kinds of Mn atoms and three types of oxygen atoms (Fig. 3.6(c)). Mn_{5a}^{surf} and Mn_{5b}^{surf} coordinate with five oxygen atoms (Mn_{5a}^{surf}: 4 oxygen atoms in the same plane and one in the second layer, Mn_{5b}^{surf}: three O atoms in the same plane and two in the second layer) while Mn atoms in sites Mn_{4a}^{surf} and Mn_{4b}^{surf} coordinate with four oxygen atoms (Mn_{4a}^{surf}: three O atoms in the same plane and one in the second layer, Mn_{4b}^{surf}: two O atoms in the same plane and two in the second layer). All of the surface oxygen atoms coordinate with total of three Mn atoms, two at the topmost layer and one at the second atomic layer, with very similar average bond lengths from 1.97 Å (site $O_{3,2d}^{surf}$) to 2.01 Å (site $O_{3,2b}^{surf}$).

All surface oxygen atoms coordinate with three cations. Categorizing these atoms in respect to the Mn atoms to which they are bounding to, half of the anions can be eliminated from further analysis within the unit cell. From these atoms three noteworthy different geometries of surface oxygen atoms can be identified when nearest neighboring other oxygen atoms are considered, labeled as $O_{3,0}^{surf}$, $O_{3,2}^{surf}$ and $O_{3,3}^{surf}$. The second index describes the number of other oxygen atoms within an arbitrary cut-off radius of 2.75 Å at the ideal relaxed surface. There are four $O_{3,2}^{surf}$ atoms whereas $O_{3,0}^{surf}$ and $O_{3,3}^{surf}$ are unique amongst the six surface oxygen atoms in the consideration. Vacancy formation energies for all these atoms were calculated and the results are: $E_{vac,3,3} = 1.4$ eV $< E_{vac,3,2b} = 1.8$ eV $< E_{vac,3,2d} = 1.9$ eV $< E_{vac,3,2c} = 2.0$ eV $< E_{vac,3,2d} = 2.1$ eV $< E_{vac,3,0} = 2.4$ eV. This way clear negative correlation between the number of nearest neighboring oxygen atoms and the vacancy formation energy can be seen. This is expected because of the Coulomb repulsions between negatively charged oxygen ions.

The Bader charge of Mn_{4b}^{surf} ($+1.49e$) is significantly different compared to the other surface cations, which express $+1.7e$ charge. Therefore Mn_{4b}^{surf} seems to be at +2 oxidation state while others are at state +3. The surface oxygen charges are from -1.08e to -1.19e. The $O_{3,3}^{surf}$ oxygen with the lowest vacancy formation energy is also characterized with the lowest charge while $O_{3,0}^{surf}$ with the highest vacancy energy has the charge at the higher end of the range, -1.18e. The surface is polarized as the sum of the charges for the first and second atomic layers are -0.42e +0.45e, respectively. The layers at the middle

of the slab model, possess bulk-like Bader charges and are therefore neutral in respect to the Bader charges.

At the oxygen deficient surface the excess electrons are localized at the vicinity of the vacancy. In the case of $O_{3,3}^{surf}$ vacancy the most reduced atoms are Mn_{5a}^{surf}, Mn_{4a}^{surf} and manganese atom at the second atomic layer initially bound to the removed oxygen atom. The magnitude of reduction respectively for these atoms are $0.05e$, $0.16e$ and $0.22e$. Overall, the excess charge tends to be localized at the second and third atomic layer which is evident from the computed total charges for the layers. Total of $0.6e$ is transferred from the first layer to the second and third formula unit layers.

Diffusion from the second layer into the most stable surface oxygen vacancy, $O_{3,3}^{surf}$, was studied. Because of the complexity of the structure, in this case also diffusion into the least favorable surface oxygen vacancy $O_{3,0}^{surf}$ was considered for reference. There are two possible diffusion pathways into $O_{3,3}^{surf}$, one FP and EP, shown in Figure 3.8. Barriers are 1.1 eV and 1.5 eV for pathways FP and EP, respectively. Here the EP is similar to the EP pathway in bulk Mn_2O_3 which was found the most favorable. Respectively FP is equivalent to the corresponding FP in bulk. Looking at the barriers, counter-intuitively the order of the barrier heights is opposite at the surface compared to the bulk. Increased barrier height of the pathway through the edge of tetragon can be explained by decreased space in between two manganese atoms forming the edge. At the relaxed surface the Mn-Mn distance is reduced $\sim 3.5\%$ compared to bulk. On the other hand, diffusion barrier along path FP, is very similar in the bulk (1.0 eV) and at the surface (1.1 eV).

The calculated vacancy formation energies of two second surface layer oxygen vacancies are 1.71 eV for EP and 1.93 eV for FP which are higher compared to the vacancy formation energy of 1.45 eV for $O_{3,3}^{surf}$. Therefore, in this case the surface vacancy is preferred over the subsurface vacancy, i.e. the transport of oxygen from the lower layers of the surface onto the surface may not be favorable. The relative stability of surface and subsurface oxygen vacancies is contrary to some other DFT studies for metal oxide surfaces [141, 116, 142]. However, compared to the other, more unstable, surface vacancies the calculated second layer oxygen defect formation energies are mainly lower. The relative stability of surface and subsurface vacancies is not therefore unambiguous for $Mn_2O_3(110)$ surface because of the complex structure.

For comparison, the diffusion barrier into the least stable surface oxygen vacancy, $O_{3,0}^{surf}$ is only 0.3 eV. The diffusion pathway corresponds to the FP

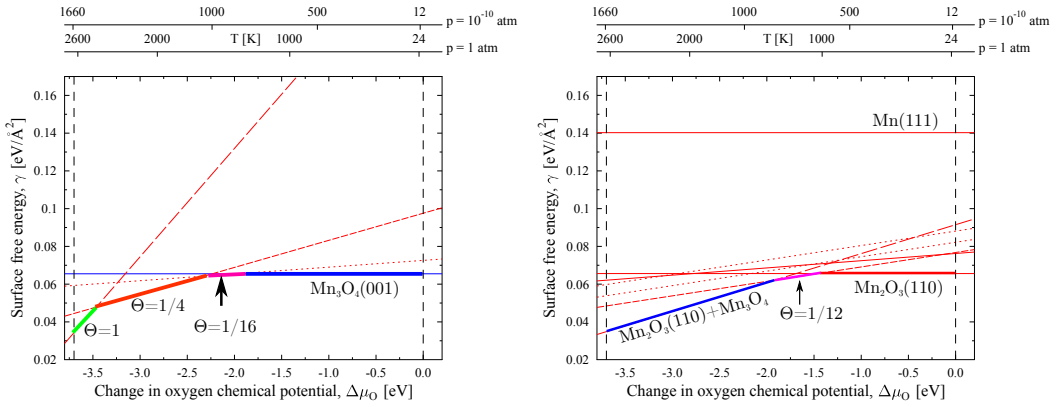

(a) Mn_3O_4 (b) Mn_2O_3

Figure 3.9. *The surface free energies of ideal and oxygen deficient most stable manganese oxide surfaces as the function of chemical potential of oxygen.* Θ *is the coverage of the surface defect.*

migration path in the bulk Mn_2O_3. The vacancy formation energy for the subsurface oxygen in this case is 1.9 eV which is very close to the other vacancies at the second layer and significantly lower than vacancy formation energy for $O^{surf}_{3,0}$, 2.4 eV. Compared to the corresponding value for bulk vacancy, 2.1 eV, the formation energy is still lower. The relative stability of the subsurface and surface vacancy at $O^{surf}_{3,0}$ explains the relatively low diffusion barrier for this pathway. The results indicate that the oxygen diffusion pathway from the bulk phase onto the surface may not be straightforward and may involve additional diffusion steps between first layer oxygen sites. However, the calculated values for the vacancy formation energies and diffusion barriers can give insight to the reactivity of the $Mn_2O_3(110)$ surface.

Comparing the vacancy formation energies and diffusion barriers at the vicinity of $Mn_2O_3(110)$ and $Mn_3O_4(001)$ surfaces a trend for reducing oxygen transport and release capabilities upon the reduction of manganese oxide can be established which is convergent with the computational results presented for the bulk structures. To get more insight and understanding about the influence of temperature and pressure to the reduction reaction between these two materials the theory of *ab initio* atomistic thermodynamics was employed.

Atomistic thermodynamics The theory of atomistic thermodynamics was used to predict the oxygen vacancy stabilities under different CLC conditions. The surface free energy γ was calculated for different oxygen vacancy coverages as a function of the oxygen chemical potential. The results for Mn

oxides in Figure 3.9(a) and 3.9(b) indicate that Mn_2O_3 surface is capable to release oxygen very rapidly at relatively low temperatures of 600-1000 K depending on the oxygen partial pressure. At this temperature a single oxygen vacancy becomes more stable than the ideal surface. Surface structure in which vacancies are present both at the surface and subsurface site becomes more stable by increasing the temperature $\sim$ 100 K representing a thin layer of similar stoichiometry than Mn_3O_4 oxide on $Mn_2O_3(110)$ surface. For the two oxygen vacancy model $O_{3,3}^{surf}$ and oxygen atom furthest away at the second layer were removed. This model may not present the most stable two vacancy system of $Mn_2O_3(110)$ surface but it sets the upper limit for the true lowest energy.

To study the reducing further, a clean $Mn_3O_4(001)$ surface was examined. A Single O vacancy with the coverage $\Theta = \frac{1}{16}$, i.e. 1 of every 16 surface O atoms removed, becomes more stable than the ideal stoichiometric surface at temperatures ranging from 800 to 1100 K. Coverage of $\Theta = \frac{1}{4}$ is preferred at temperatures from 1000 K to 1500 K. $Mn_3O_4(001)$ surface with all the surface oxygen atoms removed is achieved only in very high temperatures of $\sim$1500-2500 K. Clean metal surface is therefore unlikely to form in CLC conditions in which the temperature is typically below 1500 K. To study this also other manganese oxides with lower oxidation state, like MnO should be considered with more detail. The conclusions are however convergent with the conclusions drawn for bulk materials. The calculations suggest that oxidized manganese oxide Mn_2O_3 has rather rapid reduction rate due to its low oxygen vacancy formation energies and oxygen diffusion barriers, which is an essential property for OC materials. However, according to the calculations, manganese oxide does not have tendency to reduce into pure metal phase which is also a good property for an OC material.

Copper oxide surfaces

$Cu_2O(111)$ $Cu_2O(111)$ surface (Figure 3.7(a)) displays two differently coordinated copper and oxygen atoms. Oxygen atoms O_3^{surf} coordinate with three surface Cu_2^{surf} atoms and are the most exposed atoms at the surface. O_4^{surf} coordinates in addition to three surface copper atoms with one subsurface Cu. Cu_1^{surf} shares a bond with only one subsurface oxygen (not shown in the figure) with a bond length of 1.94 Å while Cu_2^{surf} atoms bond with two oxygen atoms at the surface layer. Cu_2^{surf} bond lengths to two neighbor oxygen atoms are not perfectly symmetric since Cu_2^{surf}-O_3^{surf} bond length is 1.85 Å and Cu_2^{surf}-O_4^{surf} bond is 1.89 Å which is the same as in bulk. The linear coordination of O-Cu-

O chains of bulk Cu_2O is broken at the surface as the relaxed O_4^{surf}-Cu_2^{surf}-O_3^{surf} angle is 174.3°. This is a result of slight intercalation of O_3^{surf} atom into the surface.

The Bader analysis reveals that at the first layer Cu_1^{surf} is the most reduced cation expressing $+0.39e$ total charge, while Cu_2^{surf} has a bulk-like charge of $+0.54e$. This is in line with the relative coordination numbers. Also all sub-surface cations are bulk-like in respect to the Bader charges. For O_3^{surf} the calculated charge is -0.99e and for O_4^{surf} -1.05e.

A single V_O in 2x2 $Cu_2O(111)$ corresponds to $\Theta = \frac{1}{8}$ defect coverage. Despite the different coordination, the vacancy formation energies for both surface oxygens show fairly similar values being 1.8 eV for O_4^{surf} and 1.9 eV for O_3^{surf}. Compared to the bulk the vacancy formation energy is reduced by ∼0.5 eV. However, according to the analysis the second layer oxygen vacancy O^{sub} is the most stable with a formation energy of 1.3 eV which is also significantly lower than the bulk vacancy formation energy 2.4 eV. Therefore the anions are driven towards the surface favoring the reduction process.

According to the Bader analysis, in the case of both surface anion vacancies, the excess electrons left by the removed oxygen atom are localized to surrounding copper atom by 0.25-0.35e. The copper atoms are left with +0.20 to +0.25 charge. Oxygen vacancy induces also strong lateral relaxation of surface atoms, illustrated in Figure 3.10(a). Similar to bulk Cu_2O, neighboring Cu_2^{surf} atoms are strongly attracted by the vacant site. The Cu-Cu distances around the vacancy are 2.44-2.51 Å which can be compared to the corresponding value 2.54 Å for the bulk. The Bader charges and the Cu-Cu distances indicate that the defected system has a tendency to form local phase which resembles pure Cu(111) surface. The bond length between the reduced Cu_2^{surf} and the nearest O_4^{surf} atom is 1.93 Å which is the same as Cu_1^{surf}-O bond at ideal surface. LDOS plots of reduced Cu_2^{surf} atoms and Cu_1^{surf} atoms show strikingly similar features, see Figure 3.10(b), especially the unique peaks at -2.3 eV and -3.5 eV.

For oxygen diffusion at the vicinity of $Cu_2O(111)$ there are only one viable pathway for both O_4^{surf} and O_3^{surf} surface vacancies, presented in Figures 3.11(a) and 3.11(b), both of which were analyzed as the vacancy formation energies of both surface oxygen atoms were similar in magnitude. Choosing O_3^{surf} defected system as the initial state of the diffusion process the only proper pathway from underneath the surface to the vacancy goes straight along (111) direction (see Figure 3.11(a)). This pathway is equivalent to FP in bulk Cu_2O which was found energetically most favorable. The calculations express a barrier for

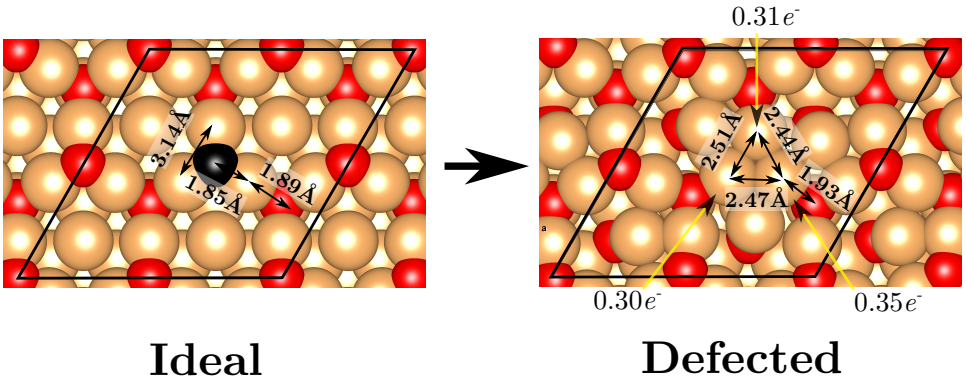

(a) Cu_2O top

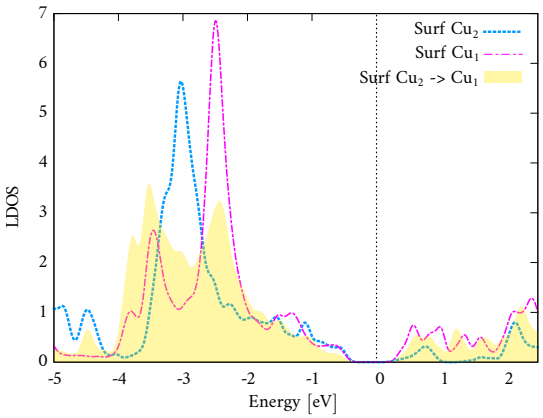

(b) LDOS

Figure 3.10. *(a) The relaxation of surface atoms at CuO(111) surface around V_{O_3} and (b) corresponding induced changes in the LDOS of Cu atoms around vacancy.*

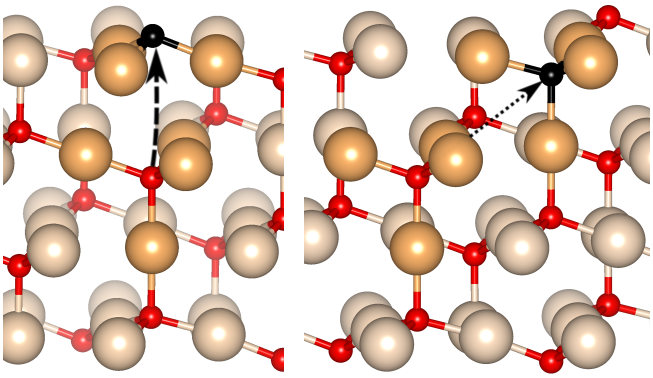

(a) V_{O_3} diffusion (b) V_{O_4} diffusion

Figure 3.11. *Viable diffusion paths at $Cu_2O(111)$ surface from the second atomic layer onto the first layer defected with vacancy (a) V_{O_3} and (b) V_{O_4}.*

surface FP diffusion 1.6 eV which is, within DFT related errors, the same as the barrier for FP in bulk.

For diffusion into surface O_4^{surf} vacancy the diffusion pathway goes directly through the edge of two Cu_4O tetragons via empty tetragonal binding site, similar to pathway EP in bulk Cu_2O which was found energetically unfavorable compared to the path FP. In this case only the energy for one image along the diffusion path, i.e. moving the migrating oxygen into the interstitial tetragonal binding site was calculated, and found to be ∼1.9 eV higher than the initial energy. The energy difference is very close to the corresponding barrier in the bulk (2.0 eV). Therefore, for Cu_2O the respective order of the EP and FP barriers is the same in bulk and at the vicinity of the surface.

CuO(111) CuO(111) surface (top view shown in Figure 3.7(c)) was constructed with bulk-like antiferromagnetic magnetic ordering, shown in Figure 3.7(d). Two different copper atoms Cu_3^{surf} and Cu_4^{surf} are present which coordinate with two surface and one subsurface oxygens or four surface oxygens, respectively. The surface has also two different oxygens: O_3^{surf} is coordinated with three surface cations while O_4^{surf} is bonds with three surface copper atoms and one subsurface Cu. The calculations do not show significant differences in the charge states between the differently coordinated species: Bader charges for Cu_3^{surf} atoms +1.04e and for Cu_4^{surf} +1.08e. For oxygen atoms O_3^{surf} and O_4^{surf} atoms the charges are -1.08e and -1.10e, respectively.

To address the reduction from CuO to Cu_2O with more detail, $V_{O,\,surf}$ for CuO(111) surface was calculated with two coverages $\Theta = \frac{1}{4}$ and $\Theta = \frac{1}{16}$. The vacancy formation energies for O_3^{surf} and O_4^{surf} are according to the calculations 2.50 eV and 2.84 eV, respectively. Maimaiti *et al* have calculated utilizing PBE+U method similar values of 3.02 eV and 3.52 eV. While the absolute vacancy energies show ∼0.5-0.7 eV difference, the relative energy difference of two vacancies remains the same. The same trend is remained with $\Theta = \frac{1}{16}$ coverage (removing one atom from 4×2 surface). Vacancy formation energies are 2.26 eV and 2.71 eV for three- and four-fold surface oxygen atoms, respectively. The lower vacancy formation energy for O_3^{surf} compared to O_4^{surf} is not surprising because of the relative under-coordination.

After removal of an O_3^{surf} atom the most distinct change at the surface is that the nearest Cu_3^{surf} atom moves strongly outwards from the created vacancy and forms a new bond with the nearest O_3^{surf} atom. The resulting bond distances related to this change alongside with the most relevant changes in Bader charges

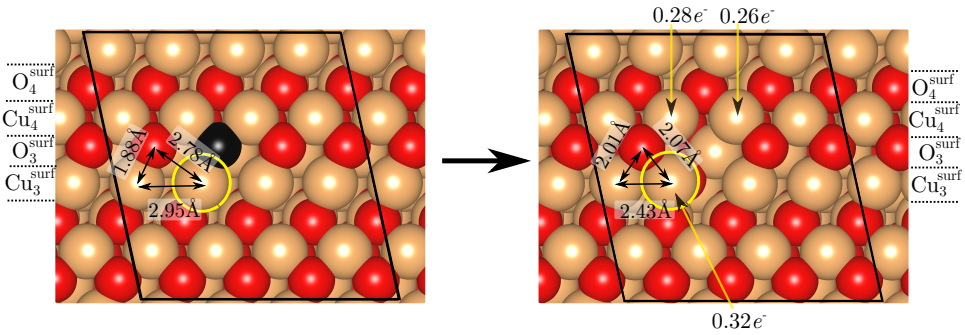

(a) Relaxation of atoms around V_{O_3}

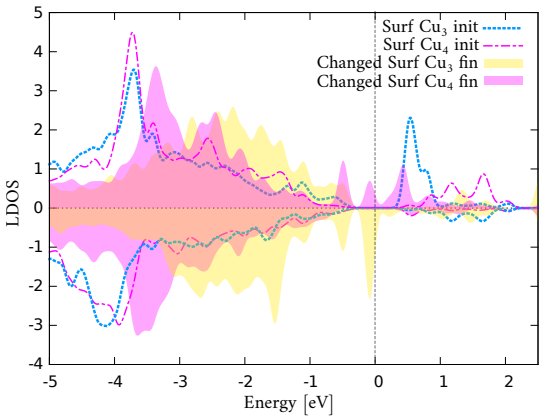

(b) LDOS

Figure 3.12. *(a) The relaxation of atoms around* $\Theta = \frac{1}{16}$ O_3^{surf} *vacancy and (b) the associated changes in LDOS. The labels on both sides of Figure (a) refer to whole rows of surface atoms.*

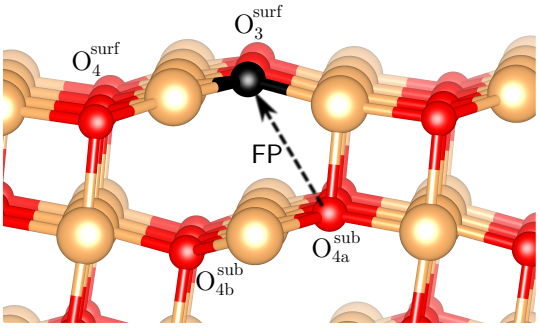

Figure 3.13. *Studied diffusion route in the vicinity of CuO(111) surface.*

are presented in Figure 3.12(a). The positions of the other surface atoms remain relatively unchanged. The excess charge left by the removed oxygen atom is distributed rather evenly to the three surrounding copper cations at the surface layer. Two Cu_4^{surf} atoms reduce by 0.26-0.28e while the Cu_3^{surf} atom having the most distinct lateral re-coordination reduces by 0.32e. This is evident also from the LDOS figures. Plotting LDOS for the nearest Cu_3^{surf} and Cu_4^{surf} atoms before and after a vacancy is being introduced reveal that the DOS of both atoms is red-shifted, see Figure 3.12(b). However, this type of shift expressed by Cu_3^{surf} atom is much more distinct.

The diffusion from subsurface layer onto the first layer of CuO(111) surface was studied taking O_3^{surf} vacancy with $\Theta = \frac{1}{16}$ coverage as the initial state. The diffusion path considered is presented in Figure 3.13. There are two different kinds of oxygen atoms at the second layer of the surface, denoted as O_{4a}^{sub} and O_{4b}^{sub}. Earlier recent PBE+U calculations[116] have provided strong support for O_{4a}^{sub} being the most stable subsurface vacancy by clear margin of ~ 0.8 eV for which reason diffusion of O_{4a}^{sub} into O_3^{surf} vacancy was only studied. Moreover, this diffusion path corresponds to the FP in bulk CuO which was found the most favorable route. The calculations show for this path diffusion barrier of 1.0 eV. The resulting subsurface vacancy is $\sim$0.3 eV lower in energy than the surface deficiency which is perfectly in line with the study by Maimaiti *et al.*

To summarize, compared to bulk CuO the vacancy formation energy is greatly decreased by 1.3 eV together with the diffusion barrier which is 0.5 eV lower at the surface. The increased reduction rate at the surface applies also for $Cu_2O(111)$ for which $\sim$ 0.6 eV lower energy for anion vacancy formation was found compared to the corresponding bulk. Also E_{vac}^{surf} for $Cu_2O(111)$ surface is mainly lower compared to CuO(111) which would indicate, that the reduction rate of copper oxide increases as the oxygen content decreases. The tendency for

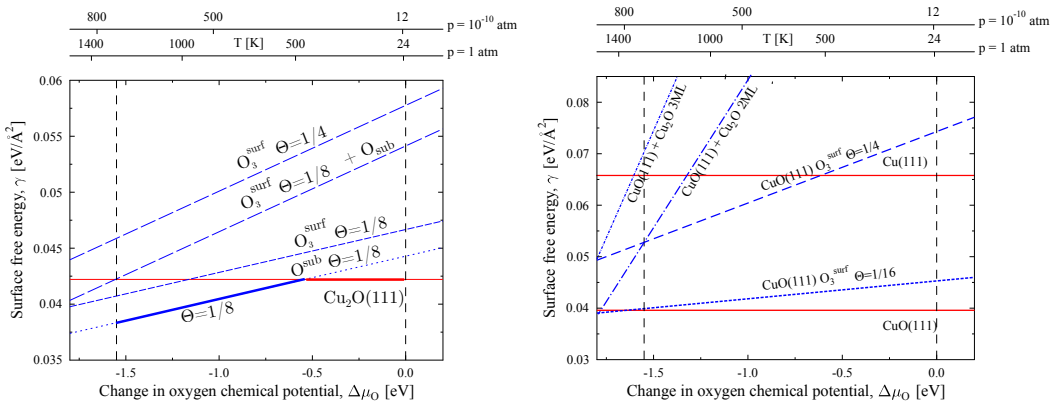

(a) $Cu_2O(111)$ (b) CuO(111)

Figure 3.14. *The surface free energies of ideal and oxygen deficient most stable copper oxide surfaces as the function of chemical potential of oxygen.*

the reduction of copper oxide was studied by utilizing the theory of atomistic thermodynamics, which is addressed next.

Atomistic thermodynamics Surface free energy plots as the function of oxygen chemical potential of CuO and Cu_2O are presented in Figure 3.14. Comparing the plots to corresponding results for manganese oxides a clear difference between these oxides in the mechanism of reduction can be seen. The stoichiometric CuO(111) surface is energetically the most favorable even under oxygen-poor conditions (at the lower limit of the oxygen chemical potential). The reduction process is therefore non-spontaneous at any vacuum annealing conditions. This result is perfectly in line with Maimaiti *et al*[116] who arrived at the same conclusion. They also studied the affect of H2 adsorption on the reduction process of CuO(111) surface and found that applying reducing agent, such as H2, is indeed required to reduce the surface. In CLC conditions the fuel molecules act as reducing agents.

$Cu_2O(111)$ surface does not seem to have same kind of restrictions for reducing process, since oxygen vacancy defected surfaces become favorable at relatively oxygen-rich conditions. Again, this indicates that once CuO surface is reduced into Cu_2O, the reduction process comes more rapid. However, further reduction into pure copper seem not to be favorable without applying stronger reducing conditions.

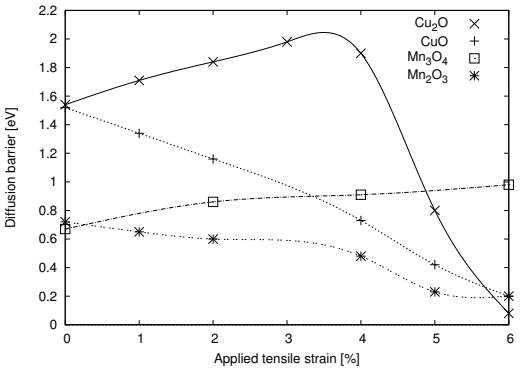

Figure 3.15. *Diffusion barriers for each studied metal oxide bulks along the most favorable path under unstrained conditions as the function applied tensile strain.*

3.1.4 The effect of straining to the kinetics in bulk

As stated in section 1.1.3, lattice straining is expected to have significant impact on the oxygen transport properties in OC particles. Therefore, the affect of tensile straining of the bulk lattice to the diffusion barriers was studied by increasing the lattice constants in x, y and z directions equally up to 6 % compared to the ideal bulk. Subsequently, for each strain, a NEB calculation to determine the barrier for oxygen migration into an vacant site, along the path which was found energetically the most favorable in the case of the unstrained structure, was performed. Additionally for Mn_3O_4 and Cu_2O the second most favorable paths were calculated to check if the favorability of migration paths tend to change as the strain increases. The calculations show substantial differences in the relationships of applied strains and diffusion barriers between different migration paths. The underlying reasons for any changes and differences between the studied materials are also being discussed.

The results for the diffusion barriers as the function of strain for paths yielding the lowest barrier under unstrained conditions are summarized in Figure 3.15. As can be seen, in Mn_2O_3 and CuO oxides the diffusion barrier behaves as intuitive: the barrier lowers steadily as the function of applied strain. However, in Mn_3O_4 and Cu_2O the behavior is different. In Mn_3O_4 the barrier energy increases steadily as the function of strain at least at the studied range. In Cu_2O the affect is similar under strains up to 3 % above which the diffusion barrier decreases dramatically close to zero. Thus, the affect of straining is differing amongst the studied materials and these variations are considered more closely.

In Mn_2O_3 and CuO structures the decreasing migration barrier can be ex-

plained by increased space along the diffusion path and weakening of M-O bonds. This can be noticed by examining the relative positions of the cations near the transition state in the unstrained system. In both materials the migrating oxygen must "push through" the cation atoms in order to reach the target site. In ideal Mn_2O_3 the edge Mn-Mn bond increases at the transition state by 0.2 Å compared to the initial state, which indicates that the oxygen atom must clear the route first in order to migrate into the empty site. The corresponding TS bond lengths are independent to the applied strain. The gap between the two manganese atoms in the initial state increases as the function of the applied tensile strain and at 6 % the gap is 3.70 Å. In the transition state the gap is 3.63 Å. Thus, the displacement of metal cations need to be very minor for the diffusion of oxygen atom which explains the low barriers under high strain. It could be speculated that under strains >6% the barrier could increase again. However, structure becomes very unstable and does not resemble original conformations when strains with this magnitude are applied.

Next the unconventional behavior of Mn_3O_4 and Cu_2O are addressed. The nature of Mn_3O_4 FP path is different compared to the most favorable paths in Mn_2O_3 and CuO since the oxygen is more free to move. This is evident from the relaxations of Mn cations around the diffusion path (see Figures 3.16(a) and 3.16(b)). Cations are not blocking the diffusion path and the Mn-O bonds around are elongated at TS (in contrast to EP in Mn_2O_3 and FP in CuO where the bonds are contracted). This creates unfavorable stress to the lattice which is seen as an increasing diffusion barrier as the function of lattice strain. Under 6 % strain the migrating oxygen coordinates with three Mn atoms with bond lengths of 2.18 Åto 2.48 Å. However, to form this coordination two Mn(II) atoms need to adapt their coordination by breaking one Mn-O bond (wavy dashed line in Figure 3.16(d)). This kind of awkwardness induced to these two Mn(II) atoms by the lattice straining seems to be the main reason for increasing diffusion barrier in FP path in Mn_3O_4

Moving on to Cu_2O FP, the unusual behavior of diffusion barrier as the function of strain can be explained by similar kind of reasoning as above. Like in Mn_3O_4 FP there are no cations blocking the diffusion path and at the TS Cu-O bonds nearby the migrating oxygen are all elongated compared to the initial state (see Figures 3.17(a) and 3.17(b)). At 3 % strain bonds of all cations enclosed by the yellow quadrangle in 3.17(d) are similarly geometrically frustrated due to the moving oxygen. However, at the higher strains the frustration is relieved as the Cu-Cu bonds around vacant anion sites are broken and the

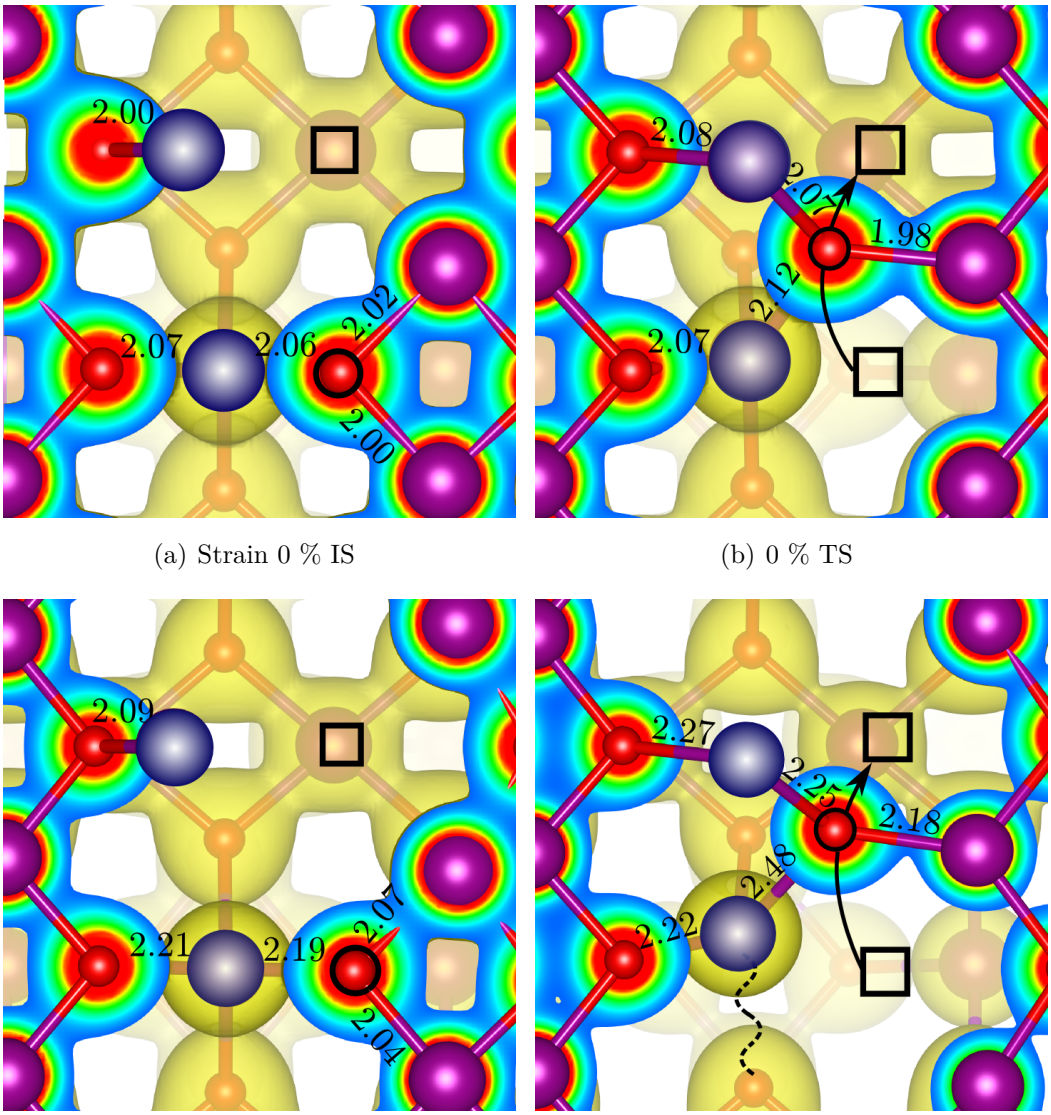

(a) Strain 0 % IS

(b) 0 % TS

(c) 6 % IS

(d) 6 % TS

Figure 3.16. *The FP diffusion path in Mn_3O_4 bulk without strain ((a) and (b)) and under 6 % lattice strain ((c) and (d)). The image on the left (right) side corresponds to initial (transition) state. The migrating oxygen is marked with black circle, vacant anion sites are black squares, Mn(III) atoms are purple, Mn(II) are dark blue and O atoms are red. The bond lengths are in Å and the isosurfaces of electron densities illustrating the strength of Mn-O bonds are presented at the 0.05 $e/Å^3$ level. Under 6 % strain at TS one nearby Mn-O bond needs to be broken (marked with dashed wavy line) to stabilize the migrating oxygen.*

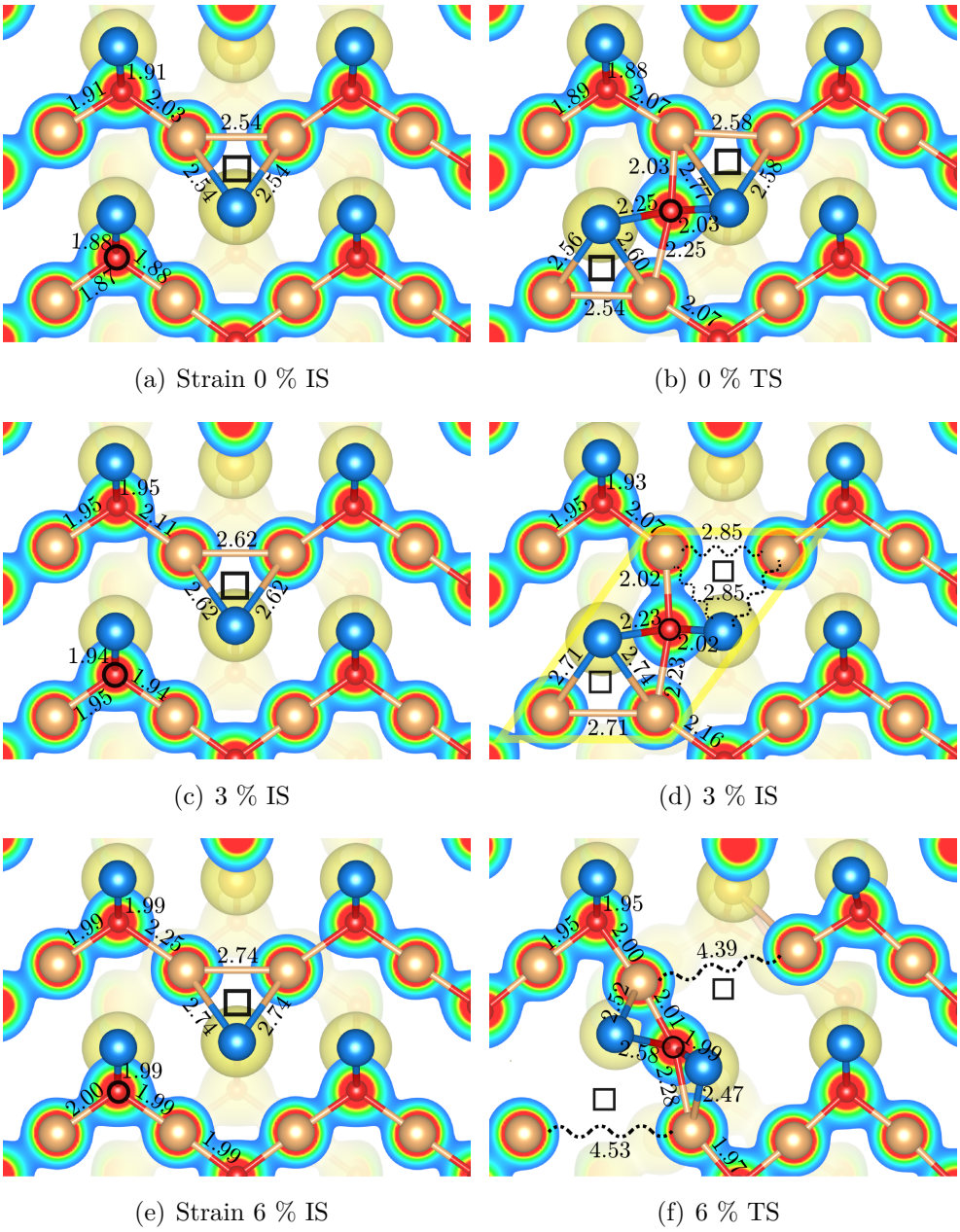

(a) Strain 0 % IS

(b) 0 % TS

(c) 3 % IS

(d) 3 % IS

(e) Strain 6 % IS

(f) 6 % TS

Figure 3.17. *The FP diffusion path in Cu_2O bulk without strain ((a) and (b)), under 4 % lattice strain ((c) and (d)) and under 6 % strain ((e) and (f)). The image on the left (right) side corresponds to initial (transition) state. The migrating oxygen is marked with black circle, vacant anion sites are black squares, oxygen atoms are red and Cu atoms are light brown on the electron density cut-off plane or blue if the atom lies above it. The bond lengths are in Å and the isosurfaces of electron densities illustrating the strength of Cu-O bonds are presented at the 0.05 $e/Å^3$ level. The key bonds broken upon diffusion compared to the IS are indicated with dashed wavy lines.*

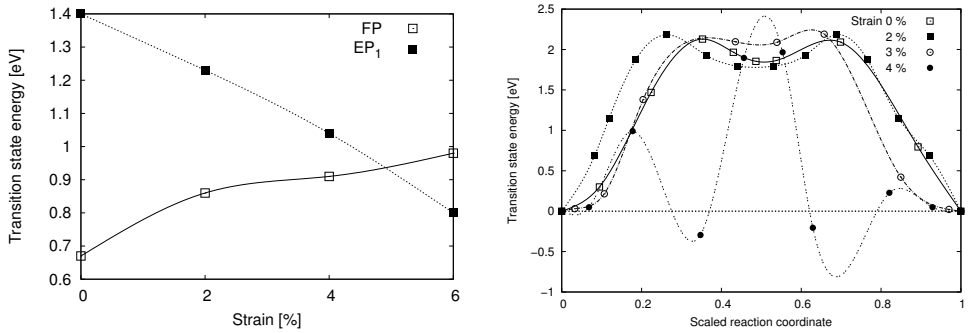

(a) Mn_3O_4 FP and EP_1 (b) Cu_2O EP

Figure 3.18. *(a) The comparison of FP and EP_1 diffusion paths in Mn_3O_4 as the function of applied tensile strain and (b) energetics of EP path under different strains.*

system is able to form at the transition states similar type of Cu-O-Cu chain as in the ideal bulk. Therefore, in this case the increased flexibility of the total structure decreases the migration energy as the strain is increased beyond 3 %.

The increasing diffusion barrier for FPs in Mn_3O_4 and Cu_2O raises a question whether EP paths showing higher barriers under unstrained conditions could become energetically most favorable when tensile straining is introduced. Therefore EP_1 of Mn_3O_4 and EP of Cu_2O were calculated similarly under different strains and the results are presented in Figures 3.18(a) and 3.18(b). As can be seen, the barrier of EP, which shows over 0.7 eV higher diffusion barrier under unstrained conditions compared to FP, decreases steadily similarly to EP in Mn_2O_3 bringing this path most favorable at strain $\sim$ 5 %. This is understandable using the same arguments as in the case of Mn_2O_3 diffusion. Increased strain opens the gap between two manganese atoms leaving more space for oxygen to move.

The EP diffusion energetics in Cu_2O, shown in Figure 3.18(b) shows two separate peaks with lower strains associated with two different Cu-Cu edges along the path. The plateau between these two peaks corresponds to initially empty tetragonal anion binding site. At 4 % strain the barrier associated to penetrating the Cu-Cu edge has been lowered to 1 eV. However, the interstitial tetragonal site remains unfavorable with energy $\sim$ 2 eV over the initial state energy. Therefore only at 3 % strain the barrier for EP path is comparable with FP path and outside this region FP dominates the diffusion process.

3.2 CO_2 on Au/MgO(100)/Ag and C_2O_4 formation

In this chapter the focus is changed to utilization of CO_2 molecule formed e.g. by CLC process. As discussed in Chapter 1, normally the value-adding reactions of carbon dioxide are hindered by its exceptionally stable structure. In this work it was studied if nanosized gold supported by Ag/MgO, representing a typical metal-insulator-metal (MIM) system, could act as catalysts for $CO_2 + CO_2 \longrightarrow C_2O_4$ reaction. The key is to first form reactive CO_2^- radical ion by shuttling electron either directly from Ag or alternatively from Au island on top of MgO to an absorbed CO_2. The formed radical may further act to for an oxalate C_2O_4.

The model system introduced in Section 2.8.2 is based on an experimental study conducted by Calaza *et al.* [1] who prepared thin Au/MgO(001) films supported by Ag(001) and studied CO_2 adsorption on them with scanning tunneling microscopy and infrared (IR) spectroscopy. The average size of the Au clusters was $\sim 5 \times 5$ nm^2. The results suggest that CO_2 and its derivatives adsorb almost exclusively at the rims of Au islands with approximated separation distance of ~ 1 nm. Also, IR spectrum of CO_2 adsorbed Au/MgO, presented in Figure 3.19(b), shows two extra bands compared to similar measurement without gold clusters, shown in 3.19(a). It can be speculated that these peaks are originated from oxalate species. The calculations presented next for adsorption energies and vibration spectrum for different CO_2 species indeed support this hypothesis. Additionally, the reaction path and energetics of oxalate forming process was studied in detail. The first results for CO_2 and C_2O_4 adsorption using the smallest models based on ad-Au_1 and -Au_2 have been presented already in article [1], but in this thesis more detailed description is given.

Since the properties of Au islands on MgO/Ag thin films have been studied extensively in e.g. [110, 111, 112, 113], this study is focused only on the CO_2 and C_2O_4 adsorption characteristics on these systems. Both experiments and calculations have shown that Au clusters on MgO/Ag thin films acquire flat geometry and are charged negatively. The most stable conformation for smaller Au clusters (2-6) has been found to be chain-like linear [143] while larger clusters are island-like. The additional electrons repel each other strongly and are thus distributed mainly amongst the edge Au atoms in island-like configurations. This would suggest that the chemically most active areas of such systems are located at the edges. This is supported by the experimental study by Calaza *et. al.* [1]. It has to be noted, however, that the total charge of Au island does

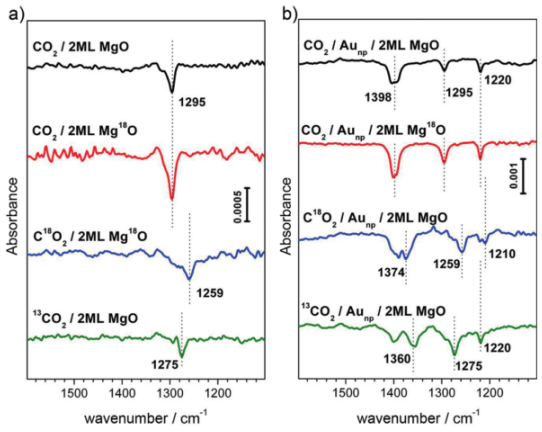

Figure 3.19. *The experimental IR absorbance spectra for (a) CO_2 adsorption on MgO(100)/Ag(100) and (b) Au/MgO(100)/Ag(100) surface. The figure is obtained from [1].*

not increase linearly as the size increases, as can be seen from the third column of Table 3.6. In the same table the formation energies E_{form} of Au clusters on MgO/Ag surface, calculated in relative to the clean MgO/Ag surface and bulk Au, are presented showing clear trend for lower formation energy as the size of the cluster increases. Additionally, the formation energy for semi-infinite stripes are lower than for two-dimensional islands indicating that even larger Au islands are preferred.

3.2.1 CO_2 Adsorption Energies

The first step concerning the C_2O_4 anion formation on different Au/MgO/Ag model systems was to determine single CO_2 adsorption energetics and the results have been presented in Table 3.6. Since all of the models in this work are based on the same 2 ML MgO on 3 ML Ag, the Ag is left out from the labeling of different systems henceforth. The adsorption energy on clean MgO(001) surface was calculated for baseline for other models and exothermic energy -0.30 eV was found. The most stable configuration for CO_2 adsorption is surface-planar, presented in Figure 3.20(a) and henceforth referred as MgO(P), in which C bonds with lattice O atom while the adsorbate O atoms coordinate with Mg atoms. At this configuration, CO_2 has a negative Bader charge of -0.42e indicating that it has accepted electrons upon adsorption. Comparing the Bader charges of MgO/Ag slab with and without the adsorbate reveals that the underlying Ag layers have donated -0.10e of this charge while the rest of it is donated by the lattice O atom bonding with C. Due to the induced partial

Table 3.6. Au cluster formation energies on MgO/Ag, CO_2 adsorption energies, corresponding geometry, Bader charge, bond lengths and relevant d- and p-band centers (dbc and pbc) determined from DOS plots.

	E_{form}/Au [eV/Au]	q(Au_{tot}) [e]	Ads. Geom. P/N	$E_{ads}(CO_2)$ [eV]	q(CO2) [e]	d(C-Au) [Å]	dbc Au [eV]	pbc C [eV]
Clean MgO	-	-	P	-0.30	-0.42	-	-	-7.549
Au_1	1.17	-0.81	P	-0.57	-0.72	2.12	-1.735	-7.325
	1.16	-0.76	N	-0.39	-0.53	2.20	-1.329	-6.913
Au_2	0.94	-1.05	P	-1.03	-1.04	2.10	-2.555	-5.995
	0.94	-0.97	N	-0.56	-0.78	2.17	-2.494	-5.914
Au_8	0.69	-1.73	P	-0.36	-0.94	2.13	-3.002	-6.223
Au_{11}	0.60	-1.97	P	-0.37	-0.91	2.13	-3.198	-6.573
Au_{12}	0.56	-2.21	P	-0.41	-0.79	2.13	-3.197	-7.098
Au_{13}	0.54	-2.71	P_1	-0.41	-0.84	2.13	-3.018	-6.836
	0.54	-2.71	P_2	-0.37	-0.86	2.15	-3.045	-6.790
Au_{14}	0.50	-2.21	P_1	-0.19	-0.87	2.14	-3.308	-6.597
	0.50	-2.21	P_2	+0.02	-0.87	2.14	-3.308	-6.597
	0.50	-2.21	MgO(P)	-0.10	-0.46	-	-3.308	-7.595
Au_{str} (110)	0.49		P	-0.63	-0.93	2.16	-2.968	-6.295
Au_{str} (100)	0.43		P	-0.11	-0.90	2.17	-3.209	-6.573

charge the linear conformation of C-O double bonds breaks and the molecule adapts a 133.4° angle.

In principle there are two different viable ways for CO_2 to adsorb at the edge of Au cluster on MgO, surface parallel (P) and surface normal (N) configurations, presented in Figures 3.20(b) and 3.20(c), respectively. These configurations are labeled as Au_x(P/N), where x is the size of the Au island on MgO. When CO_2 adsorbs on a single Au atom, the corresponding energy is by 0.1-0.3 eV more exothermic compared to MgO(P), as can be seen from Table 3.6. Also in this case the surface planar configuration is the most favorable, resulting in an adsorption energy of -0.57 eV while for Au_1(N) configuration the binding energy is -0.39 eV.

The CO_2 adsorption energies for both (N) and (P) configurations are increased significantly with an Au dimer. The stronger CO_2 binding is also associated with larger charge transfer which originates mainly from Au atom next to CO_2 and the underlying Ag layer. No binding and charge transfer is seen when the adsorbate is placed on top of the Au_1 or Au_2. This indicates that for the most efficient charge shuttling and CO_2 binding interactions equally with both the substrate and Au atom are required. It is easy to see that (P) conformation maximizes these mutual interactions. The interactions between Au, MgO and CO_2 for (P) and (N) configurations are illustrated in Figure 3.21, which shows the electron density difference, $\Delta\rho = \rho(Au_1{-}CO_2/MgO/Ag) - \rho(Au_1/MgO/Ag) - \rho(CO_2)$. Clearly charge is accumulated at the interface of the adsorbate O and lattice Mg atoms more in (P) configuration indicating stronger interaction. In addition to interaction with

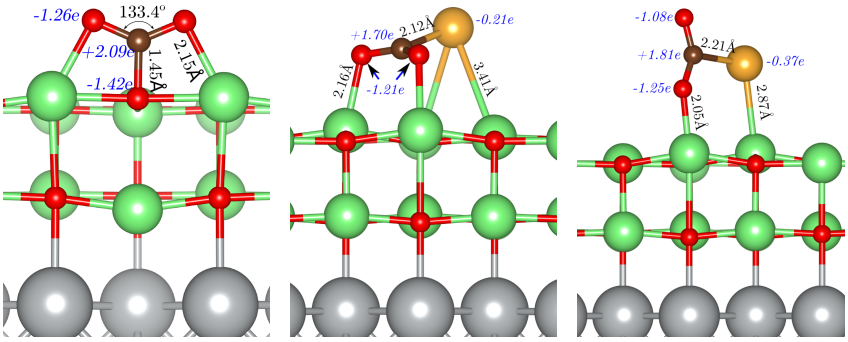

(a) Au-CO_2 Planar (P) on MgO (b) Au-CO_2 (P) on Au/MgO (c) Au-CO_2 Normal (N) on Au/MgO

Figure 3.20. *(a) The surface-planar (P) and (b) surface-normal (N) adsorption configurations of Au-CO_2 complex. The Bader charges and bond lengths have been indicated by blue italics and black normal text, correspondingly.*

the lattice, adsorbing CO_2 induces also polarization in the Au atom as charge is accumulated from the opposite side to the Au-C bond.

Increasing the size of ad-Au cluster to 8 and up to 14 reveals that there is no clear direct correlation between the number of Au atoms and the CO_2 adsorption energy or magnitude of charge transfer. The C-Au bond length (seventh column in Table 3.6) is clearly shortest for Au_2 on which the adsorption energy was the most favorable. However, for other systems the correlation between the bond length and adsorption energy is not such clear which shows that the bonding strength does not solely depend on the electrostatic interactions between the adsorbate and the substrate.

For the larger Au-islands only P configuration was considered since it was found clearly the most stable for $x = 1$ and $x = 2$. For Au_8-Au_{13}(P) the calculations show $\sim$ -0.4 eV energy while for Au_{14} the corresponding energy is -0.2 eV, indicating weaker bonding compared the MgO(P). As can be seen from Figures 2.2(c) to 2.2(g) there are multiple possible adsorption sites for (P) configuration. However, the energies for these different sites do not seem to vary much. Also moving the island as a whole, to allow better interaction with lattice Mg and adsorbate O atoms, was tested and no clear change in energy was observed which would indicate that the size of ad-Au island is the determinant for $E_{ads}(CO_2)$.

The adsorption on semi-infinite Au-stripes, modeling the edge of larger Au cluster, is strongly dependent on the type of the stripe. For (110) stripe model

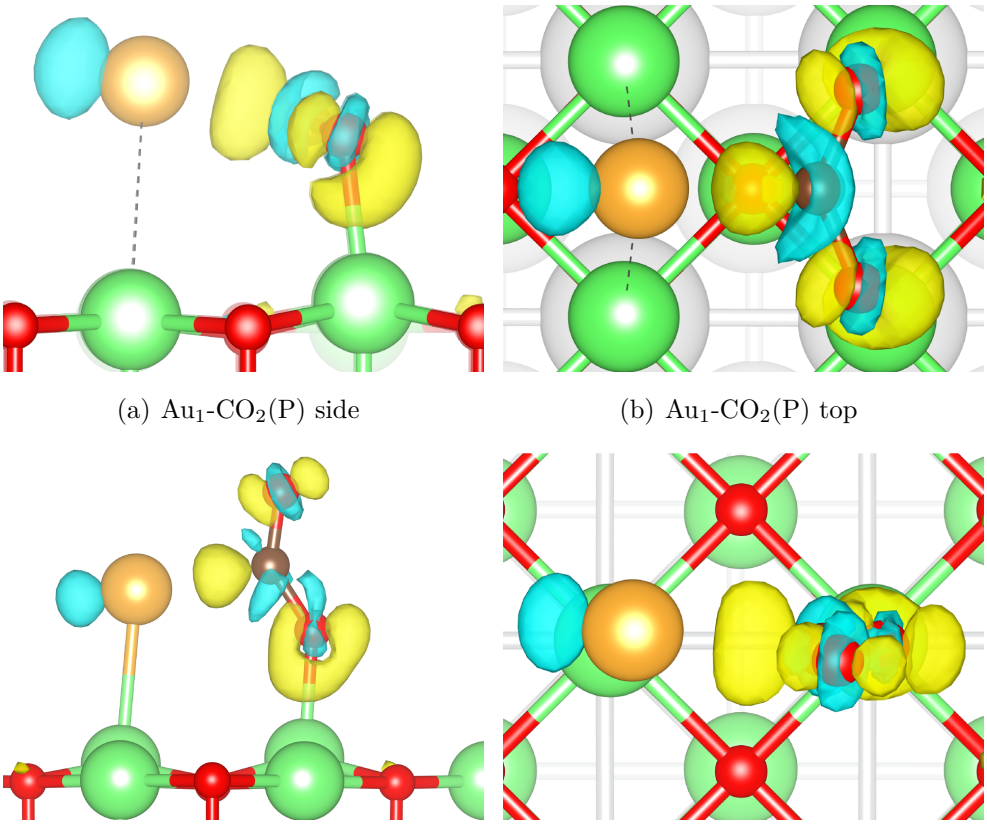

(a) Au_1-CO_2(P) side

(b) Au_1-CO_2(P) top

(c) Au_1-CO_2(L) side

(d) Au_1-CO_2(L) top

Figure 3.21. *The electron density difference mappings for Au_1-CO_2(P) ((a) & (b)) and Au_1-CO_2(L) ((c) & (d)) configurations associated with CO_2 adsorption. The isosurface levels are* 0.05 e/Å^2. *Yellow (blue) volumes represent electron density increase (decrease).*

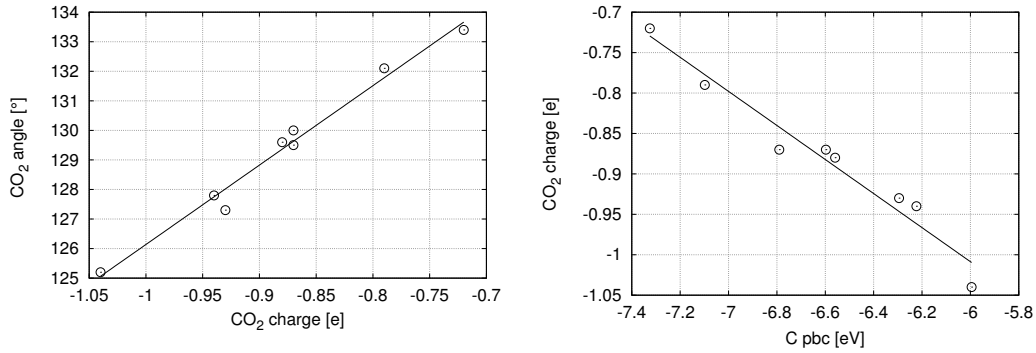

(a) q(CO_2) vs. α (b) C pbc vs. q(CO_2)

Figure 3.22. *(a) The angle of adsorbed CO_2 molecule as the function of its Bader charge calculated for Au_x-CO_2 systems and (b) the Bader charge of adsorbed CO_2 atom plotted as the function of the p-band center of carbon atom. The solid lines are linear fits.*

(presented in Figure 2.2(i)), where the edge is also slightly stretched ($\sim 5.5\%$) compared to the (100) model, a favorable adsorption energy of -0.6 eV is found. However, for the (100) stripe the corresponding energy is only -0.1 eV. In these cases, Au islands and stripes, there is no clear correlation between the transferred charge and adsorption energy. Therefore some other indicator for the bonding strength has to be found. The shuttled excess charge correlates, however, linearly with the angle adapted by the CO_2 molecule, as can be seen from Figure 3.22(a). The bending also moves the p-states of CO_2 towards the Fermi-level yielding a linear dependency between the p-band center, calculated using Equation 2.46, and $q(CO_2)$ presented in Figure 3.22(b). The Bader charge is therefore a good measure for the possible degree of activation and tendency to form oxalate species.

Interestingly, Bader analysis shows that systems with larger Au island seem to have higher electron transfer capabilities from the Ag substrate. E.g. when Au14-CO_2 system is considered, -0.63e charge has been transported from the Ag layer, -0.24e from MgO and Au contributes only -0.01e of the total charge transferred to CO_2. Already with Au dimer -0.41 charge is transported from the Ag layer to the adsorbate even though it has to be noted that the number of Ag atoms within the unit cell is smaller by the factor of $\frac{9}{16}$ compared to Au_{14} system. In comparison, for Au_1-CO_2 (P) system only -0.07e of the total CO_2 Bader charge of -0.72e is transported from the Ag, -0.06e from MgO and the remaining -0.60e from the Au atom. Therefore Au clusters seem to enhance the

electron shuttling through the 2 ML MgO.

3.2.2 DOS comparison between Au_x and Au_x-CO_2 systems.

To understand the observed differences in CO_2 adsorption energies between different Au-cluster models, the chemistry of these systems has to be characterized in more detail. In interactions involving charge transfer, like in the case of CO_2 adsorption on Au/MgO/Ag systems, Lewis acidity concept is a handful tool to determine the strength of the interaction [91]. There are numerous definitions for the Lewis acidity but here Lewis acid/base is simply defined as electron acceptor/donor. The strength of the bonding is determined by the relative acidity of the two reacting species, i.e. the Au/MgO/Ag adsorption site and CO_2. In the case of CO_2-Au/MgO/Ag systems CO_2 acts as a Lewis acid, since it accepts electrons upon adsorption, and accordingly the Au cluster and the substrate are Lewis bases. Therefore, determining the relative basicity of each Au-cluster should show correlation with the CO_2 adsorption energy. Fortunately there are ways to establish scales for the acidity. One qualitative method is to use orbital energies: lower LUMO energy means stronger Lewis acid and similarly higher HOMO indicates stronger base. HOMO and LUMO energies are not observable quantities in experiments, but several computational studies have shown that this definition can be used to predict the trends in adsorption energies reliably [144, 145, 146].

To study the differences between Au clusters with varying sizes, the DOS plots were acquired. The *spd*-, *p*-only and *d*-only projections of Au_x on MgO densities of states with and without CO_2 adsorbate are presented in Figure 3.23. As can be seen from the figure, there are clear qualitative differences between the small Au_1 and Au_2 models. The *d*-projected Kohn-Sham density of states for Au_1 is relatively narrow centered around -1.7 eV and shows only two peaks whereas at Au dimer the *d*-states are spread between the energies -4 to -1.7 eV. In general, increasing the size of Au island seems to spread the *d*-states and more and more continuous band is acquired. Also, new bands consisting mainly of *s*- and *p*-states appear at the proximity of the Fermi-level.

The HOMO of Au dimer, consisting mainly *s*-states lies practically at the Fermi-level while at Au_1 the corresponding energy is -0.4 eV which would indicate stronger basicity in favor of the dimer. Also, for the dimer HOMO is actually a singly occupied orbital (SOMO), which can be seen by comparing the spin-up and spin-down electron states. This is unique to Au dimer amongst the studied systems. These kind of orbitals seem to indicate particularly strong

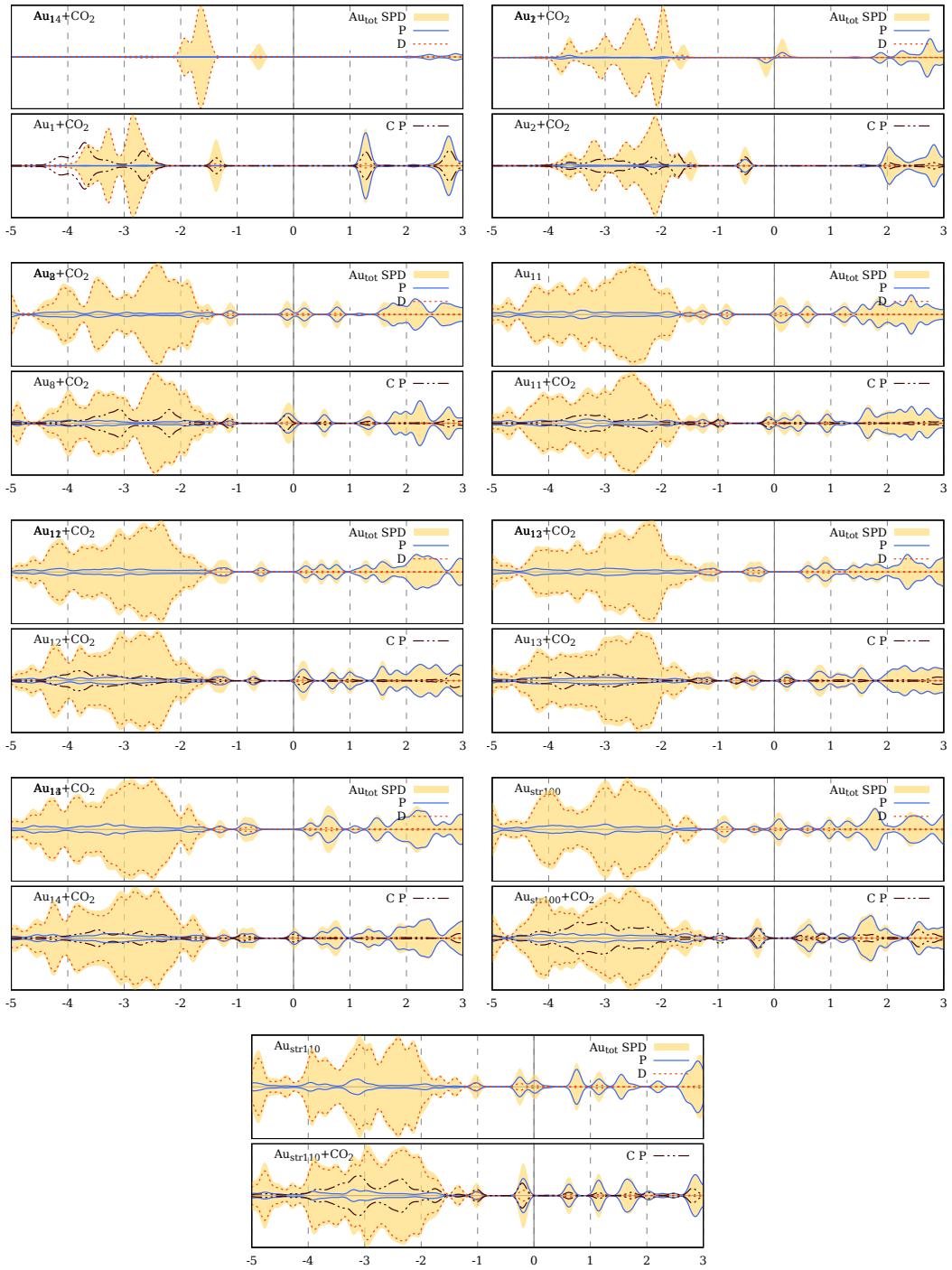

Figure 3.23. *DOS plots for Au/MgO/Ag systems with cluster sizes between 1 to 14. The upper figure shows SPD, P and D -projected DOS for the whole Au cluster while the lower image is the similar plot for Au_x-CO_2 system alongside with P-projection of the adsorbate which is scaled using the factor of 5 for clusters with $x > 2$.*

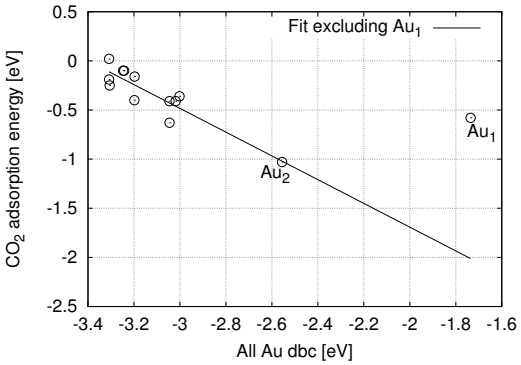

Figure 3.24. *CO_2 adsorption energy vs. the combined d-band center of all Au atoms. The data is fitted with a linear function. Only the data for (P) adsorbate configurations are shown because of the substantial differences on the adsorbate-substrate interactions.*

basicity due to the absence of electron pairing effect leading to higher energy [146]. These two points indicate that clearly Au_2 is stronger Lewis base compared to Au_1 which explains well the calculated over 0.4 eV difference in CO_2 adsorption energies compared to any other ad-Au system.

For larger Au islands the HOMO energy analysis does not seem to give as clear correlation as in the case of Au_1 and Au_2 system. However, plotting the CO_2 adsorption energy against the *d*-band center calculated from all Au atoms present at the system, reveals linear dependency when Au_1 is excluded (see Figure 3.24). This is not surprising as popular *d*-band center (dbc) model [147] and its extensions have been proved very useful to predict bond formation energetics and catalytic activity among transition metal, such as Au, surfaces [148, 149, 150, 151]. However, it has to be noted, that in *d*-band model it is assumed that the surface expresses continuous band in order to determine a meaningful centroid. As can be seen from the DOS of different Au clusters (Fig. 3.23) Au_1 does not fulfill this requirement and hence *d*-band center model does not apply to it. Increasing the size of the Au cluster also makes the *d*-band more continuous meaning that the model is more applicable.

The *d*-band model, developed by Hammer and Nørskov [152, 153], describes approximately the interaction between adsorbate valence states and the *s*- and *d*-states of metal surface. Coupling to the metal *s*-states gives rise to a shift and broadening of the adsorbate valence states. Similarly coupling with substrate *d*-band leads to formation of bonding and antibonding states in the coupled system. The strength of the bonding is described by relative filling of these states. Because all transition metals have broad and half-filled *s*-bands, the

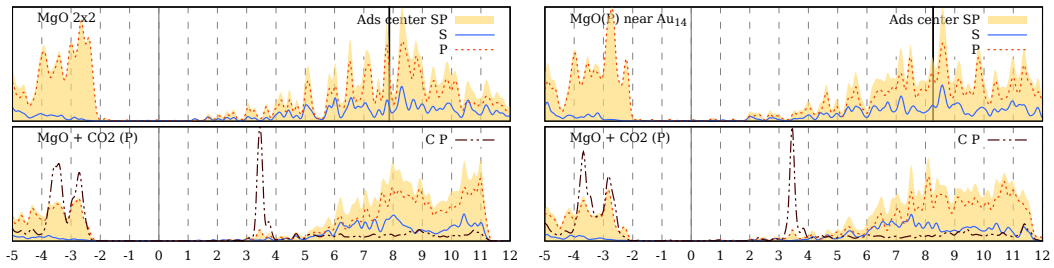

(a) $MgO\text{-}CO_2(P)$ (b) $Au_{14}\text{-}MgO\text{-}CO_2(P)$

Figure 3.25. *DOS plots for (a) $MgO\text{-}CO_2(P)$ and (b) $Au_{14}\text{-}MgO\text{-}CO_2(P)$ systems without/with adsorbate (upper/lower plots). The s-conduction band centers for the adsorption center (see text) have been indicated by solid vertical lines.*

differences between different systems can be quantified with the properties of *d*-states [91]. Therefore the energy of *d*-states, and particularly the centroid of the band, in relative to the Fermi-level is a good first approximation of the interaction strength. Higher *d*-band center of the substrate should yield increased bonding strength since more and more antibonding states are left unoccupied.

3.2.3 Adsorption at the vicinity of Au

Interestingly, the bonding strength on MgO is weakened at the vicinity of Au, i.e. CO_2 in MgO(P) configuration and not in direct contact with any Au atoms (see Figure 3.20(a)) which was demonstrated with Au_{14} island (Au_{14}-MgO(P)). The adsorption energy for this configuration is only -0.10 eV, while for clean MgO corresponding energy of -0.30 eV was found. The difference is not explained by different coverages. The variation is actually accounted for the differences in adsorption site Lewis acidity, which becomes evident when DOS of both systems are examined (see Figure 3.25). Here the DOS has been constructed by summing the LDOS of two substrate Mg and one O atom forming the site for CO_2(P) adsorption. In this case the HOMO energies for both adsorption sites, MgO-(P) and Au_{14}-MgO-(P) are close to each other. However, the presence of Au modifies the site conduction band forcing them higher in energy. This is important since the conduction band centroid E_c^* has been recognized as practical descriptor for Lewis acidity in [154]. It is calculated as

$$E_c^* = \frac{\int_{E_f}^{\infty} \rho_c(\epsilon)\epsilon \mathrm{d}\epsilon}{\int_{E_f}^{\infty} \rho_c(\epsilon)\mathrm{d}\epsilon}, \tag{3.2}$$

which is the mean of conduction band, which consists mainly of *s*- and *p*-angular momentum terms. In principle the *sp*-projected DOS is integrated from the Fermi-energy to infinity. However, the upper limit is practically defined by the amount of unoccupied states, which is an adjustable parameter in DFT calculations. Because the number of atoms in MgO and Au_{14}-MgO models is different, the empty states were adjusted so that the cut-off energy in both systems was equal. This way the band centroids for both models are comparable with each other. The *sp*-conduction band centers calculated using Equation 3.2 are for clean MgO adsorption site 7.86 eV and correspondingly for Au_{14}-MgO 8.35 eV indicating that the Lewis acidity at the vicinity of Au is decreased, which in turn explains the clear 0.2 eV difference in the CO_2 adsorption energies.

There is a direct consequence of less exothermic adsorption energy near Au islands. Because the bonding strength is more favorable when CO_2 is in contact with Au instead of adsorbing on MgO only, the adsorbates are driven towards the metal clusters. This is in agreement with the experimental results obtained by Calaza *et al.* [1] who found that CO_2 is absorbed preferably at the rims of Au islands while sites at film MgO are relatively empty when Au is present.

3.2.4 Formation of C_2O_4

Oxalate is a dianion ${C_2O_4}^{2-}$, or ${(CO_2)_2}^{2-}$, which is basically two coupled CO_2 molecules with a single C-C bond [155]. The barrier for rotation about the C-C bond is $\sim$ 0.1-0.2 eV the preferred state determined by gas-phase calculations being cross-like (CO_2 units perpendicular). This was also confirmed by the calculations presented here the difference between the two configurations being 0.2 eV. The gas-phase planar and cross-like ${C_2O_4}^{1.8-}$ anions, approximating the full double anion, have been presented in Figures 3.26(d) and 3.26(e). The corresponding C-C bond lengths are 1.70 Åand 1.61 Å.

First to study the C_2O_4 anion formation on Au/MgO/Ag surface I will discuss the binding of C_2O_4 species on different ad-Au clusters and MgO. The labeling of the configurations is similar to the previous one used of CO_2, only now two letters are used for indicating the positions of individual CO_2 parts in relative to the MgO surface. N refers to CO_2 unit coordinated normal to the surface while P stand for surface planar coordination. Label *c* refers to CO_2 unit which is not bound to MgO substrate and is in "cross" position in relative to the other CO_2. Three favorable configurations for ${C_2O_4}^{2-}$ adsorption on pure MgO were found, presented in Figures 3.26(a)-3.26(c): NP_1, NP_2 and PP. In each of these cases the C-C bond length is reduced to 1.55-1.60 Å and the

Table 3.7. Results for computed $C_2O_4{}^{2-}$ structures. Adsorption energies and Bader charges have been reported per one CO_2 unit. The reference state for formation energies E_f is two CO_2 in gas phase.

	$E_{ads}(C_2O_4)/CO_2$ [eV]	$q(C_2O_4)/CO_2$ [eV]	E_f [eV]
MgO: NP_1	-0.32	-0.91	
NP_2	-0.25	-0.93	
PP	-0.46	-0.93	0.4
Au_2: $2N_1$	-0.25	-0.58	
$2N_2$	-0.19	-0.55	
NP	-0.37	-0.80	0.7
Pc	-0.27	-0.78	0.9
PP	-0.57	-0.85	
Au_{14}: Pc1	0.21	-0.80	
Pc_2	0.37	-0.80	
NP	-0.27	-0.86	
$Au_{str}(110)$: NN	-0.18	-0.79	0.7
PP	-0.43	-0.93	0.6
Pc	-0.11	-0.77	0.5

total charge of C_2O_4 species is from -1.8e to -1.9e. The adsorption energies per one CO_2 unit, taking two CO_2 molecules in gas phase as a reference state, are listed in the Table 3.7. As can be seen, the surface planar configuration (PP) is clearly the most stable. Also, in this case the binding energy of -0.46 eV/CO_2 is more favorable than the corresponding energy for CO_2 adsorption on MgO, indicating that merging of two CO_2 molecules is more favorable than two individual adsorbates.

For Au_2 three favorable Au-C_2O_4 species were found. Configurations $2L_1$ and $2L_2$ listed in the Table 3.7 refer to two separate CO_2(N) with no C-C linkage. The energies for these configurations are also exothermic, -0.25 eV and -0.19 eV with -0.6e charge transferred to each CO_2. However, also in this case the merging of two carbon dioxides is found to be the favored state since the adsorption energies for NP, Pc and PP (Figures 3.27(a), 3.27(b) and 3.27(c)) are more exothermic. Again, PP configuration is the most stable with 0.1 eV lower energy compared to the corresponding result for MgO-C_2O_4(PP). From the density difference plots (Figures 3.27(d)-3.27(f)) it can be seen that the Au atom next to the oxalate donates electrons which are accumulated mainly between two C atoms and at the interface of the adsorbate and MgO surface. This is confirmed by the Bader analysis showing that the charge of this Au atom is clearly positive in each case. The density difference plots reveal also

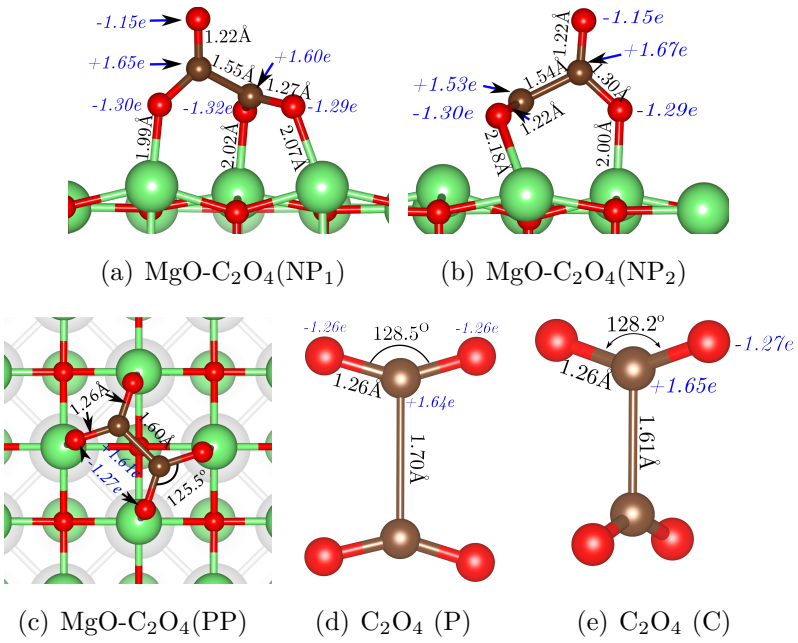

(a) MgO-C_2O_4(NP_1) (b) MgO-C_2O_4(NP_2)

(c) MgO-C_2O_4(PP) (d) C_2O_4 (P) (e) C_2O_4 (C)

Figure 3.26. *Modeled structures for $C_2O_4{}^{2-}$. (a), (b) and (c) Some possible adsorption configurations for C_2O_4 on MgO/Ag surface and (d) planar and (e) cross-like $C_2O_4{}^{1.8-}$ gas-phase configurations.*

that most charge is donated from the interface between the oxalate and Au which indicates that the bond between these species is substantially weaker than the corresponding C-Au bond in Au-CO_2 complexes, where polarization of the Au atom was found (Figure 3.21).

The binding of C_2O_4 complex at the edge of larger Au islands was studied with Au_{14} and Au_{str}(110) models. All computed configurations showed higher energies compared to Au_2 which can be contributed to the lower charge available for donation of edge Au atom (-0.2e compared to -0.5e for Au_2 model). Also the energy for NP configuration is similar to MgO-C_2O_4(NP) indicating that Au the presence of Au does not have a significant effect to the binding of C_2O_4 complex. For Au_{str}(110) unique C_2O_4(NN) configuration was found, shown in Figure 3.27(g). Also in this case the Au atoms at the edge of donate electrons to the C_2O_4 complex, as can be seen from Figure 3.27(h). The energy is exothermic, -0.18 eV, although not as low as for PP configuration.

The barrier for formation of different C_2O_4 complexes was determined utilizing constraint method where C-C bond length was fixed and varied in each subsequent step. The formation energy in each case was found to be associated with the formation of C-C bond. The results listed in the forth column of Ta-

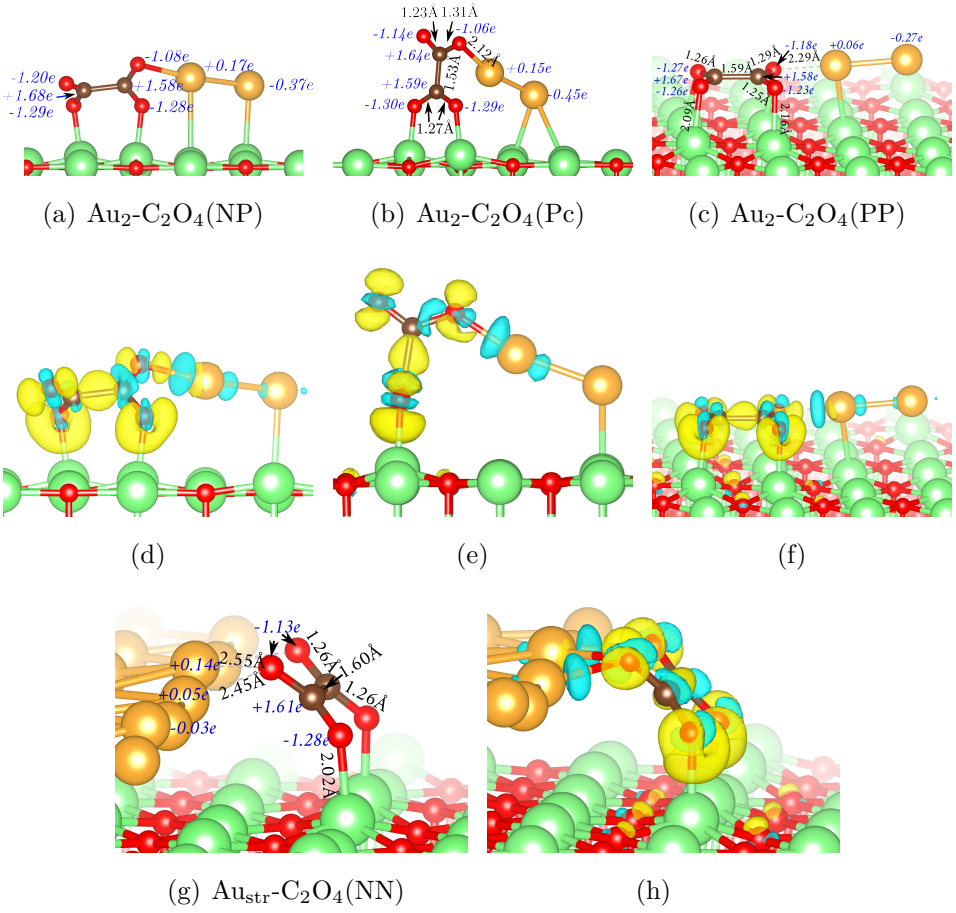

(a) Au_2-C_2O_4(NP) (b) Au_2-C_2O_4(Pc) (c) Au_2-C_2O_4(PP)

(d) (e) (f)

(g) Au_{str}-C_2O_4(NN) (h)

Figure 3.27. *Computed structures for Au-$C_2O_4^{2-}$. (a)-(c) NP, Pc and PP configurations for Au_2-C_2O_4 complexes and (d)-(f) corresponding electron density difference plots. (g) Structure and (h) electron density difference plot for LL configuration at the edge of Au_{str}(110).*

ble 3.7 should be considered more directional since major convergence issues were encountered when C-C bond was near the true breaking point presenting the formation barrier. Also it has to be noted, that the barriers have been reported using two gas-phase CO_2 molecules as the baseline for the energy, which represents the experimental situation most closely. The formation energies calculated this way range from 0.5 eV to 0.9 eV which are easily surpassed in room temperature. For MgO-C_2O_4(PP) the computed barrier is 0.4 eV which is lower than any of the barriers in the presence of Au. However, in order for this reaction to happen, initially adsorbed CO_2 species in (P) configuration has to desorb first since the C atom is surrounded by O atoms (see Figure 3.20(a)) effectively preventing the C-C bond formation. In Au_x-CO_2 configurations the C atoms are much more exposed making reaction with another CO_2 molecule

much more likely, which is most probably the reason for the catalytic effect of Au islands in C_2O_4 species formation.

3.2.5 Vibration Analysis

Vibration analysis allows direct comparison between the experimental IR absorbance data presented in [1] and DFT calculations. The experimental spectra obtained by infrared reflection absorption spectroscopy (IRAS) technique for CO_2 adsorption on both MgO/Ag and Au/MgO/Ag surfaces are presented in Figure 3.19 and corresponding calculated energies are summarized in Table 3.8. In order to make comparison between experiments and calculations it has to be noted that using IRAS method only vibration modes showing change in polarization perpendicular to the surface are detectable in contrast to DFT calculations revealing all possible vibration modes. In the Table 3.8 the modes which are not be detectable are indicated by red color.

When clean MgO is exposed to CO_2, the IR spectrum shows a single band at 1295 cm^{-1} which is moved to 1275 cm^{-1} and 1259 cm^{-1} with ^{13}C and ^{18}O labeling on CO_2 molecules, respectively (Figure 3.19(a)). If the MgO film is prepared with isotope-labeled oxygen, no change is observed. If $\sim$ 4 % scaling factor is taken into account, this band corresponds well to MgO-CO_2 (P) configuration for which the corresponding calculated vibrational modes are 1247, 1231 and 1206 cm^{-1}. If in turn MgO is isotope-labeled, i.e. the mass of the substrate O atom is set in the calculations to 18 u, the vibration band is at 1244 cm^{-1}, which is very close to the unlabeled system and therefore in agreement with the experimental findings. Calaza *et al.* speculate in [1] that the 1295 cm^{-1} band would result from the formation of carboxylate species, i.e. CO_2 lying on some point defect, like F^+ -center (oxygen vacancy), or on metal ion. The carbonate formation, i.e. CO_2 adsorbed on top of lattice oxygen (MgO-CO_2 (P) configuration) is ruled out by the fact that the absorbance band does not shift when MgO is oxygen-labeled. However, as the calculations demonstrate, ^{16}O or ^{18}O labeling on MgO does not show difference on the vibration energy for this particular band and therefore the MgO-CO_2 (P) adsorption configuration is in line with the 1295 cm^{-1} band. The reason for this is that in this vibration mode the lattice oxygen atom is stationary while the molecular C-O bonds vibrate symmetrically. Also, CO_2 on top of Mg can be ruled out since no such stable adsorption configuration was found.

Figure 3.19(b) shows the IR spectra for CO_2 dosed on Au/MgO/Ag surface. As can be seen, in addition to the 1295 cm^{-1} band expressed by CO_2

Table 3.8. Harmonic eigenmodes of CO_2 and C_2O_4 species on MgO film and on different Au/MgO systems (Au_1, Au_2 and $Au_{str}(110)$). Only the relevant vibration energies ω within the experimental range are presented. All values are in cm^{-1}. The numbers in red italics refer to eigenmodes not showing change in polarization perpendicular to the surface indicating that they would not be detectable by the experiments.

	CO_2		$AuCO_2$	Au_2CO_2	C_2O_4		$Au_2C_2O_4$		$Au(110)C_2O_4$			
	(P)	**Exp.**	(N)	(N)	(NP1)	(NP2)	(NP)	(Pc)	(NN)	(Pc)	(PP)	**Exp.**
$^{12}C^{16}O_2$	1247	**1295**	1231	1197	1226	1245	1261	1228	*1294*	1196	*1304*	**1220**
					1365	1406	1350	1414	1345	1391	*1380*	**1398**
$^{13}C^{16}O_2$	1231	**1275**		1181				1207	*1273*	1169	*1282*	**1220**
								1404	1319	1355	*1351*	**1360**
$^{12}C^{18}O_2$	1206	**1259**		1146				1191	*1253*	1163	*1263*	**1210**
								1393	1310	1367	*1346*	**1374**

adsorbed on clean MgO, two additional peaks are observed at 1220 cm^{-1} and 1398 cm^{-1}. These two peaks are assigned to oxalate species [1]. Comparing these bands with the vibration eigenmodes computed for several $AuCO_2$ and AuC_2O_4 complexes (Table 3.8) provides strong support for this conclusion. All C_2O_4 systems have a vibration eigenmode with an energy $\sim$ 1400 cm^{-1} while CO_2 complexes are missing this eigenenergy. Additionally, AuC_2O_4 (Pc) configurations express $1200 - 1220$ cm^{-1} vibration mode and especially at the Au(110) edge vibration energies of 1196 cm^{-1} and 1391 cm^{-1} are very close to the experimental values. At this configuration the IR signals would also be strong due to the mainly surface normal vibrational components. The visualization of these two modes reveal that the higher frequency mode has mainly C-C stretching character while the other mode consists of C-O-C angle deformation and C-O bond stretching. The 1220 cm^{-1} band is also consistent with $AuCO_2$ (N) configurations which indicates that part of the molecules may be adsorbed at the edge of Au islands without forming oxalate. However, the presence of the higher frequency band suggests that oxalate is present.

The computed vibration eigenergies for ^{13}C and ^{18}O labeled systems are in line with the experimental results when $Au(110)C_2O_4$ (Pc) configuration is considered. Especially the shifts in the 1391 cm^{-1} eigenmode are within few wave numbers. The DFT calculations predict a $\sim$ 30 cm^{-1} shift for the lower 1220 cm^{-1} mode upon labeling while in the experiments the corresponding band shifts by $\sim$ 10 cm^{-1} when CO_2 is oxygen-labeled. On the other hand, the vibration energies for both $AuCO_2$ (N) and $MgO-CO_2$ (P) are also very close

to 1220 cm^{-1} frequency which would indicate that the 1220 cm^{-1} band may be mainly originated from unreacted CO_2 atoms at the edges of the Au islands and on MgO.

4 Summary and Outlook

CLC materials

Here I have studied and presented the results for reduction of copper and manganese oxides by utilizing GGA+U calculations. The reduction process was characterized by calculating oxygen vacancy formation energies and anion diffusion barriers in bulk and at the vicinity of corresponding most stable surfaces. Energetically most favorable surface vacancy has always lower formation energy compared to bulk material which favors particles having high surface to bulk ratio. Diffusion is not expected to be the rate determining step in the reduction process since the barrier is within the studied materials lower than the oxygen deficiency energy especially taking into account the known underestimation of vacancy formation energies.

Atomistic thermodynamics analysis reveals that $Mn_2O_3(110)$ is readily reduced into Mn_3O_4 at relatively low temperatures. $Mn_3O_4(001)$ is able to reduce further but pure Mn phase is formed only at very high temperatures. In contrast to Mn_2O_3, CuO(111) surface is not able to reduce at relevant conditions under vacuum annealing conditions. Therefore the reduction process is likely dependent on additional adsorbed reducing agents, such as fuel molecules. $Cu_2O(111)$ does not have same kind of restrictions. After a $\Theta = \frac{1}{8}$ vacancy has been made at Cu_2O the surface forms local Cu phase which are potentially catalytically active and therefore undesirable.

Straining is often introduced to the structure by e.g. the interfaces between nanoparticles and the support material or between dissimilar oxides. This kind of straining plays an important role on the oxygen transport for which reason the O migration was also studied in the strained conditions. In oxygen-rich oxides Mn_2O_3 and CuO the diffusion barrier decreases steadily as the function of applied tensile strain until reaches close to 0 eV at 6 % strain. This behavior is contrary to Mn_3O_4 FP, where the barrier increases correspondingly. In Cu_2O the diffusion energy first increases until decreases dramatically at > 4 % strain. The unusual behavior of the Mn_3O_4 and Cu_2O FPs are accounted to

geometrical frustrations induced by the migrating oxygen at TS. For Mn_3O_4 it was found that at $\sim$ 5 % strain EP_1 path becomes more favorable than FP due to increased space for oxygen to penetrate Mn-Mn edge. For Cu_2O EP path is hindered mainly by the unfavorable interstitial tetragonal binding site at higher strains. These studies demonstrate that it is important to consider all the viable paths when diffusion inside the material is studied especially in strained conditions.

There would be several paths to extend the computational studies of CLC materials from these results. The oxides chosen in this work could be studied more comprehensively, e.g. by studying the effect of multiple oxygen vacancies and the transformation of corresponding surface from the oxidized form to the reduced one more closely. This could reveal the possible restrictions of oxidation/reduction processes. Obviously the results could be compared with other materials. Direct comparison with OC materials performing poorly in experiments could reveal the most important computable factors affecting to the actual oxygen carrying performance. Whether the oxygen migration, vacancy formation energy, or combination of these or some other factors, is the most determining factor remains to be seen. It would be also interesting to study the possible performance enhancements going from the conventional bulk materials, which basically have been studied in this work, to nano-sized OC materials, which could have superior oxygen transport properties due to the increased surface-to-bulk ratio. Also the range of OC materials could be extended with several mixed/doped oxides since introduction of impurities like Ni, Ce and Fe has shown widely varying performance of OC particles in CLC reaction [26, 156, 157, 158, 159]. All of these aspects could be studied using *ab initio* DFT calculations, which therefore have great potential to achieve better understanding of the performance variations amongst different materials. Ultimately more efficient materials for CLC process could be designed systematically by the means of *ab initio* methods.

CO_2 adsorption and C_2O_4 formation on Au/MgO/Ag surface

The adsorption of CO_2 molecule and C_2O_4 formation at MgO(001)/Ag(001) and at the edge of Au islands on top of MgO/Ag was studied using several different models for the surface. The results were also compared with the experimental findings for corresponding system presented in [1]. In this section

I demonstrated that the adsorption of CO_2 is enhanced at the edges of ad-Au clusters compared to the clean MgO/Ag surface. However, the adsorption energy varies depending on the size of the gold cluster and Au_2CO_2 complex is found the most favorable. The relative Lewis acidity of Au_1 and Au_2 on MgO explain the differences in the CO_2 adsorption energetics on these systems. Larger Au clusters form a continuous DOS bands allowing the determination of *d*-band centers, which correlate linearly with the CO_2 adsorption energies. It was also found that MgO$-CO_2$ (P) adsorption is more favorable when ad-Au is not present on MgO which is explained by the relative Lewis acidities of the adsorption centers. This indicates that when Au is present, single CO_2 molecules are in contact with Au instead of adsorbing only at the vicinity of Au clusters.

The formation energy of C_2O_4 species on the surface was not found to be more favorable at the edges of Au clusters. The computed reaction barriers ranged from 0.4 eV to 0.9 eV in relative to two gas phase CO_2 molecules. However, carbon in CO_2 is sterically restricted in MgO$-CO_2$(P) configuration to react with another CO_2 molecule making the formation of oxalate products unlikely. At $AuCO_2$ complexes the C atom is much more exposed allowing C-C bond forming. This is likely the explanation for the catalytic effect of ad-Au clusters in oxalate forming reaction observed in the experiments. Vibration analysis provided strong support that the IR bands observed in the experiments are indeed originated from oxalate species. The computational results presented in this thesis suggest that the thin MgO(001)/Ag(001) film shuttles electrons to nanoscale Au islands which provide a favorable adsorption site for CO_2 molecules. These carbon dioxide molecules are able to react with another CO_2 molecule to form oxalate species. This is in agreement with experimental results presented in [1].

The results presented here could be appended by e.g. studying the nature of reaction with two CO_2 molecules to form oxalate more comprehensively. Also the coverage effects of different adsorbates were left outside of the study in this work. The experimental results of 0.02 ML coverage of CO_2 on clean MgO and ~ 15 adsorbed oxalate species per one $4-5$ nm Au island could be confirmed by DFT calculations. Also one interesting way to extend the results would be to study the reactions of ${C_2O_4}^{2-}$ species further.

In summary for this thesis as a whole, the work presented here has contributed to the knowledge of oxygen carrying materials in chemical looping combustion process as well as the CO_2 activation on thin film Au clusters. Two CLC materials have been characterized computationally and the obtained

results can be used in developing an *ab initio* scheme for predicting the oxygen carrying properties of OC particles. This would eventually help to find the best possible materials to be used in CLC reactors. In the second part of this thesis I provided strong support for the experimental results suggesting that Au/MgO(001)/Ag(001) surface has potential to activate CO_2 molecules such that oxalate species, ${C_2O_4}^{2-}$, are formed. This kind of novel heterogenic catalysis used in combination with e.g. CLC reactors may prove to be important ways to reduce the CO_2 concentration in the atmosphere, which would be ultimately needed to stop the emerging global climate change.

Bibliography

[1] Florencia Calaza, Christian Stiehler, Yuichi Fujimori, Martin Sterrer, Sebastian Beeg, Miguel Ruiz-Oses, Niklas Nilius, Markus Heyde, Teemu Parviainen, Karoliina Honkala, Hannu Häkkinen, and Hans-Joachim Freund. Carbon Dioxide Activation and Reaction Induced by Electron Transfer at an Oxide-Metal Interface. *Angew. Chemie Int. Ed.*, 54(42):12484–12487, 2015.

[2] IPCC 2014. Climate Change 2014: Synthesis Report. Contribution of Working Groups I, II and III to the Fifth Assessment Report of the Intergovernmental Panel on Climate Change [Core Writing Team, R.K. Pachauri and L.A. Meyer (eds.)]. Technical report, IPCC, Geneva, Switzerland, 2014.

[3] V. Bex Contribution of Working Group I to the Fifth Assessment Report of the Intergovernmental Panel on Climate Change [Stocker, T.F., D. Qin, G.-K. Plattner, M. Tignor, S.K. Allen, J. Boschung, A. Nauels, Y. Xia and P.M. Midgley (eds.)]. Climate Change 2013: The Physical Science Basis. Technical report, Cambridge University Press, Cambridge, United Kingdom and New York, NY, USA, 2013.

[4] IPCC, Bert Metz, Ogunlade Davidson, Heleen de Coninck, Manuela Loos, and Leo Meyer. Special Report: Carbon dioxide capture and storage. Technical report, Intergovernmental Panel on Climate Change, Cambridge, New York, Melbourne, Madrid, Cape Town, Singapore, Sao Paolo, 2005.

[5] Michele Aresta, editor. *Carbon Dioxide Recovery and Utilization.* Springer Netherlands, 1 edition, 2003.

[6] T. Zwickel IPCC 2014: Contribution of Working Group III to the Fifth Assessment Report of the Intergovernmental Panel on Climate Change [Edenhofer, O., R. Pichs-Madruga, Y. Sokona, E. Farahani, S. Kadner, K. Seyboth, A. Adler, I. Baum, S. Brunner, P. Eickemeier, B. and J.C. Minx

(eds.)]. *Climate Change 2014, Mitigation of Climate Change. Contribution of Working Group III to the Fifth Assessment Report of the Intergovernmental Panel on Climate Change*. Cambridge University Press, Cambridge, United Kingdom and New York, NY, USA, 2014.

[7] R.E.H. Sims, R.N. Schock, A. Adegbululgbe, J. Fenhann, I. Konstantinaviciute, W. Moomaw, H.B. Nimir, B. Schlamadinger, J. Torres-Martínez, C. Turner, Y. Uchiyama, S.J.V. Vuori, N. Wamukonya, X. Zhang, I Konstantinaviciute, W Moomaw, H B Nimir, B Schlamadinger, C Turner, Y Uchiyama, S J V Vuori, N Wamukonya, and X Zhang. Climate Change 2007: Mitigation. Contribution of Working Group III to the Fourth Assessment Report of the Intergovernmental Panel on Climate Change Mitigation. Contribution of Working Group III to the Fourth Assessment Report of the Intergovernmental Pane. Technical report, International Panel on Climate Change, Cambridge, United Kingdom and New York, NY, USA, 2007.

[8] H. R. Kerr. Capture and separation technology gaps and priority research needs. In David C. Thomas, editor, *Carbon Dioxide Capture Storage Deep Geol. Form. - Results from CO_2 Capture Proj. Capture Sep. Carbon Dioxide from Combust. Sources*, chapter 38. 2005.

[9] Tobias Mattisson, Anders Lyngfelt, and Henrik Leion. Chemical-looping with oxygen uncoupling for combustion of solid fuels. *Int. J. Greenh. Gas Control*, 3(1):11–19, jan 2009.

[10] Wu Qin, Qiuluan Chen, Yang Wang, Changqing Dong, Junjiao Zhang, Wenyan Li, and Yongping Yang. Theoretical study of oxidation-reduction reaction of Fe_2O_3 supported on MgO during chemical looping combustion. *Appl. Surf. Sci.*, 266:350–354, feb 2013.

[11] Paul Cho, Tobias Mattisson, and Anders Lyngfelt. Carbon Formation on Nickel and Iron Oxide-Containing Oxygen Carriers for Chemical-Looping Combustion. *Ind. & Eng. Chem. Res.*, 44(4):668–676, feb 2005.

[12] Saurabh Bhavsar, Brian Tackett, and Götz Veser. Evaluation of iron- and manganese-based mono- and mixed-metallic oxygen carriers for chemical looping combustion. *Fuel*, 136(x):268–279, nov 2014.

[13] Qamar Zafar, Alberto Abad, Tobias Mattisson, Börje Gevert, and Michael Strand. Reduction and oxidation kinetics of Mn_3O_4/Mg-ZrO_2 oxygen carrier particles for chemical-looping combustion. *Chem. Eng. Sci.*, 62(23):6556–6567, dec 2007.

[14] Yan Cao, Bianca Casenas, and Wei-ping Pan. Investigation of Chemical Looping Combustion by Solid Fuels . 2 . Redox Reaction Kinetics and Product Characterization with Coal , Biomass , and Solid Waste as Solid Fuels and CuO as an Oxygen Carrier. *Energy & Fuels*, 20(5):1845–1854, 2006.

[15] Iñaki Adánez-Rubio, Alberto Abad, Pilar Gayán, Luis F. de Diego, Francisco García-Labiano, and Juan Adánez. Identification of operational regions in the Chemical-Looping with Oxygen Uncoupling (CLOU) process with a Cu-based oxygen carrier. *Fuel*, 102:634–645, dec 2012.

[16] Paul Cho, Tobias Mattisson, and Anders Lyngfelt. Comparison of iron-, nickel-, copper- and manganese-based oxygen carriers for chemical-looping combustion. *Fuel*, 83(9):1215–1225, jun 2004.

[17] Marcus Johansson. *Screening of oxygen-carrier particles based on iron- , manganese- , copper- and nickel oxides for use in chemical-looping technologies*. PhD thesis, Chalmers University of Technology, 2007.

[18] Kaisa Aho. *Use of nanostructures as oxygen carriers in chemical looping combustion*. Pro gradu, University of Jyväskylä, 2013.

[19] N Khare. *Handbook of High-Temperature Superconductor*. Applied Physics. Taylor & Francis, 2003.

[20] Leah Isseroff Bendavid and Emily a Carter. First-Principles Predictions of the Structure, Stability, and Photocatalytic Potential of Cu_2O Surfaces. *J. Phys. Chem. B*, 117(49):15750–60, dec 2013.

[21] Suwit Suthirakun, Salai Cheettu Ammal, Guoliang Xiao, Fanglin Chen, Hans-Conrad zur Loye, and Andreas Heyden. Density functional theory study on the electronic structure of n- and p-type doped $SrTiO_3$ at anodic solid oxide fuel cell conditions. *Phys. Rev. B*, 84(20):205102, nov 2011.

[22] Hai-Yan Su, Yelena Gorlin, Isabela C Man, Federico Calle-Vallejo, Jens K Nørskov, Thomas F Jaramillo, and Jan Rossmeisl. Identifying active surface phases for metal oxide electrocatalysts: a study of manganese oxide bi-functional catalysts for oxygen reduction and water oxidation catalysis. *Phys. Chem. Chem. Phys.*, 14(40):14010–14022, oct 2012.

[23] Tobias Mattisson and Anders Ja. Reactivity of Some Metal Oxides Supported on Alumina with Alternating Methane and Oxygen s Application for Chemical-Looping Combustion. *Energy & Fuels*, 17(4):643–651, 2003.

[24] J Adánez, L.F. de Diego, F. García-Labiano, P. Gayán, A Abad, L F De Diego, P. Gayán, A Abad, J M Palacios, P Gaya, A Abad, and Miguel Luesma Casta. Selection of Oxygen Carriers for Chemical-Looping Combustion. *Energy & Fuels*, 18(3):371–377, 2004.

[25] Qamar Zafar and Tobias Mattisson. Redox Investigation of Some Oxides of Transition-State Metals Ni, Cu, Fe, and Mn Supported on SiO_2 and $MgAl_2O_4$. *Energy & Fuels*, 20(6):34–44, 2006.

[26] Alexander Shulman, Erik Cleverstam, Tobias Mattisson, and Anders Lyngfelt. Manganese/Iron, Manganese/Nickel, and Manganese/Silicon Oxides Used in Chemical-Looping With Oxygen Uncoupling (CLOU) for Combustion of Methane. *Energy & Fuels*, 23(10):5269–5275, oct 2009.

[27] Juan Adanez, Alberto Abad, Francisco Garcia-Labiano, Pilar Gayan, and Luis F. de Diego. Progress in Chemical-Looping Combustion and Reforming technologies. *Prog. Energy Combust. Sci.*, 38(2):215–282, apr 2012.

[28] Pilar Gayán, Iñaki Adánez-Rubio, Alberto Abad, Luis F. de Diego, Francisco García-Labiano, and Juan Adánez. Development of Cu-based oxygen carriers for Chemical-Looping with Oxygen Uncoupling (CLOU) process. *Fuel*, 96:226–238, jun 2012.

[29] Luis F. De Diego, Francisco García-Labiano, Juan Adánez, Pilar Gayán, Alberto Abad, Beatriz M. Corbella, and Jose María Palacios. Development of Cu-based oxygen carriers for chemical-looping combustion. *Fuel*, 83(13):1749–1757, 2004.

[30] Bilge Yildiz. "Stretching" the energy landscape of oxides-Effects on electrocatalysis and diffusion. *MRS Bull.*, 39(02):147–156, feb 2014.

[31] Akihiro Kushima and Bilge Yildiz. Oxygen ion diffusivity in strained yttria stabilized zirconia: where is the fastest strain? *J. Mater. Chem.*, 20(23):4809, 2010.

[32] John a Kilner. Ionic conductors: feel the strain. *Nat. Mater.*, 7(11):838–839, 2008.

[33] C. Korte, A. Peters, J. Janek, D. Hesse, and N. Zakharov. Ionic conductivity and activation energy for oxygen ion transport in superlattices - The multilayer system CSZ (ZrO_2 + CaO) / Al_2O_3. *Solid State Ionics*, 10:4623–4635, 2008.

[34] J. a. Hirschfeld and H. Lustfeld. First-principles study and modeling of strain-dependent ionic migration in ZrO_2. *Phys. Rev. B*, 84(22):224308, dec 2011.

[35] S. M. Benson. Carbon Dioxide Capture and Storage: Assessment of Risks from Storage of Carbon Dioxide in Deep Underground Geological Formations. Technical report, Lawrence Berkeley National Laboratory, 2006.

[36] Sheri Gagnon. Burying the Problem. *Can. Geogr.*, 2008.

[37] Parsons Brinckerhoff. Accelerating the Uptake of Ccs : Industrial Use of Captured Carbon Dioxide. Technical Report March, Global CCS Institute, 2011.

[38] Jos G.J. Olivier, Greet Janssens-Maenhout, Marilena Muntaean, and Jeroen A.H.W Peters. Trends in global CO_2 emissions 2014 Report. Technical report, PBL Netherlands Environmental Assessment Agency, The Hague, 2014.

[39] Chunshan Song. Global challenges and strategies for control, conversion and utilization of CO_2 for sustainable development involving energy, catalysis, adsorption and chemical processing. *Catal. Today*, 115(1-4):2–32, 2006.

[40] Wei Wang, Shengping Wang, Xinbin Ma, and Jinlong Gong. Recent advances in catalytic hydrogenation of carbon dioxide. *Chem. Soc. Rev.*, 40(7):3703–3727, 2011.

[41] Samrand Saeidi, Nor Aishah Saidina Amin, and Mohammad Reza Rahimpour. Hydrogenation of CO_2 to value-added products - A review and potential future developments. *J. CO2 Util.*, 5:66–81, 2014.

[42] Gerhard Lauermann, Peter Häussinger, Reiner Lohmüller, and Allan M. Watson. *Hydrogen, 1. Properties and Occurence*, chapter Hydrogen„ pages 1–15. Wiley-VCH Verlag GmbH GmbH & Co KGaA, 2000.

[43] Kai Zeng and Dongke Zhang. Recent progress in alkaline water electrolysis for hydrogen production and applications. *Prog. Energy Combust. Sci.*, 36(3):307–326, 2010.

[44] Detlef Schröder, Christoph a Schalley, Jeremy N Harvey, and Helmut Schwarz. On the formation of the carbon dioxide anion radical CO_2^- in the gas phase. *Int. J. Mass Spectrom.*, 185-187:25–35, 1999.

[45] Edward L Quitevis and Dudley R Herschbach. Electron Attachment to CO, Clusters by Collisional Charge Transfer. *J. Phys. Chem.*, 93(3):1136–1139, 1989.

[46] Janina a. Rosso, Sonia G. Bertolotti, André M. Braun, Daniel O. Mártire, and Monica C. Gonzalez. Reactions of carbon dioxide radical anion with substituted benzenes. *J. Phys. Org. Chem.*, 14(5):300–309, 2001.

[47] Johannes Postler, Violaine Vizcaino, Stephan Denifl, Fabio Zappa, Stefan Ralser, Matthias Daxner, Eugen Illenberger, and Paul Scheier. Electron Attachment to CO_2 Embedded in Superfluid He Droplets. *J. Phys. Chem. A*, 118:6553–6559, 2014.

[48] John Berman, Helen M. and Westbrook, Zukang Feng, Gary Gilliland, T. N. Bhat, Helge Weissig, Ilya N. Shindyalov, and Philip E. Bourne. The Protein Data Bank: Rubisco. *Nucleic Acids Res.*, 28(1):235–242, 1999.

[49] Yasuo Fukuda and Isamu Toyoshima. AES and UPS studies of CO and CO_2 adsorption on Mg and MgO. *Surf. Sci.*, 158(1-3):482–489, jul 1985.

[50] H-J Freund and Meirion Wynn Roberts. Surface chemistry of carbon dioxide. *Surf. Sci. Rep.*, 25(8):225–273, 1996.

[51] Gargi Dutta, Alexey A Sokol, C Richard A Catlow, Thomas W Keal, and Paul Sherwood. Activation of Carbon Dioxide over Zinc Oxide by Localised Electrons. *ChemPhysChem*, 13(15):3453–3456, 2012.

[52] Yoshitake Toda, Hiroyuki Hirayama, Navaratnarajah Kuganathan, Antonio Torrisi, Peter V Sushko, and Hideo Hosono. Activation and splitting of carbon dioxide on the surface of an inorganic electride material. *Nat. Commun.*, 4(2378), aug 2013.

[53] Geoffrey C Bond, Paul A Sermon, Geoffrey Webb, Douglas A Buchanan, and Peter B Wells. Hydrogenation over supported gold catalysts. *J. Chem. Soc. Chem. Commun.*, 13:444b–445, 1973.

[54] Masatake Haruta. Size- and support-dependency in the catalysis of gold. *Catal. Today*, 36(1):153–166, 1997.

[55] Thomas Risse, Shamil Shaikhutdinov, Niklas Nilius, Martin Sterrer, and Hans Joachim Freund. Gold supported on thin oxide films: From single atoms to nanoparticles. *Acc. Chem. Res.*, 41(8):949–956, 2008.

[56] a Stephen K Hashmi and Graham J Hutchings. Gold catalysis. *Angew. Chem. Int. Ed. Engl.*, 45(47):7896–7936, 2006.

[57] Vahideh Habibpour. *Reactivity of Cluster Model Catalysts : Influence of Support Material Properties and Reaction Conditions*. Academic dissertation, Technische Universität München, 2009.

[58] Katayun Barmak and Kevin Coffey. 8 - Metallic thin films: stresses and mechanical properties. In Katayun Barmak and Kevin B T Metallic Films for Electronic Coffey Optical and Magnetic Applications, editors, *Met. Film. Electron. Opt. Magn. Appl. Struct. Process. Prop.*, chapter 8, pages 353–421. Woodhead Publishing, 2014.

[59] J Wollschläger, J. Viernow, C. Tegenkamp, D Erdös, K.M. Schröder, and H Pfnür. Stoichiometry and morphology of MgO films grown reactively on Ag(100). *Appl. Surf. Sci.*, 142(1-4):129–134, 1999.

[60] Martin Sterrer, Markus Heyde, Marek Novicki, Niklas Nilius, Thomas Risse, Hans Peter Rust, Gianfranco Pacchioni, and Hans Joachim Freund. Identification of color centers on MgO(001) thin films with scanning tunneling microscopy. *J. Phys. Chem. B*, 110(1):46–49, 2006.

[61] R.G. Parr and W Yang. Density-functional theory of atoms and molecules. *Int. Ser. Monogr. Chem.*, page 323, 1989.

[62] P Hohenberg and W Kohn. Inhomogeneous electron gas. *Phys. Rev. B*, 136(3B):864–871, 1964.

[63] W Kohn and L. J. Sham. Self-Consistent Equations Including Exchange and Correlation Effects. *Phys. Rev.*, 140(4A):1133–1138, 1965.

[64] D. M. Ceperley and B. J. Alder. Ground state of the electron gas by a stochastic method. *Phys. Rev. Lett.*, 45(7):566–569, 1980.

[65] R Q Hood, M Y Chou, a J Williamson, G Rajagopal, R J Needs, and W M C Foulkes. Quantum Monte Carlo investigation of exchange and correlation in silicon. *Phys. Rev. Lett.*, 78(17):3350–3353, 1997.

[66] M C Payne, M P Teter, D C Allan, T a Arias, and J D Joannopoulos. Iterative minimization techniques for ab initio total -energy calculations: molecular dynamics and conjugate gradients. *Rev. Mod. Phys.*, 64(4):1045–1097, 1992.

[67] O. Gunnarsson and B. I. Lundqvist. Exchange and correlation in atoms, molecules, and solids by the spin-density-functional formalism. *Phys. Rev. B*, 13(10):4274–4298, 1976.

[68] John P. Perdew, Kieron Burke, and Matthias Ernzerhof. Generalized Gradient Approximation Made Simple. *Phys. Rev. Lett.*, 77(18):3865–3868, oct 1996.

[69] John Perdew, J. Chevary, S. Vosko, Koblar Jackson, Mark Pederson, D. Singh, and Carlos Fiolhais. Atoms, molecules, solids, and surfaces: Applications of the generalized gradient approximation for exchange and correlation. *Phys. Rev. B*, 46(11):6671–6687, 1992.

[70] John P Perdew, P Ziesche, and H Eschrig. *Electronic structure of solids*, volume 11. Akademie Verlag, Berlin, 1991.

[71] Viktor Staroverov, Gustavo Scuseria, Jianmin Tao, and John Perdew. Tests of a ladder of density functionals for bulk solids and surfaces. *Phys. Rev. B*, 69(7):1–11, 2004.

[72] Laurids Schimka, Judith Harl, and Georg Kresse. Improved hybrid functional for solids: The HSEsol functional. *J. Chem. Phys.*, 134(024116), 2011.

[73] C. David Sherrill. Frontiers in electronic structure theory. *J. Chem. Phys.*, 132(110902):0–7, 2010.

[74] Jess Wellendorff, Keld T. Lundgaard, Andreas Møgelhøj, Vivien Petzold, David D. Landis, Jens K. Nørskov, Thomas Bligaard, and Karsten W. Jacobsen. Density functionals for surface science: Exchange-correlation model development with Bayesian error estimation. *Phys. Rev. B - Condens. Matter Mater. Phys.*, 85(235149), 2012.

[75] Kyuho Lee, Éamonn D. Murray, Lingzhu Kong, Bengt I. Lundqvist, and David C. Langreth. A Higher-Accuracy van der Waals Density Functional. *Phys. Rev. B*, 82(081101):14, 2010.

[76] Lei Wang, Thomas Maxisch, and Gerbrand Ceder. Oxidation energies of transition metal oxides within the GGA+U framework. *Phys. Rev. B*, 73(195107), may 2006.

[77] Vladimir I Anisimov, F Aryasetiawan, and Ai Liechtenstein. First-principles calculations of the electronic structure and spectra of strongly correlated systems: the LDA + U method. *J. Phys. Condens. Matter*, 9(4):767–808, 1997.

[78] Anubhav Jain, Geoffroy Hautier, Shyue Ping Ong, Charles J. Moore, Christopher C. Fischer, Kristin a. Persson, and Gerbrand Ceder. Forma-

tion enthalpies by mixing GGA and GGA + U calculations. *Phys. Rev. B*, 84(4):045115, jul 2011.

[79] F. Zhou, M. Cococcioni, C. a. Marianetti, D. Morgan, and G. Ceder. First-principles prediction of redox potentials in transition-metal compounds with LDA + U. *Phys. Rev. B - Condens. Matter Mater. Phys.*, 70(23):1–8, 2004.

[80] C. Franchini, R. Podloucky, J. Paier, M. Marsman, and G. Kresse. Ground-state properties of multivalent manganese oxides: Density functional and hybrid density functional calculations. *Phys. Rev. B*, 75(19):195128, may 2007.

[81] R. M. Martin. *Electronic structure - Basic theory and practical methods*. Cambridge university press, UK, 2008.

[82] James R. Chelikowsky, N. Troullier, K. Wu, and Y. Saad. Higher-order finite-difference pseudopotential method: An application to diatomic molecules. *Phys. Rev. B*, 50(16):11355–11364, 1994.

[83] Carlos L Reis, J M Pacheco, and José Luis Martins. First-principles norm-conserving pseudopotential with explicit incorporation of semicore states Â´. *Phys. Rev. B*, 68(155111):1–6, 2003.

[84] N. Troullier and José Luis Martins. Efficient pseudopotentials for plane-wave calculations. *Phys. Rev. B*, 43(3):1993–2006, 1991.

[85] Carsten Rostgaard. The Projector Augmented-wave Method, 2010.

[86] P. E. Blöchl. Projector augmented-wave method. *Phys. Rev. B*, 50(24):17953–17979, 1994.

[87] Jutta Rogal and Karsten Reuter. Ab Initio Atomistic Thermodynamics for Surfaces : A Primer. *Exp. Model. Simul. Gas- Surf. Interact. React. Flows Hypersonic Flights*, pages 1–18, 2007.

[88] Michael A. Collins. The Interface Between Electronic Structure Theory and Reaction Dynamics by Reaction Path Methods. *Adv. Chem. Phys.*, 93:389–453, 2007.

[89] Edward Sanville, Steven D Kenny, Roger Smith, and Graeme Henkelman. Improved grid-based algorithm for Bader charge allocation. *J. Comput. Chem.*, 28(5):899–908, 2007.

[90] Graeme Henkelman, Andri Arnaldsson, and Hannes Jónsson. A fast and robust algorithm for Bader decomposition of charge density. *Comput. Mater. Sci.*, 36(3):354–360, 2006.

[91] J W Niemantsverdriet. *Concepts of Modern Catalysis and Kinetics*. WILEY-VCH Verlag GmbH GmbH & Co. KGaA, 2003.

[92] J. Mortensen, L. Hansen, and K. Jacobsen. Real-space grid implementation of the projector augmented wave method. *Phys. Rev. B*, 71(3):035109, jan 2005.

[93] Sune R. Bahn and Karsten W. Jacobsen. An Object-Oriented Scripting Interface to a Legacy Electronic Structure Code. *Comput. Sci. Eng.*, May/June:56–66, 2002.

[94] K T Jacob, A Kumar, G Rajitha, and Y Waseda. Thermodynamic Data for Mn3O4, Mn_2O_3 and MnO_2. *High Temp. Mater. Proc.*, 30:459–472, 2011.

[95] Subhash Thota, Bhagwati Prasad, and Jitendra Kumar. Formation and magnetic behaviour of manganese oxide nanoparticles. *Mater. Sci. Eng. B*, 167(3):153–160, mar 2010.

[96] S Geller. Structure of α-Mn_2O_3, $(Mn_{0.983}Fe_{0.017})_2O_3$ and $(Mn_{0.37}Fe_{0.63})_2O_3$ and relation to magnetic ordering. *Acta Crystallogr. Sect. B Struct. Crystallogr. Cryst. Chem.*, 27(4):821–828, apr 1971.

[97] M Regulski, R Przenioslo, I Sosnowska, D Hohlwein, and R Schneider. Neutron diffraction study of the magnetic structure of α-Mn_2O_3. *J. Alloys Compd.*, 362(1-2):236–240, jan 2004.

[98] Eric Cockayne, Igor Levin, Hui Wu, and Anna Llobet. Magnetic structure of bixbyite α-Mn_2O_3: A combined DFT+U and neutron diffraction study. *Phys. Rev. B*, 87(184413), may 2013.

[99] M Busch, E Ahlberg, and I Panas. Electrocatalytic oxygen evolution from water on a Mn(III-V) dimer model catalyst–a DFT perspective. *Phys. Chem. Chem. Phys.*, 13(33):15069–15076, sep 2011.

[100] P A Korzhavyi and B Johansson. Literature review on the properties of cuprous oxide Cu_2O and the process of copper oxidation. Technical Report October, Department of Materials Science and Engineering, 2011.

[101] R. Restori and D. Schwarzenbach. Charge Density in Cuprite , Cu_20. *Acta Crystallogr. Sect. B Struct. Crystallogr. Cryst. Chem.*, B42:201–208, 1986.

[102] Chinping Chen, Lin He, Lin Lai, Hua Zhang, Jing Lu, Lin Guo, and Yadong Li. Magnetic properties of undoped Cu_2O fine powders with magnetic impurities and/or cation vacancies. *J. Phys. Condens. Matter*, 21(14):145601, 2009.

[103] G Tunell, E Posniak, and C J Ksanda. Geometrical and optical properties, and crystal structure of tenorite, Zeitschrift für Kristallographie. *Z. Krist.*, 90:120–142, 1935.

[104] T Kimura, Y Sekio, H Nakamura, T Siegrist, and a P Ramirez. Cupric oxide as an induced-multiferroic with high-TC. *Nat. Mater.*, 7(4):291–294, apr 2008.

[105] V. T. Witusiewicz, F. Sommer, and E. J. Mittemeijer. Reevaluation of the Fe-Mn phase diagram. *J. Phase Equilibria Diffus.*, 25(4):346–354, 2004.

[106] G Fuster, N E Brener, J Callaway, J L Fry, Y Z Zhao, and D A Papaconstantopoulos. Magnetism in bcc and fcc manganese. *Phys. Rev. B*, 38(1):423–432, jul 1988.

[107] A. J Bradley and J Thewlis. The Crystal Structure of α-Manganese. *Proc. R. Soc. A Math. Phys. Eng. Sci.*, 115(771):456–471, jul 1927.

[108] J. Hafner and D. Hobbs. Understanding the complex metallic element Mn. II. Geometric frustration in β-Mn, phase stability, and phase transitions. *Phys. Rev. B*, 68(1):014408, jul 2003.

[109] G. Milss and H. Jónsson. Quantum and Thermal Effects in H_2 Dissociative Adsorption: Evaluation of Free Energy Barriers in Multidimensional Quantum Systems. *Phys. Rev. Lett.*, 72(7):1124–1127, 1994.

[110] X. Lin, N. Nilius, H. J. Freund, M. Walter, P. Frondelius, K. Honkala, and H. Häkkinen. Quantum well states in two-dimensional gold clusters on MgO thin films. *Phys. Rev. Lett.*, 102(206801):1–4, 2009.

[111] Michael Walter, Pentti Frondelius, Karoliina Honkala, and Hannu Häkkinen. Electronic structure of MgO-supported Au clusters: Quantum dots probed by scanning tunneling microscopy. *Phys. Rev. Lett.*, 99(096102):1–4, 2007.

[112] Pentti Frondelius, Hannu Häkkinen, and Karoliina Honkala. Adsorption of gold clusters on metal-supported MgO: Correlation to electron affinity of gold. *Phys. Rev. B*, 76(073406):1–4, 2007.

[113] P Frondelius. *Electronic, structural and chemical properties of gold clusters on ultra-thin oxide films.* Academic dissertation for the degree if doctor of philosophy, University of jyväskylä, 2009.

[114] Thomas Frederiksen, Magnus Paulsson, Mads Brandbyge, and Antti Pekka Jauho. Inelastic transport theory from first principles: Methodology and application to nanoscale devices. *Phys. Rev. B - Condens. Matter Mater. Phys.*, 75(205413):1–22, 2007.

[115] A. Jha, R. Thapa, and K.K. K Chattopadhyay. Structural transformation from Mn_3O_4 nanorods to nanoparticles and band gap tuning via Zn doping. *Mater. Res. Bull.*, 47(3):813–819, mar 2012.

[116] Yasheng Maimaiti, Michael Nolan, and Simon D Elliott. Reduction mechanisms of the CuO(111) surface through surface oxygen vacancy formation and hydrogen adsorption. *Phys. Chem. Chem. Phys.*, pages 3036–3046, jan 2014.

[117] R.W.G. Wykoff. *Crystal Structures.* Interscience Publishers, New York, 1963.

[118] Mazharul M. Islam, Boubakar Diawara, Vincent Maurice, and Philippe Marcus. Bulk and surface properties of Cu_2O: A first-principles investigation. *J. Mol. Struct. THEOCHEM*, 903(1-3):41–48, jun 2009.

[119] A. Werner and H. D Hochheimer. High-pressure x-ray study of Cu_2O and Ag_2O. *Phys. Rev. B*, 25(9):5929–5934, 1982.

[120] Nicholas A. Brincat, Stephen C. Parker, Marco Molinari, Geoffrey C. Allen, and Mark T. Storr. Density functional theory investigation of the layered uranium oxides U_3O_8 and U_2O_5. *Dalt. Trans.*, 44:2613–2622, 2015.

[121] F. Marabelli, G. B. Parravicini, and F. Salghetti-Drioli. Optical gap of CuO. *Phys. Rev. B*, 52(3):1433–1436, 1995.

[122] F. P. Koffyberg. A photoelectrochemical determination of the position of the conduction and valence band edges of p-type CuO. *J. Appl. Phys.*, 53(2):1173, 1982.

[123] Sekhar C. Ray. Preparation of copper oxide thin film by the sol-gel-like dip technique and study of their structural and optical properties. *Sol. Energy Mater. Sol. Cells*, 68(3-4):307–312, 2001.

[124] Leah Y. Isseroff and Emily a. Carter. Importance of reference Hamiltonians containing exact exchange for accurate one-shot GW calculations of Cu_2O. *Phys. Rev. B*, 85(23):235142, jun 2012.

[125] Q Javed, FP Wang, Rafique MY, Toufiq AM, Li QS, H Mahmood, and Khan W. Diameter-controlled synthesis of α-Mn_2O_3 nanorods and nanowires with enhanced surface morphology and optical properties. *Nanotechnology*, 23:415603, 2012.

[126] H. J. Trodahl, a. R H Preston, J. Zhong, B. J. Ruck, N. M. Strickland, C. Mitra, and W. R L Lambrecht. Ferromagnetic redshift of the optical gap in GdN. *Phys. Rev. B - Condens. Matter Mater. Phys.*, 76(085211):1–5, 2007.

[127] B. X. Yang, T. R. Thurston, J. M. Tranquada, and G. Shirane. Magnetic neutron scattering study of single-crystal cupric oxide. *Phys. Rev. B*, 39(7):4343–4349, 1989.

[128] David O. Scanlon, Benjamin J. Morgan, and Graeme W. Watson. Modeling the polaronic nature of p-type defects in Cu_2O: The failure of GGA and GGA+U. *J. Chem. Phys.*, 131(12):124703, 2009.

[129] D R Lide. *CRC Handbook of Chemistry and Physics, 86th Edition*. CRC Handbook of Chemistry and Physics, 86th Ed. Taylor & Francis, 2005.

[130] Yuan Peng, Zhen Zhang, Thien Viet Pham, Yang Zhao, Ping Wu, and Junling Wang. Density functional theory analysis of dopants in cupric oxide. *J. Appl. Phys.*, 111(10):103708, 2012.

[131] B. Hammer, L. Hansen, and J. Nørskov. Improved adsorption energetics within density-functional theory using revised Perdew-Burke-Ernzerhof functionals. *Phys. Rev. B*, 59(11):7413–7421, mar 1999.

[132] A. Foster, V. Sulimov, F. Lopez Gejo, A. Shluger, and R. Nieminen. Structure and electrical levels of point defects in monoclinic zirconia. *Phys. Rev. B*, 64(22):224108, nov 2001.

[133] Zongxian Yang, Tom K. Woo, Micael Baudin, and Kersti Hermansson. Atomic and electronic structure of unreduced and reduced CeO_2 surfaces: A first-principles study. *J. Chem. Phys.*, 120(16):7741–7749, 2004.

[134] Asmae Bouzoubaa, Alexis Markovits, Mònica Calatayud, and Christian Minot. Comparison of the reduction of metal oxide surfaces: TiO_2-anatase, TiO_2-rutile and SnO_2-rutile. *Surf. Sci.*, 583(1):107–117, 2005.

[135] Hai-Feng Wang, Hui-Ying Li, Xue-Qing Gong, Yang-Long Guo, Guan-Zhong Lu, and P. Hu. Oxygen vacancy formation in CeO_2 and $Ce_{1-x}Zr_xO_2$ solid solutions: electron localization, electrostatic potential and structural relaxation. *Phys. Chem. Chem. Phys.*, pages 16521–16535, 2012.

[136] Thomas Lippmann and Jochen R. Schneider. Topological analyses of cuprite, Cu_2O, using high-energy synchrotron-radiation data. *Acta Crystallogr. Sect. A Found. Crystallogr.*, 56(6):575–584, nov 2000.

[137] J Carrasco, N Lopez, and F Illas. First Principles Analysis of the Stability and Diffusion of Oxygen Vacancies in Metal Oxides. *Phys. Rev. Lett.*, 93(22):225502, nov 2004.

[138] L E Sutton. *Tables of Interatomic Distances and Configuration in Molecules and Ions : Supplement 1956-59.* Special publication. Chemical Society, 1965.

[139] A Rodriguez, Jae Y Kim, Jonathan C Hanson, and Manuel Pe. Reduction of CuO in H_2 : in situ time-resolved XRD studies. *Catal. Letters*, 85(3-4):247–254, 2003.

[140] Jae Y Kim, A Rodriguez, Jonathan C Hanson, Anatoly I Frenkel, and Peter L Lee. Reduction of CuO and Cu_2O with H_2 : H Embedding and Kinetic Effects in the Formation of Suboxides. *J. Am. Chem. Soc.*, 125:10684–10692, 2003.

[141] M. Verónica Ganduglia-Pirovano, Juarez L.F. Da Silva, and Joachim Sauer. Density-Functional Calculations of the Structure of Near-Surface Oxygen Vacancies and Electron Localization on $CeO_2(111)$. *Phys. Rev. Lett.*, 026101(JANUARY):1–4, 2009.

[142] Gustavo E Murgida and M Verónica Ganduglia-Pirovano. Evidence for Subsurface Ordering of Oxygen Vacancies on the Reduced $CeO_2(111)$ Surface Using Density-Functional and Statistical Calculations. *Phys. Rev. Lett.*, 110(24):246101, jun 2013.

[143] Violeta Simic-Milosevic, Markus Heyde, Xiao Lin, Thomas König, Hans-Peter Rust, Martin Sterrer, Thomas Risse, Niklas Nilius, Hans-Joachim

Freund, Livia Giordano, and Gianfranco Pacchioni. Charge-induced formation of linear Au clusters on thin MgO films: Scanning tunneling microscopy and density-functional theory study. *Phys. Rev. B*, 78(23):235429, 2008.

[144] Steeve Chrétien, Mark S. Gordon, and Horia Metiu. Density functional study of the adsorption of propene on mixed gold-silver clusters, Au nAg m: Propensity rules for binding. *J. Chem. Phys.*, 121(20):9931–9937, 2004.

[145] Steeve Chrétien, Mark S. Gordon, and Horia Metiu. Binding of propene on small gold clusters and on Au(111): Simple rules for binding sites and relative binding energies. *J. Chem. Phys.*, 121(8):3756–3766, 2004.

[146] Horia Metiu, Steeve Chrétien, Zhenpeng Hu, Bo Li, and XiaoYing Sun. Chemistry of Lewis Acid–Base Pairs on Oxide Surfaces. *J. Phys. Chem. C*, 116:10439–10450, 2012.

[147] B. Hammer and J.K. Nørskov. *Impact of Surface Science on Catalysis*, volume 45 of *Advances in Catalysis*. Elsevier, 2000.

[148] J. K. Norskov, F. Abild-Pedersen, F. Studt, and T. Bligaard. Density functional theory in surface chemistry and catalysis. *Proc. Natl. Acad. Sci.*, 108(3):937–943, 2011.

[149] GreeleyJ., StephensI. E L., BondarenkoA. S., JohanssonT. P., HansenH. A., JaramilloT. F., RossmeislJ., ChorkendorffI., and NørskovJ. K. Alloys of platinum and early transition metals as oxygen reduction electrocatalysts. *Nat Chem*, 1(7):552–556, oct 2009.

[150] J. R. Kitchin, J. K. Nørskov, M. A. Barteau, and J. G. Chen. Modification of the surface electronic and chemical properties of Pt(111) by subsurface 3d transition metals. *J. Chem. Phys.*, 120(21):10240, 2004.

[151] Chun-Fang Huo, Yong-Wang Li, Jianguo Wang, and Haijun Jiao. Insight into CH_4 Formation in Iron-Catalyzed Fischer-Tropsch Synthesis. *J. Am. Chem. Soc.*, 131(41):14713–14721, 2009.

[152] B. Hammer and J. K. Nørskov. Electronic factors determining the reactivity of metal surfaces. *Surf. Sci.*, 343(3):211–220, 1995.

[153] Jeff Greeley, Jens K. Nørskov, and Manos Mavrikakis. ELECTRONIC STRUCTURE AND CATALYSIS ON METAL SURFACES. *Annu. Rev. Phys. Chem.*, 53(1):319–348, 2002.

[154] Glen R Jenness, Matthew a Christiansen, Stavros Caratzoulas, Dionisios G Vlachos, and Raymond J Gorte. Site-Dependent Lewis Acidity of γ-Al_2O_3 and Its Impact on Ethanol Dehydration and Etherification. *J. Phys. Chem. C*, 118:12899–12907, 2014.

[155] Philip A W Dean. The Oxalate Dianion, $C_2O_4^{2-}$: Planar or Nonplanar? *J. Chem. eEucation*, 89:417–418, 2012.

[156] Golnar Azimi, Henrik Leion, Tobias Mattisson, and Anders Lyngfelt. Chemical-looping with oxygen uncoupling using combined Mn-Fe oxides, testing in batch fluidized bed. *Energy Procedia*, 4:370–377, 2011.

[157] Golnar Azimi, Henrik Leion, Magnus Rydén, Tobias Mattisson, and Anders Lyngfelt. Investigation of different Mn-Fe oxides as oxygen carrier for chemical-looping with oxygen uncoupling (CLOU). *Energy and Fuels*, 27(1):367–377, 2013.

[158] Fang Liu. Cerium oxide (CeO2) promoted oxygen carrier development and scale modeling study for chemical looping combustion. *Theses Diss. Eng.*, 31, 2013.

[159] Lu Liu and Michael R Zachariah. Enhanced Performance of Alkali Metal Doped Fe_2O_3 and Fe_2O_3/Al_2O_3 Composites As Oxygen Carrier Material in Chemical Looping Combustion. *Energy & Fuels*, 27:4977–4983, 2013.